Title

Exploring the critical phenomenon in the QCD phase diagram at STAR

Author

Esha, Roli

Publication Date

2019

UNIVERSITY OF CALIFORNIA
Los Angeles

Exploring the critical phenomenon in the QCD phase diagram at STAR

A dissertation submitted in partial satisfaction
of the requirements for the degree
Doctor of Philosophy in Physics

by

Roli Esha

2019

ABSTRACT OF THE DISSERTATION

Exploring the critical phenomenon
in the QCD phase diagram
at STAR

by

Roli Esha
Doctor of Philosophy in Physics
University of California, Los Angeles, 2019
Professor Huan Z. Huang, Chair

The main goal of high-energy heavy-ion collisions has been to understand Quantum Chromo Dynamics (QCD) under extreme temperature and baryon densities. At ordinary temperatures, the quarks and gluons are confined within hadrons, but at very high temperatures and densities, we have a deconfined phase of quarks and gluons, the Quark Gluon Plasma (QGP). Over the past years, evidence for the distinct phases of QGP and hadron gas has been established experimentally.

Fluctuations and correlations have been considered as sensitive observables to explore the phases of the strongly interacting QCD matter, namely the QGP phase and the Hadron Gas phase, as they can provide essential information about the effective degrees of freedom. The main goal of this thesis is exploring the critical phenomenon in QCD phase diagram. In this thesis, we have studied two main aspects of the QCD phase diagram, namely, the crossover at small baryon chemical potential and signatures of local parton density fluctuation near the critical point within the framework of the STAR experiment at the Relativistic Heavy Ion Collider (RHIC).

Phase transitions and/or critical phenomena are known to lead to local density fluctuations. In the coalescence mechanism of particle production, the baryon formation probability can be influenced by these local parton density fluctuations, thereby leading to clusters and voids in the phase-space distribution of hadrons. In order to probe the density fluctuation in heavy-ion collisions, we studied the distribution of the ratio of particles in a given angular region to the total number of particles produced. We expect the shape of this distribution to be sensitive to clustering in phase space. For the first part, we measured the cumulants of this self-normalized distribution using the data from Au+Au collisions from the STAR Beam Energy Scan program to probe baryon density fluctuations.

Lattice QCD is a well-established non-perturbative approach to solve the theory of quarks and gluons exactly from first principles. However, these calculations are exact only at zero baryon chemical potential (μ_B). In order to explore the phenomenon at finite μ_B, these calculations are extended using Taylor expansion about $\mu_B = 0$. A constraint on the equation of state from Lattice QCD can be achieved by using the ratio of the sixth-order to the second-order baryon susceptibilities. In addition, Lattice QCD also predicts that the ratio of the sixth-order to second-order cumulants of baryon number remains negative at the chiral transition temperature. For the second part, we measured of the sixth-order cumulant for the net-proton (proxy for net-baryon) multiplicity distribution for Au+Au collisions at $\sqrt{s_{NN}} =$ 200 GeV (which corresponds to $\mu_B \sim 20$ MeV) for the high statistics run in the year 2014.

Unfortunately, the higher-order cumulants are very sensitive to experimental artifacts that one has to deal with in the analysis of heavy-ion collision data. The factorial moment method, which is used to account for the effect of detector efficiency, assumes the underlying detector response function to be a Binomial distribution. In order to account for non-Binomial detector responses and multiplicity-dependent efficiency, we developed an unfolding approach to measure efficiency-corrected higher-order cumulants of event-by-event distribution of physical variables.

The dissertation of Roli Esha is approved.

Gang Li

Per J. Kraus

Huan Z. Huang, Committee Chair

University of California, Los Angeles

2019

To my parents

for always being there

TABLE OF CONTENTS

LIST OF FIGURES

LIST OF TABLES

ACKNOWLEDGMENTS

The desire to explore and scrutinize brings us closer to many alluring facts. I would like to extend my heartfelt gratitude to all the hands and minds behind the successful completion of this dissertation.

I am grateful to my advisor, Prof. Huan Zhong Huang, for the opportunity, for being a constant source of inspiration, and for continued support and guidance. Thank you for being ever-generous with your knowledge. Thank you for helping me be a better person.

I would also like to thank the doctoral committee members, Prof. George Igo, Prof. Per Kraus, Prof. Gang Li and Prof. Nu Xu for their time and critical feedback.

Many thanks to the members of the Nuclear Physics Group at UCLA for all the discussions on physics and beyond. I am truly indebted for the wonderful experience. Special mention to Md. Nasim for patiently steering me through the analyses.

It was a great learning experience from the members of the STAR Collaboration who are committed to training the younger generation and keeping the excitement alive. Thank you!

To my friends, thank you for sticking around.

Special thanks to my beloved family - my parents (on both sides!), Ashwin, Ruhi, Ravineet and Amit for all your blessings, love and encouragement and to Himanshu for backing me through the thick and thin. Together, we did it!

VITA

2008 – 2013	Integrated Master of Science in Physics, National Institute of Science Education and Research, Bhubaneswar, India
2013 – 2014	Teaching Assistant, Department of Physics and Astronomy, University of California, Los Angeles
2014 –	Graduate Student Researcher, Nuclear physics group, Department of Physics and Astronomy, University of California, Los Angeles

CHAPTER 1

Introduction

With the advent of BEVELAC experiment at the Lawrence Berkeley National Laboratory in Berkeley, where nuclei were first accelerated to relativistic speeds successfully in 1984, to the collider experiments, Relativistic Heavy Ion Collider (RHIC) at the Brookhaven National Laboratory and the Large Hadron Collider (LHC) at CERN, the main goal of high-energy heavy-ion collisions has been to understand Quantum Chromo Dynamics (QCD) under extreme temperature and baryon densities. The most important characteristic of relativistic nucleus-nucleus collisions is the large amount of energy deposited in a very small region of space for a very short duration of time. In the collision of gold nuclei at RHIC, where the collider is designed to accelerate the nuclei to an energy of about 100 GeV per nucleon, the center-of-mass energy is about $2 \times 100 \times 197$ GeV, or 39.4 TeV. During central inelastic collision at such large center-of-mass energy, energy densities of few GeV/fm^3 may be achieved near the center-of-mass at mid-rapidity. The most relevant quantity is the amount of thermal energy density locally, which is the essence of the Björken formula. The collision energy for proton-proton collisions can be as large as 500 GeV at RHIC [1].

The nucleons inside the nucleus are made up of elementary particles, the quarks and gluons. At ordinary temperatures, the quarks and gluons are confined within hadrons, but at such high temperatures and densities, they form a deconfined state of matter where quarks and gluons are strongly coupled. This state, called the Quark Gluon Plasma (QGP), can be created in interactions of relativistic heavy-ions at the colliders such as RHIC [2]. Although the matter in the QGP state lasts for only one-billionth of a second after the collision, this is where scientists can master and expand our knowledge about QCD. For now, the properties of this extremely interesting but elusive state of the matter still remain a subject of intensive experimental and theoretical investigations.

1.1 The Standard Model of particle physics

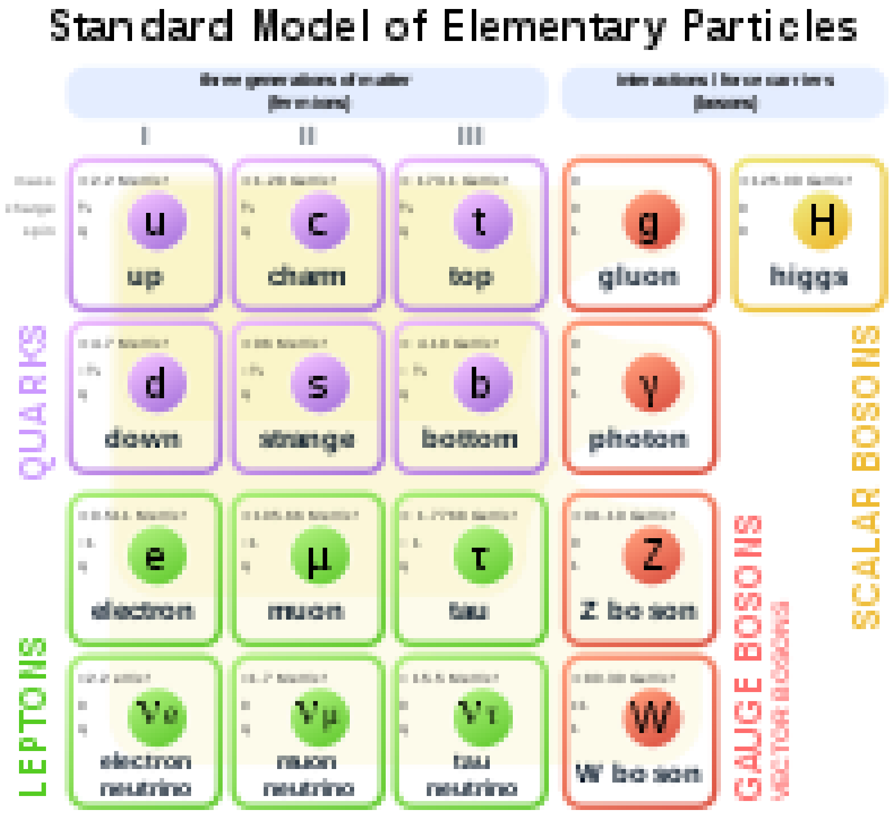

Figure 1.1: (Color online) The contents of the Standard Model of particle physics.

The Standard Model of particle physics describes our understanding of the phenomenology of particle physics. It is a theory describing three of the four known fundamental forces in nature, namely the strong, weak and electromagnetic forces. The first step towards the Standard Model was the unifications of the electromagnetic and weak interactions by Sheldon Glashow in 1961 [3]. In 1967, Steven Weinberg and Abdus Salam incorporated the Higgs mechanism into Glashow's electroweak interaction, giving it its modern form [4] [5]. The main ingredients of the Standard Model are shown in Figure 1.1. The particles involved are described by their spin, mass and charge and the quantum numbers determining their interactions. The fermions, comprising of the quarks and leptons, are organized in three families. The quarks are charged under strong and electromagnetic interactions. The heavier quarks decay into lighter ones, which makes most of the ordinary matter. The quarks which are positively charged under strong interactions, namely, up (u), charm (c) and top (t) quarks carry electromagnetic charge of $+2/3$, while the down (d), strange (s) and bottom (b) quarks are negatively charged under strong interactions and carry $-1/3$ electromagnetic charge. The leptons, electron (e), muons (μ) and tau (τ), carry -1 electromagnetic charge and are neutral under strong interactions. The neutrinos (ν_e, ν_μ and ν_τ) are neutral under both electromagnetic and strong interactions. The neutrinos interact through weak interactions. The masses of the fermions span a range going from the sub-eV neutrino masses to the 1.7×10^2 GeV top mass.

The interactions in the Standard Model are mediated through exchange of the four vector bosons. The photons (γ) are associated with electromagnetic interactions, the gluons with strong interactions, and the W and Z bosons with weak interactions. The photon and the gluons are massless, while the Z and the W are massive, which is the reason why weak interactions are weak at low energy. The distinctive signatures of weak interactions are violations of parity (P), charge conjugation (C), their combination (CP), time-reversal (T), and family number, which all are symmetries of the electromagnetic and strong interactions. In particular, the decay of heavier into lighter families is due to weak interactions.

The Standard Model predicted the existence of the scalar Higgs boson (H) in 1976 [6] [7] [8]. It is responsible for the masses of various fermions and the massive gauge bosons through the interactions with the Higgs field that permeated space-time. This particle was discovered recently at LHC in 2012 [9] [10].

1.2 Basics of Quantum Chromodynamics

Quantum Chromodynamics (QCD) is the theory that most accurately describes the physics of strong interactions. It is based on an $SU(3)$ gauge theory with quark in the fundamental and gluons in the adjoint representation of the gauge group. There is an internal degree of

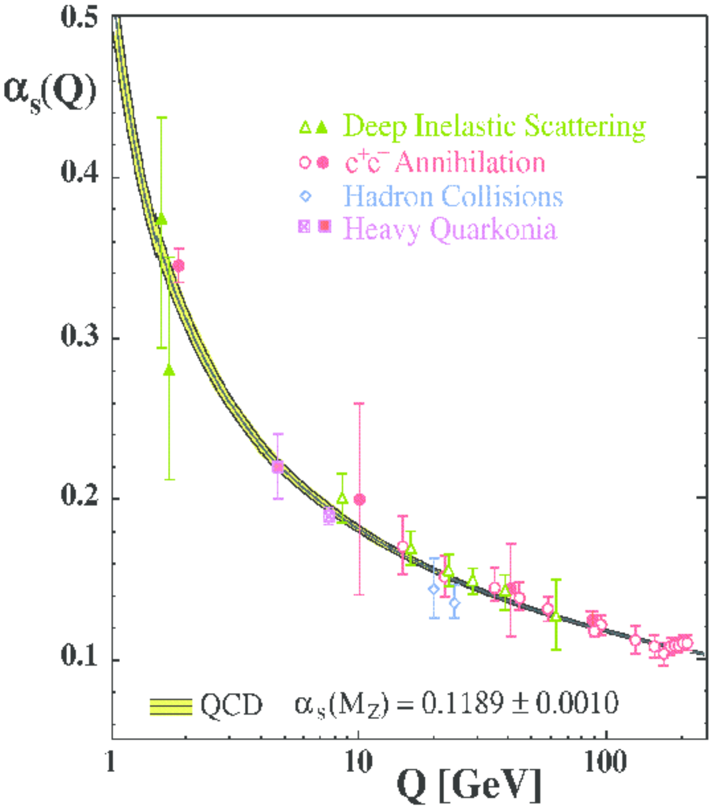

Figure 1.2: (Color online) Various measurements of the strong coupling constant, α_S, as a function of energy scale, Q. The curves are theoretical predictions.

freedom, the color degree of freedom, which provides for the arena of interaction amongst these particles. The quarks come in six flavors, namely, up, down, strange, charm, bottom and top in increasing order of their masses. These are fermions with spin 1/2. Three quarks come together in a color neutral state to form baryons, while a quark and an anti-quark together form colorless meson. Baryons and mesons are together called hadrons. All visible matter around us is made of hadrons. There are 8 massless, flavorless, colored gluons with spin 1. These are the force carriers of QCD.

QCD is characterized by its two key features, namely, confinement and asymptotic freedom. The coupling constant reflects the interaction strength among various constituents.

For QCD interactions, the coupling, α_S, is given by

$$\alpha_S = \frac{12\pi}{(11n - 2f)\ \ln(|Q^2|/\Lambda^2)}, \tag{1.1}$$

where n is the number of colors, f is the number of flavors, Q^2 is the amount of momentum transferred and Λ is the scale parameter with a value in the range of 100 MeV to 500 MeV. Figure 1.2 shows the values of α_S as extracted from different experiments and their comparisons with results from perturbative QCD (pQCD) [11].

Experimentally, a single quark described by color triplet state has never been isolated. The absence suggests that the interaction between quarks and gluons is very strong on large distance scales. This is what we mean by confinement. This idea was pioneered by Ken Wilson [12], within the backdrop of the "bag model", which is an effective picture of hadronic structure [13] [14]. On the other hand, the effective strength of the interaction between quarks and gluons on short distance scales becomes arbitrarily small. This is known as asymptotic freedom and was discovered by David Gross, Frank Wilczek and David Politzer in 1973 [15] [16] [17].

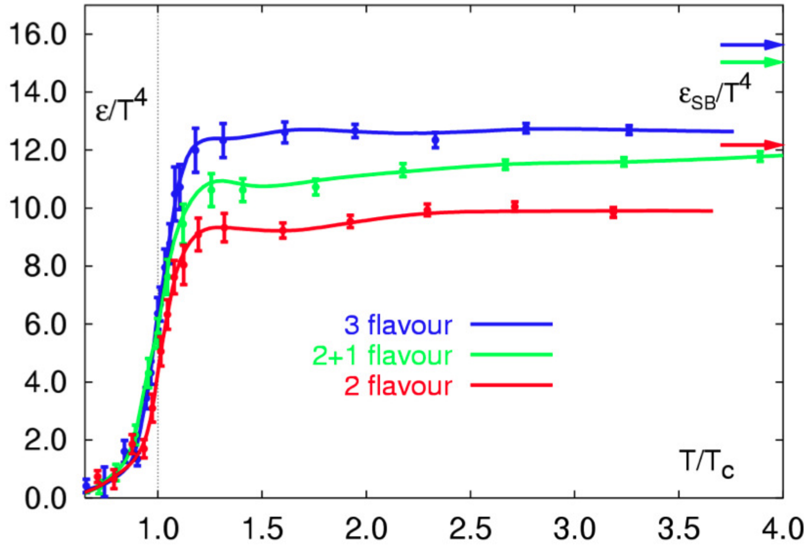

Figure 1.3: (Color online) Lattice QCD calculations for energy density as a function of temperature.

1.3 The Quark-Gluon Plasma

Based on the intriguing nature of strong interactions, in 1974, T. D. Lee proposed the creation of a dense state of nuclear matter at very high energies containing asymptotically free quarks and gluons [18]. This deconfined state of nuclear matter is called Quark Gluon Plasma (QGP) and is believed to have existed a few microseconds after the Big Bang [2]. Experimentally, QGP is defined as a (locally) thermally equilibrated state of matter in which quarks and gluons are deconfined from hadrons. The color degree of freedom becomes manifest over the nuclear volume.

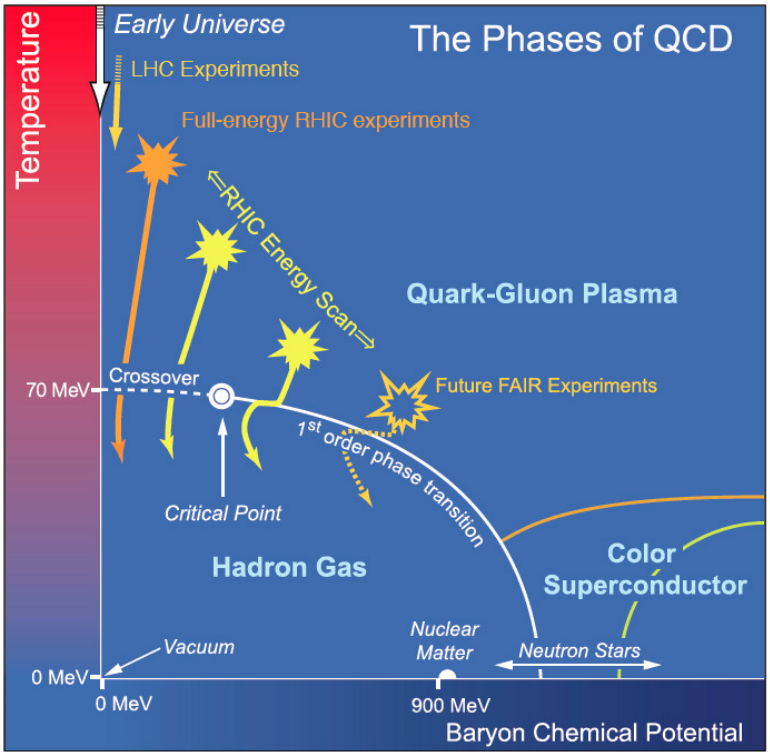

Figure 1.4: (Color online) Schematic QCD phase diagram for nuclear matter.

Lattice QCD aims to calculate QCD quantities non-perturbatively and from first principle using lattice gauge techniques on discretized space-time. These calculations predict a phase transition from confined hadronic matter to a deconfined phase of quarks and gluons around a critical temperature (T_c) of 154 MeV [19] and an energy density (ε) of 1 GeV/fm^3 [20]. Figure 1.3 shows the variation of energy density as a function of temperature for zero chemical potential. The active number of degrees of freedom, indicated by ε/T^4, increases rapidly, thereby, indicating the formation of a new state of matter. SB stands for the approximation in the Stefan-Boltzmann limit where the constituents are non-interacting and massless [20].

The study of QGP within the perspective of QCD phase diagram gives an insight into the thermal properties of strongly interacting matter. The QCD phase diagram, as shown in Figure 1.4, is spanned by baryon chemical potential (μ_B) and temperature (T) [21]. It has several distinct phase structures. Some of which are: (a) high temperature high density phase of deconfined quarks and gluons (QGP), (b) low temperature low density phase of hadrons, (c) nature of quark-hadron transition, and (d) end point of the first order phase transition line is a second order point, called the critical point (CP). Lattice QCD predicts the phase transition from QGP to hadron gas phase for small baryon chemical potential to be a cross-over transition [22] [23][1]. Theoretical calculations predict this transition to be a first-order phase transition for large baryon chemical potential that ends in a second-order critical point [24]. QCD calculations suggest that at low T and very large μ_B, quarks form a color superconducting phase [25].

1.4 Relativistic heavy-ion collisions

The name heavy-ion is used for heavy atomic nuclei whereas relativistic (high-energy) denotes kinetic energies much greater than the rest mass energy. Relativistic heavy-ion collisions are a key to explore the hydrodynamic properties like viscosity, conductivity, diffusion coefficient etc. of bulk quarks and gluons and to map the phase diagram of strong interactions.

The first heavy-ion collisions at the Bevalac accelerator in Lawrence Berkeley National Laboratory with a top collision energy of 2.1 GeV pioneered for experimental programs to continue at the Heavy Ion Synchrotron (SIS) at Helmholtzzentrum fur Schwerionenforschung (GSI), Alternating Gradient Synchrotron (AGS) at Brookhaven National Laboratory (BNL) and the Super Proton Synchrotron (SPS) at European Organization for Nuclear Research

---

[1] Lattice QCD calculations are exact only for $\mu_B = 0$

(CERN). These fixed-target experiments limited to few tens of GeV in the center-of-collision energy. The collider experiments at the Relativistic Heavy Ion Collider (RHIC) at BNL and the subsequent Large Hadron Collider at CERN pushed the collision energy to the TeV scale.

1.4.1 Space-time evolution

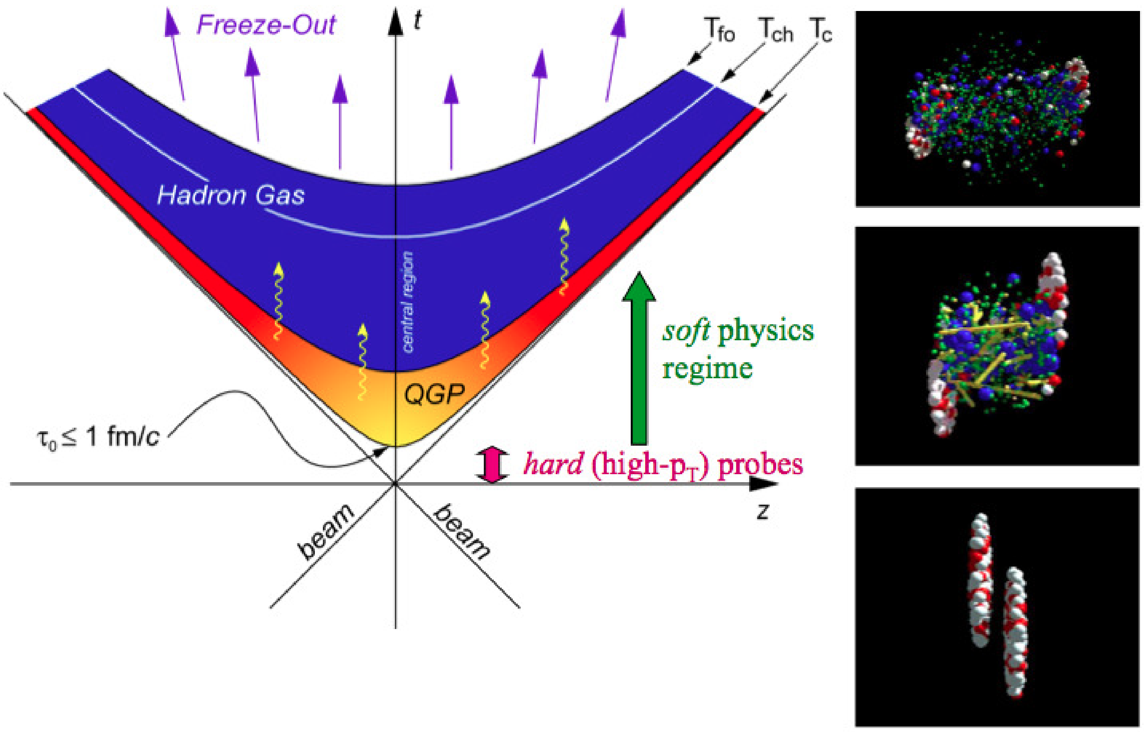

Figure 1.5: (Color online) Diagram showing space-time evolution of different stages in relativistic heavy-ion collisions.

In high-energy heavy-ion collisions, nuclei are accelerated to relativistic speeds. These appear as pancakes due to Lorentz contraction along the beam direction. Figure 1.5 shows a cartoon of the theoretically motivated space-time evolution of heavy-ion collisions at relativistic energies. At time $t = 0$, inelastic interactions develop in the overlapping region of the colliding nuclei. This loss in kinetic energy leads to creation of matter in the vicinity of the collision, often called the fireball. If the collision energy is large enough, QGP will be formed. Due to pressure gradient, the fireball expands, and hence cools. This QGP medium expands rapidly with falling energy density until the temperature decreases to the critical temperature, T_c, when the medium evolves into a mixed phase where partonic and hadronic matter may coexist. Chemical freeze-out temperature, T_{ch}, describes the point where inelastic processes that convert one kind of hadronic species into a different one cease and the hadron abundances stops changing. After further expansion, elastic collisions ceases. This is known as kinetic freeze-out temperature, T_{fo}, and the momenta of the particles stop changing.

1.4.2 Kinematics

Usually, the coordinate system in collider is defined such that the beam axis is parallel to the Z-axis. The point of collision of the two nuclei is called the primary vertex.

1.4.2.1 Transverse momentum

The total momentum of a particle can be divided into two components – longitudinal, which is its component along the beam direction, or transverse, which is the component perpendicular to the beam direction. In heavy-ion collisions, the beam direction is usually along the Z-axis. Hence, the transverse momentum, p_T is given by

$$p_T = \sqrt{p_x^2 + p_y^2} \tag{1.2}$$

where p_x and p_y are components of total momentum along the X and Y direction. Transverse momentum is a Lorentz invariant quantity.

1.4.2.2 Rapidity

Rapidity, y, is a dimensionless quantity defined in terms of the energy, E, and longitudinal momentum, p_z, of the particle.

$$y = \frac{1}{2} \ln \frac{E + p_z}{E - p_z} \tag{1.3}$$

It is related to the ratio of forward to backward light cone momentum. Rapidity is a frame dependent quantity and in two Lorentz frames, it is related by an additive constant.

1.4.2.3 Pseudorapidity

To characterize the rapidity of a particle, we need to measure its energy and longitudinal momentum, which means that the particle has to be identified. In many experiments, it is only possible to measure the angle of the detected particle with respect to the beam axis. In such situations, pseudorapidity, η, is used. It is a measure of the spatial coordinate described in terms of the angle of the particle relative to the beam axis.

$$\eta = -\ln\left[\tan\left(\frac{\theta}{2}\right)\right] \tag{1.4}$$

where θ is the angle between particle momentum and the beam-axis. For massless particles or for particles with very high momentum, rapidity and pseudorapidity coincide.

1.4.2.4 Multiplicity

Multiplicity is defined as the total number of particles produced in a collision. Since most of the detectors measure charged particles, multiplicity is often synonymous with charged particle multiplicity.

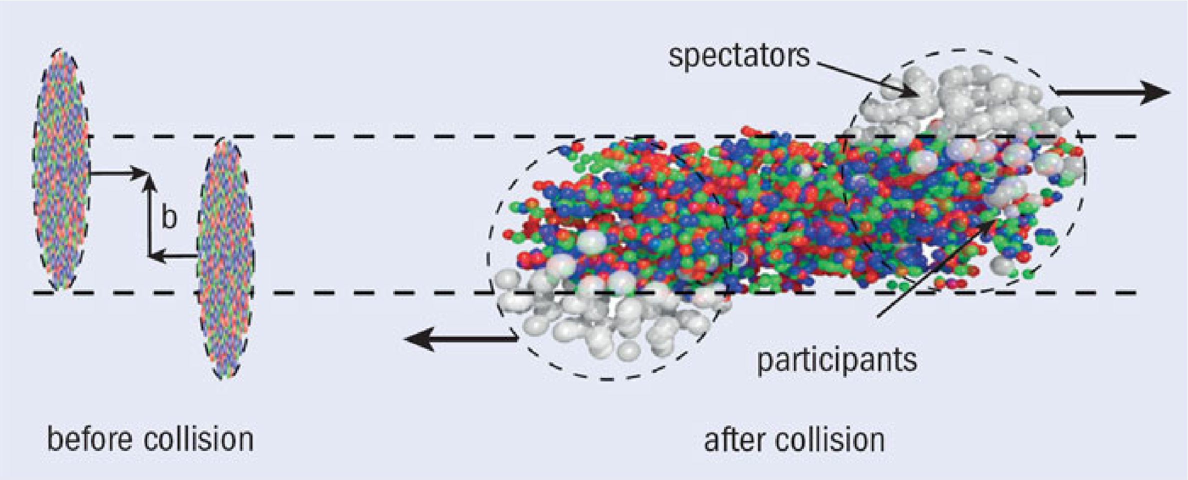

Figure 1.6: (Color online) A geometric view of relativistic heavy-ion collisions.

1.4.2.5 Collision centrality

Theoretically, centrality is characterized by the impact parameter which is the distance between the centers of two colliding heavy ions in a plane transverse to the beam direction as shown in Figure 1.6. Small impact parameter collisions are central collisions while large impact parameter collisions are peripheral collisions. Experimentally, the collision centrality is inferred from the measured particle multiplicities if it is assumed that this multiplicity is a monotonic function of impact parameter. When the total integral of the multiplicity distribution is known, centrality classes are defined by binning the distribution based upon the fraction of the total integral. The details of centrality determination technique using charged particle multiplicity will be discussed in Chapter 4.

1.4.2.6 Units and conversion factors

Table 1.1: Conversion from SI to natural units

Quantity	Conversion
Mass	1 kg = 5.61×10^{26} GeV
Length	1 m = 5.07×10^{15} GeV^{-1}
Time	1 s = 1.52×10^{24} GeV^{-1}

In heavy-ion collisions, all quantities are expressed in natural units *i.e.* velocity of light, $c = 1$ and Plank's constant $\hbar = 1$. Regular physical units can be converted into natural units using the conversion formula, $\hbar c = 197$ MeV-fm. Table 1.1 gives the values of mass, length and time in natural units.

1.5 Experimental Observables

The elusive hot and dense medium created in relativistic heavy-ion collisions lasts for a very short time ($\sim$ 5–10 fm). In heavy-ion experiments, particles from final state of the evolution are detected. Various measurements on these particles provide an insight into the different stages of evolution and the properties of QGP.

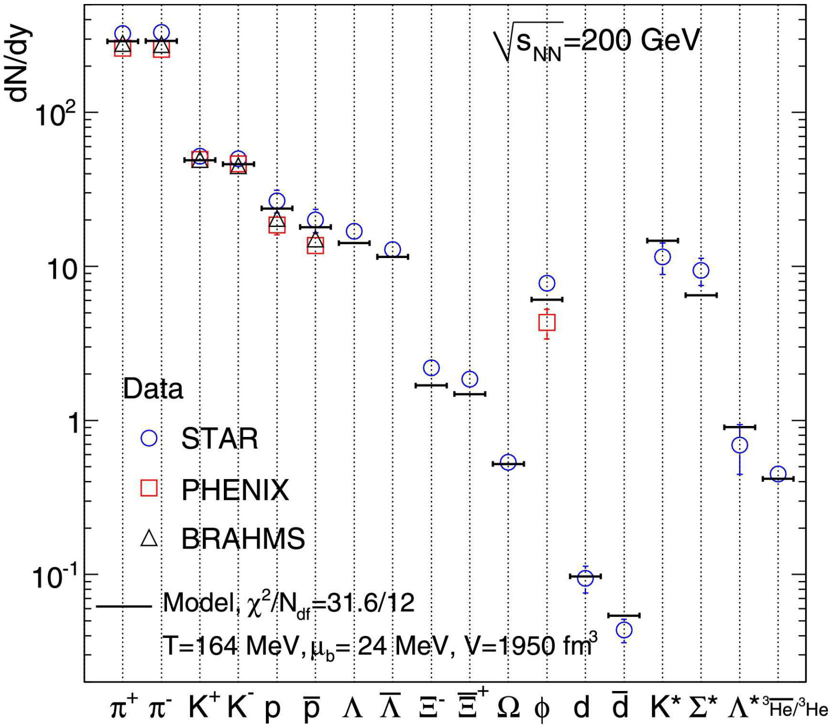

Figure 1.7: Comparison of particle yields with a thermal statistical model fit for Au+Au collisions at $\sqrt{s_{NN}} = 200$ GeV.

One of the important features of high-energy heavy-ion collisions is that the particles in the final state corresponding to different momentum regime may come from different production mechanisms. Most of the particles with transverse momentum below 2 GeV/c at RHIC (often referred to as the soft sector) are dominated by thermal production from the QGP medium. The particles with large transverse momentum ($p_T > 6$ GeV/c at RHIC) are mainly produced by perturbative processes and constitute the hard sector. The intermediate transverse momentum regime is dominated by the coalescence mechanism.

In the following subsections, some of the signatures of QGP formation and the associated characteristics of the medium is discussed.

1.5.1 Hadron yields

The measurement of particle yield provides information about the system at chemical freezeout as it marks the end of inelastic collisions, thereby, fixing chemical abundances. The particles produced in the soft sector exhibit features of thermal statistics. Figure 1.7 shows a thermal statistical model fit to the measured yields of various particles in Au+Au collisions at $\sqrt{s_{NN}} = 200$ GeV [26]. The horizontal lines are the statistical model fit to particle yields. In the regime of the model, three parameters are used, namely, chemical freezeout temperature, $T_{ch} = 164 \pm 4$ MeV, baryon chemical potential, $\mu_B = 24 \pm 4$ MeV and strangeness suppression factor, $\gamma_s = 0.99 \pm 0.07$ [27]. The strangeness suppression factor is a measure of how far the system is from chemical equilibrium. As the value of γ_s is consistent with unity, it implies that the system formed at RHIC is in chemical equilibrium.

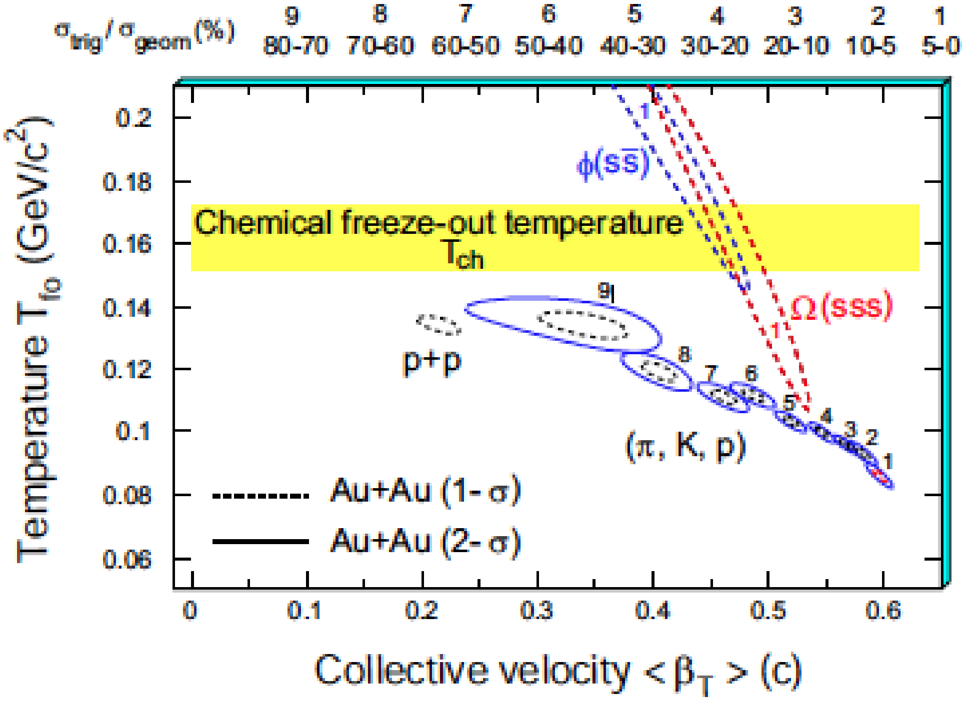

Figure 1.8: (Color online) The 1σ and 2σ contour for $\langle\beta_T\rangle$ and T_{fo} extracted from thermal and radial flow fits to π, K and p spectra in 9 centrality bins for Au+Au and $p+p$ collisions at $\sqrt{s_{NN}} = 200$ GeV.

With elastic interactions ceasing and the momentum distributions fixed, at kinetic freezeout, the measurement of particle spectra is an important observable. The particle spectra are compared with blast-wave model, the fit parameters being kinetic freezeout temperature (T_{fo}) and the mean collective expansion velocity, ($\langle\beta_T\rangle$). The results obtained by simultaneous fitting of π, K and p spectra are shown in Figure 1.8 [27]. For most central collision, the extracted $\langle\beta_T\rangle$ is highest while (T_{fo}) is lowest, indicating that the system created in central collisions expands faster than peripheral collisions and freezes out at lower temperatures.

1.5.2 Collective Flow

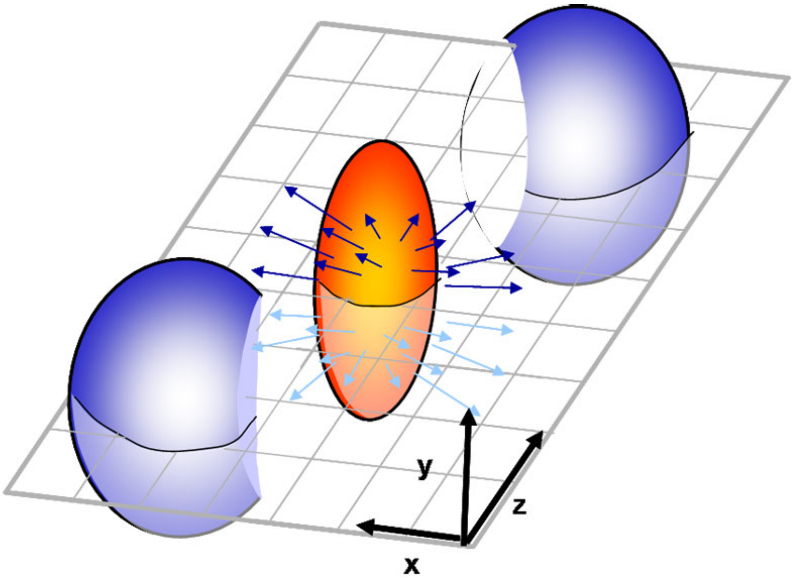

Figure 1.9: (Color online) Cartoon for non-central nucleus-nucleus collision.

The system of heavy-ion collision is surrounded by vacuum. This gives rise to a pressure gradient from the dense center to the boundary of the system. This pressure gradient is radially symmetric for head-on heavy-ion collisions and gives a radially outward boost to all particles that are formed in the system. This influences the transverse momentum spectra of heavy particles. For non-central collisions, the shape of the interaction region depends strongly on the impact parameter of the collision. Just after the collision, as shown in Figure 1.9, the reaction volume is elliptically shaped. This initial spatial anisotropy of collision geometry and the interaction among particles produced lead to momentum anisotropy of pro-

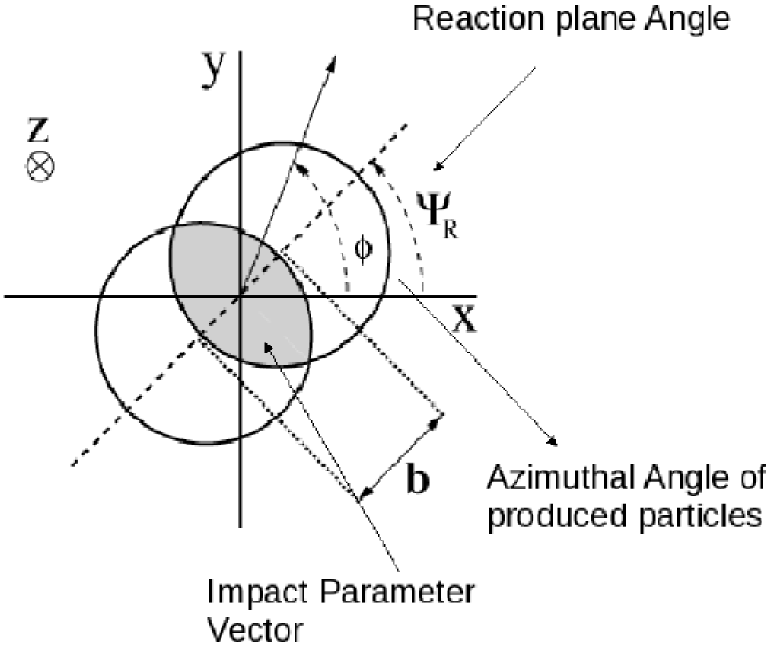

Figure 1.10: Non-central nucleus-nucleus collision with azimuthal angle, ϕ and reaction plane angle, ψ_{rp}.

duced particles in high-energy heavy-ion collisions. The anisotropic flow leads to azimuthal distribution of particles which is measured with respect to reaction plane. The particle azimuthal distribution relative to reaction plane can be written in the form of Fourier series

$$\frac{dN}{d\phi} = \frac{1}{2\pi}\left(1 + \sum_{n=1}^{\infty} 2v_n \cos\left[n(\phi - \psi_{rp})\right]\right) \tag{1.5}$$

where ψ_{rp} is the reaction plane angle defined by the impact parameter vector in the transverse plane as shown in Figure 1.10.

The coefficients v_n are given by

$$v_n = \langle \cos\left[n(\phi_i - \psi_{rp})\right] \rangle \tag{1.6}$$

Here $\langle . \rangle$ denotes the average over all the particles produced for all events. The first two coefficients v_1 and v_2 are called directed and elliptic flow respectively [28]. Measurements of v_1 and v_2 of identified particles at the STAR experiment is shown in Figure 1.11 [29] [30] and

Figure 1.12 [31] respectively. The mass ordering observed in Figure 1.12 is a characteristic of hydrodynamic evolution of the QGP medium [32].

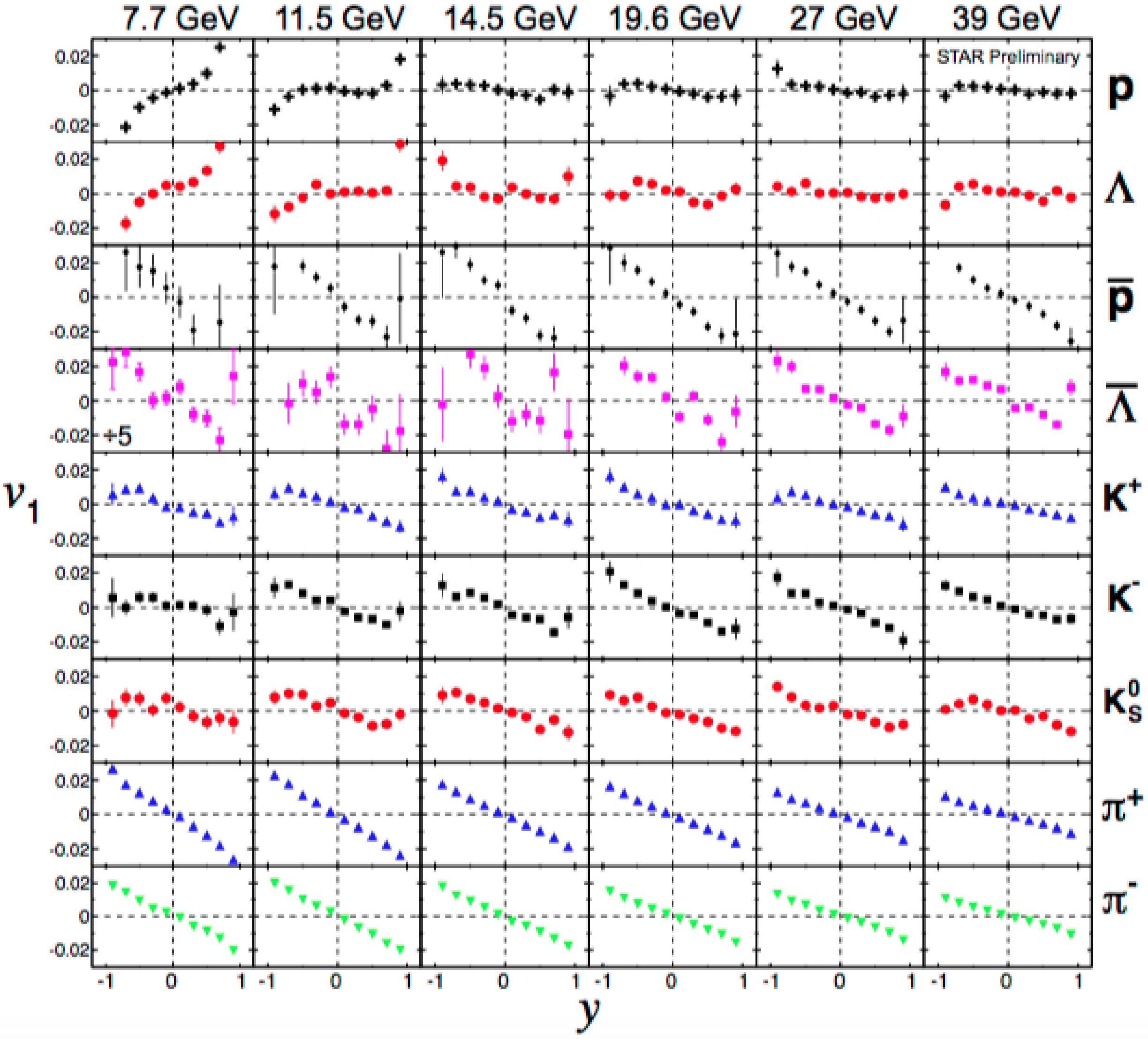

Figure 1.11: (Color online) The directed flow, v_1 as a function of rapidity in 0-40% central Au+Au collisions for identified particle.

1.5.3 Strangeness enhancement

Strangeness is the lightest unstable quark flavor that appears in *pp* collisions with an abundance that is about a factor 2.5-3 below that of each light quark flavor, called the Wroblewski

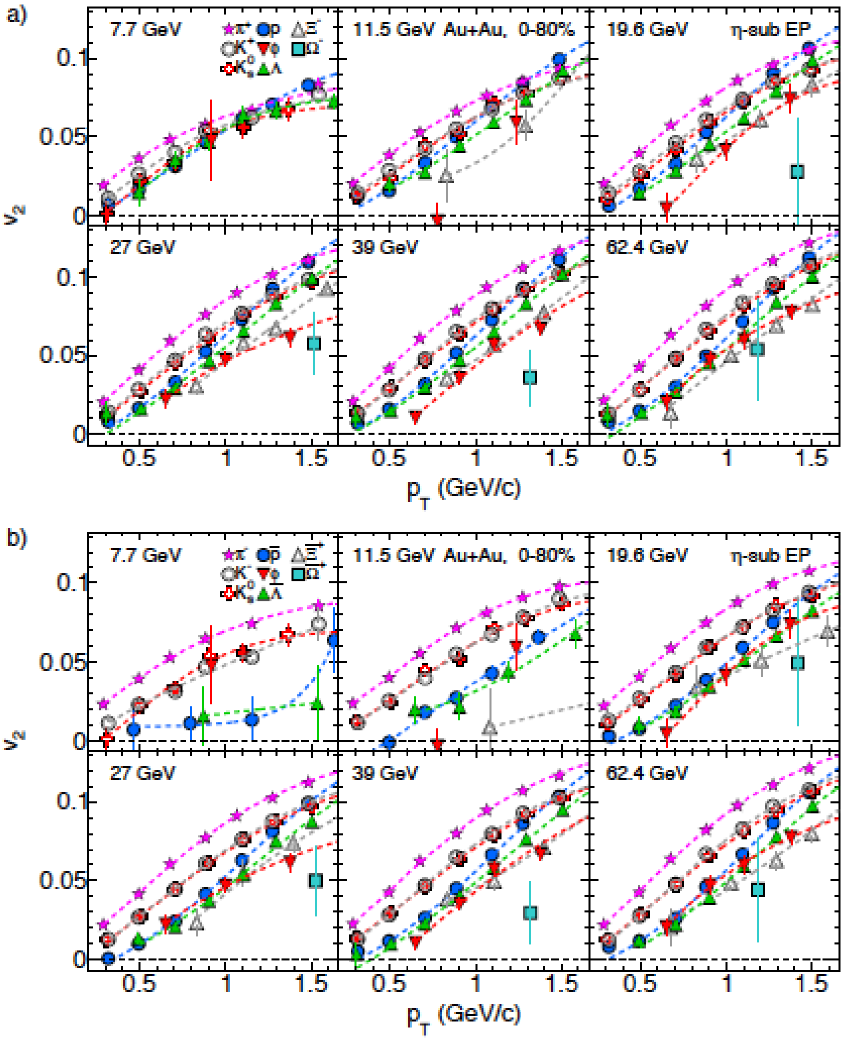

Figure 1.12: (Color online) The elliptic flow, $v_2(p_T)$ in 0-80% central Au+Au collisions for identified particles (a) and anti-particles (b).

ratio [33]. However, in nucleus-nucleus collisions, it is found that the ratio of the number of produced kaons to that of pions is higher by a factor of about two compared to that in proton-proton reactions at the same energy [34] [35]. This strangeness enhancement is possible if the nucleus-nucleus reactions proceeds through a de-confined stage [36].

Figure 1.13 shows the ratio of strange hadron yields normalized to $\langle Npart \rangle$ in nucleus-nucleus collisions relative to corresponding yields from proton-proton collisions at 62.4 and 200 GeV [37]. Enhancement of $\phi(s\bar{s})$ production in Cu+Cu and Au+Au relative to p+p collisions clearly indicates the formation of a dense partonic medium in these collisions.

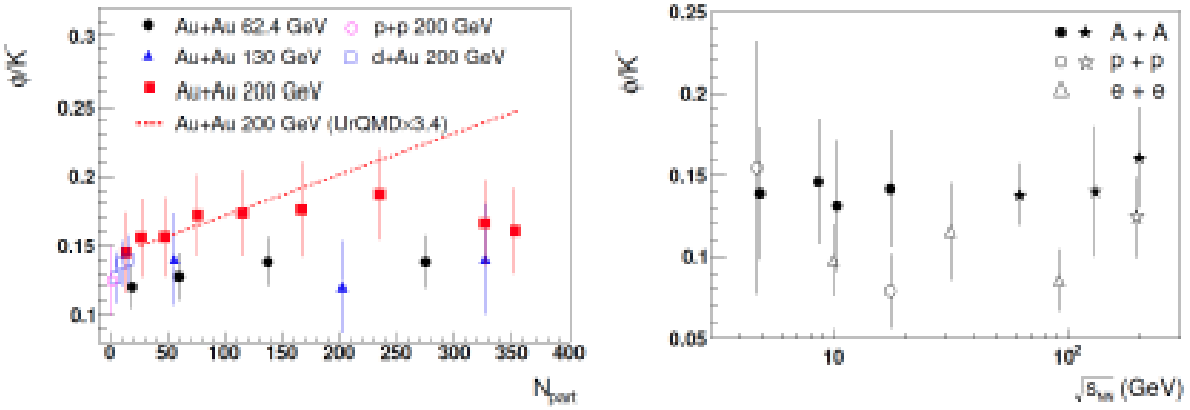

Figure 1.13: (Color online) Left panel: ϕ/K^- ratio as a function number of participants. Right panel: ϕ/K^- ratio as a function of centre-of-mass energies.

1.5.4 Hard hadrons: jet quenching

With increasing center of collision energies, hard parton back-scattering occurs in nucleus-nucleus collisions (as in *pp* collisions) at a rate described by perturbative QCD [38] [39]. Such hard partons are observed as back-to-back jets. These jets are created in the primordial medium at the initial time when the two colliding nuclei are passing each other. Geometrically, if such a pair is produced near the edge of the colliding matter, then one of the jet-partons can escape, while the balancing momentum of the immersed jet parton traverses QGP that has evolved in the collision. The energy of such a parton can be partially or completely dissipated. This phenomenon is called jet-quenching.

Dihadron azimuthal correlations can be used to observe jets in high energy collisions as shown in Figure 1.14 [27]. The parton-pair created moves in opposite direction, thereby giving rise to strong correlations between $\phi = 0$ and $\phi = \pi$, as seen in $p + p$ and $d+$ Au collisions. However, in Au+Au collisions one of the partons is scattered in the QCD medium so it loses significant energy as well as the original direction, resulting in the quenching of the peak on the away side.

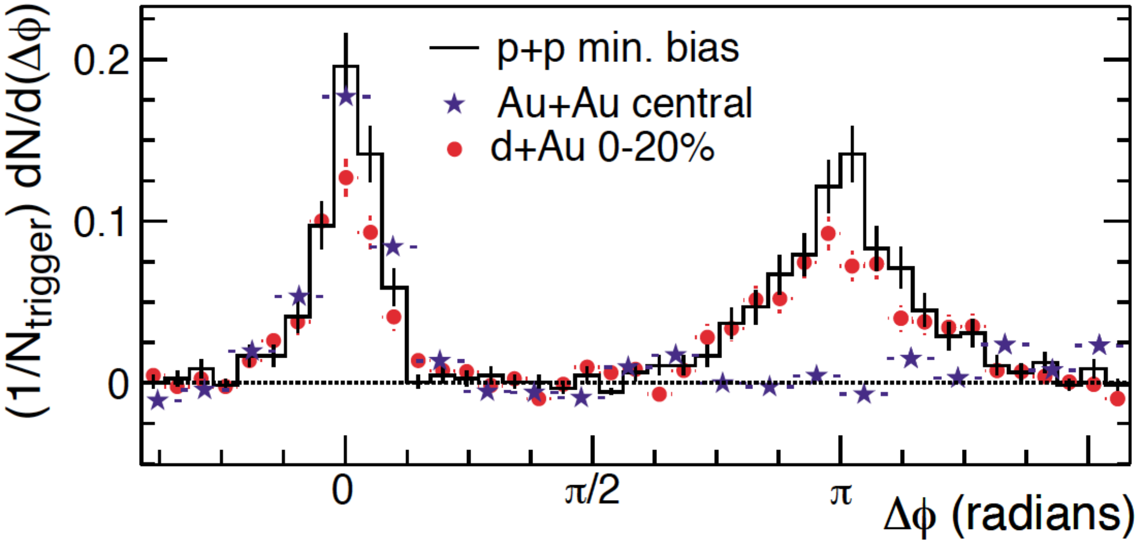

Figure 1.14: (Color online) Dihadron azimuthal correlation for different collision systems.

1.5.5 Fluctuations

Any physical system that appears homogenous actually consists of large microscopic fluctuations. To see fluctuations in QGP medium, event-by-event measurements are performed. The search is for large, non-statistical fluctuations that would signal competition between two different phases of matter, a phase transition [40].

1.6 Thesis outline

One of the main goals of the RHIC Beam Energy Scan program is to search for the QCD Critical Point (CP) and phase transition in heavy-ion collisions. Over the past years, evidence for the distinct phases of Quark Gluon Plasma (QGP) and hadron gas has been established experimentally. Lattice QCD predicts the transition from the QGP phase to the hadron gas phase to be a crossover at zero baryon density [23], while QCD-inspired models predict it to be a first-order phase transition for large baryon chemical potential and to end in a second-order critical point [24]. Both theory and experiment have ruled out the existence of a critical point below baryon chemical potential (μ_B) values of 154 MeV [41].

In this thesis, we have studied two main aspects of the QCD phase diagram, namely, the crossover at small baryon chemical potential and signatures of local parton density fluctuation near the critical point with data from the STAR experiment at the Relativistic Heavy Ion Collider (RHIC).

Phase transitions and/or critical phenomena are known to lead to local density fluctuations. In the coalescence mechanism of particle production, the baryon formation probability can be influenced by these local parton density fluctuations, thereby leading to clusters and voids in the phase-space distribution of hadrons. In order to probe the density fluctuation in heavy-ion collisions, we studied the distribution of the ratio of particles in a given angular region to the total number of particles produced. We expect the shape of this distribution to be sensitive to clustering in phase space. For the first part, we measured the cumulants of this self-normalized distribution using the data from Au+Au collisions from the STAR Beam Energy Scan program to probe baryon density fluctuations.

Fluctuations and correlations have been considered as sensitive observables to explore the phases of the strongly interacting QCD matter as they can provide essential information about the effective degrees of freedom. The magnitude of the fluctuation of conserved quantities (baryon number, strangeness, and charge of the system) in a grand canonical ensemble at finite temperature are distinctly different in the hadronic and the QGP phases and can be related to the susceptibility of the system [42] [43] [44]. The susceptibility (χ), which is defined as the derivative of free energy density or pressure (p) of a thermodynamic system at a given temperature (T) with respect to the chemical potential (μ). This can be related to the cumulants (C) of the event-by-event distribution of the associated conserved quantity by:

$$\chi_q^{(n)} = \frac{\partial^n (p/T^4)}{\partial(\mu_q/T)^n} = \frac{1}{VT^3} \times C_{n,q}, \tag{1.7}$$

where V is the volume of the system, n is the order, and q is baryon number, strangeness or charge of the system. The ratios of such cumulants as experimental observables cancel the volume and temperature dependence and can be directly compared to the ratios of susceptibilities from theoretical calculations.

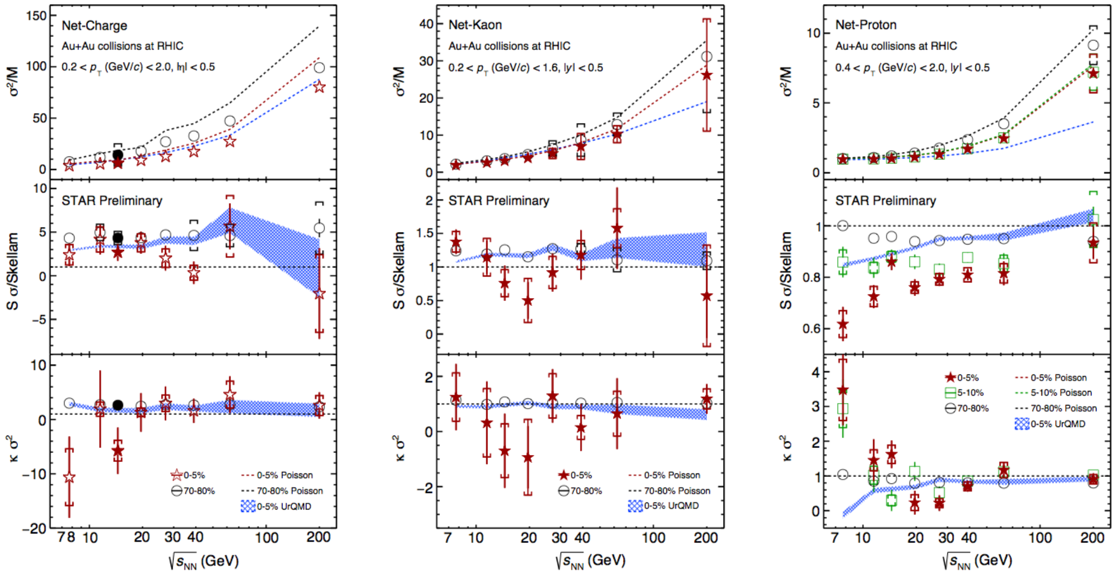

Figure 1.15: Variation of the cumulant ratios for net-charge, net-kaon and net-proton multiplicity distribution with beam energy from the STAR experiment for different centralities.

Constrained by statistics, upto fourth-order cumulants for net-proton multiplicity distribution have been measured at the STAR experiment. Figure 4.16 shows the measurements of the cumulant-ratios for net-charge (left panel), net-kaon (middle panel) and net-proton (right panel) multiplicity distributions from Au+Au collisions at $\sqrt{s_{NN}}$ = 7.7, 11.5, 14.5, 19.6, 27, 39, 62.4 and 200 GeV from the STAR experiment [45] [46] [47] [48]. The black circles are the measurements for 70-80%, green squares for 5-10% and red stars for 0-5% central collisions. The corresponding dashed lines are the Poisson baselines. The blue band is the result from 0-5% central collisions from the UrQMD model calculations. It should be noted that the kinematic range for the measurements are different. Results for net-charge include all charged particles within transverse momentum region of 0.2 to 2.0 GeV/c and pseudorapidity ranging from -0.5 to 0.5. The spallation protons with transverse momentum less than 0.4 GeV/c are excluded. For the cumulants of net-kaons, (anti-)kaons within transverse momentum region of 0.2 to 1.2 GeV/c and rapidity ranging from -0.5 to 0.5 are included. For the net-proton analysis, (anti-)protons within transverse momentum region of 0.4 to 2.0 GeV/c and rapidity ranging from -0.5 to 0.5 are included. Within large statistical error bars, we find a monotonic trend in the various cumulant ratios for net-charge and net-kaon multiplicity distributions with the collision energy. However, higher cumulants of net-proton multiplicity distributions show a non-monotonic trend for central collisions.

For the second part, we measured of the sixth-order cumulant for the net-proton (proxy for net-baryon) multiplicity distribution for Au+Au collisions at $\sqrt{s_{NN}} = 200$ GeV for the high statistics run in the year 2014.

In order to precisely measure the event-by-event fluctuation of conserved quantities, a series of analysis techniques are applied. As no detector is perfect, an important step is particle detection efficiency correction. There could be noticeable consequences of the multiplicity-dependent behavior of particle detection efficiency on the measured higher-order cumulants [49]. In order to understand and overcome these issues, we have developed a data-driven approach for efficiency correction. We use this method to investigate the multiplicity-dependent detector response and efficiency variations. The effect for different efficiency correction techniques on the measurement of the cumulants for net-proton multiplicity distribution for Au+Au collisions at $\sqrt{s_{NN}} = 200$ GeV is discussed in the third part.

The plan of this thesis is as follows. In Chapter 2, the technical details of the STAR experiment is discussed. Chapter 3 deals with the search for critical phenomenon using local parton density fluctuations. In Chapter 4, the measurements for the sixth-order cumulant for net-proton multiplicity distribution for Au+Au collisions at $\sqrt{s_{NN}} = 200$ GeV is presented. The unfolding method for efficiency correction is developed in Chapter 5. The summary and future prospects are discussed in Chapter 6.

CHAPTER 2

Experimental set-up

The Relativistic Heavy Ion Collider (RHIC) at the Brookhaven National Laboratory in Upton, NY is world's first accelerator facility that is capable of colliding heavy and light ions, e.g. gold, copper and deutrons, and polarized protons at relativistic energies [50]. STAR, which stands for Solenoid Tracker at RHIC, is one of the four experiments housed in the RHIC complex. It is a massive detector system with full azimuthal coverage and excellent particle identification capabilities constructed to investigate the behavior of strongly interacting matter formed in high-energy heavy-ion collisions and to search for the signatures of Quark-Gluon Plasma.

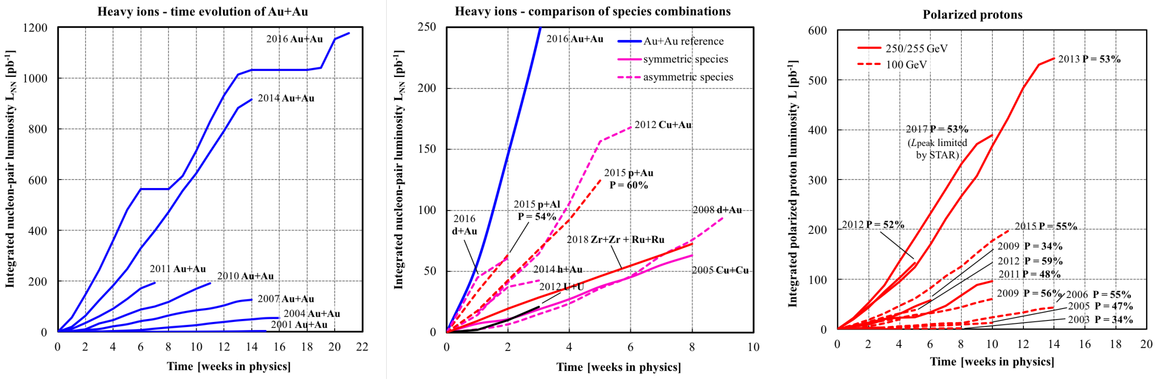

Figure 2.1: (Color online) Summary of RHIC runs. The nucleon-pair luminosity is defined as $L_{NN} = A_1 A_2 L$, where L is the luminosity, and A_1 and A_2 are the number of nucleons of the ions in the two beams respectively. The proton polarization is intensity and time averaged over the whole run, as measured by the H-jet.

2.1 Relativistic Heavy Ion Collider

The Relativistic Heavy Ion Collider began its operation in the year 2000 and is one of the two collider facilities (other being the Large Hadron Collider at CERN which started in 2010) currently in operation. So far, it is the only spin-polarized proton collider. The RHIC complex is a series of particle accelerators that enable acceleration and collision of various particle species, ranging from polarized protons to heavy nuclei like gold, through a wide range of center-of-mass energies [51] [52] [53]. Figure 4.4 gives a brief overview of the luminosities and the running periods for the heavy-ion and the polarized $p + p$ collisions at RHIC [54]. Table 2.1 summarizes the particle species that are collided at RHIC with their respective energies [54].

Table 2.1: Summary of RHIC operations

Particle species	Total particle energy (GeV/nucleon)
Polarized $p + p$	31.2 – 254.9
Polarized p + ^{27}Au^{13+}	103.9 + 98.7
Polarized p + ^{197}Au^{79+}	103.9 + 98.6
d + ^{197}Au^{79+}	9.9 + 9.8 – 100.7 + 100.0
^{3}He^{2+} + ^{197}Au^{79+}	103.5 + 100.0
^{63}Cu^{29+} + ^{63}Cu^{29+}	11.2 – 100.0
^{63}Cu^{29+} + ^{197}Au^{79+}	99.9 + 100.0
^{96}Zr^{40+} + ^{96}Zr^{40+}	100.0
^{96}Ru^{44+} + ^{96}Ru^{44+}	100.0
^{197}Au^{79+} + ^{197}Au^{79+}	3.85 – 100.0
^{197}Au^{79+} + ^{197}Au (fixed target)	3.85 – 31.2
^{238}U^{92+} + ^{238}U^{92+}	96.4

2.1.1 Stages of particle acceleration

A schematic drawing of the RHIC accelerator complex is shown in Figure 2.2 [1]. The important subsystems, namely the Electron Beam Ion Source (EBIS) accelerator (1), the Linac (2), the Boosters (3), the Alternating Gradient Synchrotron (4), the beamline (5) and the RHIC rings (6) are numbered.

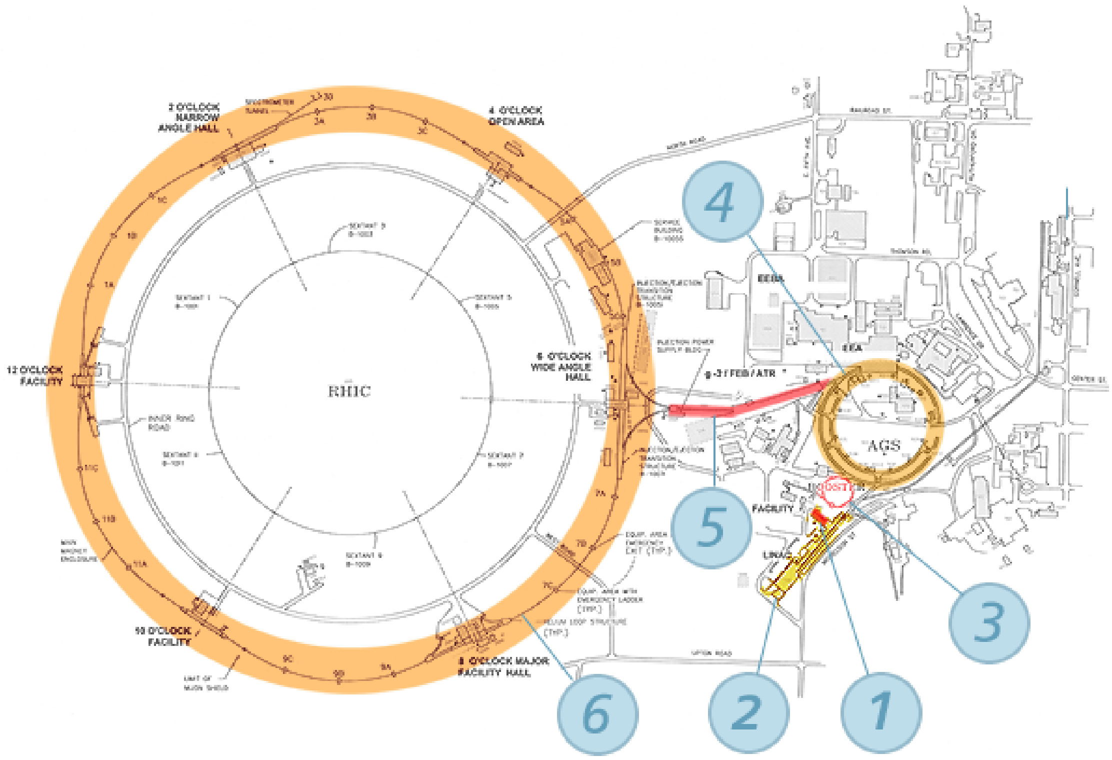

Figure 2.2: (Color online) A schematic drawing of the RHIC accelerator complex, with the important subsystems namely the Electron Beam Ion Source (EBIS) accelerator (1), the Linac (2), the Boosters (3), the Alternating Gradient Synchrotron (AGS) (4), the beamline (5) and the RHIC rings (6) numbered.

The particles are passed through several stages [1] [55], which are discussed below, before reaching the desired energy.

1. **Electron Beam Ion Source (EBIS)**: EBIS is a pre-injector system for heavy-ion acceleration where highly charged ion beams can be created from any element. These ion beams are then accelerated by two small linear accelerators before being carried to

the Booster Synchrotron. For example, gold ions leaving EBIS have a charge of +32 and kinetic energy of 2 MeV per nucleon.

2. **Linac**: The starting point for proton beam is the 200 MeV Linac from where it is transferred to the Booster Synchrotron.

3. **Booster Synchrotron**: A synchrotron is a circular accelerator with the accelerating voltage adjusted to synchronize with the circulation period of the particles being accelerated. The Booster Synchrotron is used to pre-accelerate particles entering the AGS ring. The superior vacuum at the Booster makes it possible to accelerate heavy ions upto uranium. When exiting, gold ions are accelerated to 100 MeV per nucleon with a charge of +77. The beam is then injected into the AGS ring.

4. **Alternating Gradient Synchrotron (AGS) ring**: The field gradient of the 240 magnets in the AGS ring are alternated inward and outward successively, thereby focussing the particle beam both in the horizontal and vertical planes simultaneously. When exiting the AGS ring into the AGS-to-RHIC beamline, gold ions are accelerated to 8.86 GeV per nucleon and a charge of +77.

5. **AGS-to-RHIC line**: A foil at the beginning of the AGS-to-RHIC transfer line strips the last two electrons of the gold ions. The switching magnets at the end of the line are used to direct the bunches to either to the left in the the clockwise, or to the right in the counter-clockwise RHIC ring.

6. **RHIC ring**: RHIC is a particle accelerator that doubles up as a storage ring. It consists of two independent 2.4 mile long, quasi-circular rings where heavy-ions and/or polarized protons are (de)accelerated to the final collision energy and circulated in opposite directions for upto 10 hours, colliding at the intersection points. The six intersection points, where the rings cross allowing the particles to collide, are identified by clock positions, with the injection near 6 o'clock. Large super-conducting magnets are used for focusing the particle beams [56]. The dipole magnets operate at 3.45 T. Polarized protons, which are injected into the RHIC ring, are preserved in their state

with the help of Siberian snakes (chain of 4 helical dipole magnets) in the ring.

The collisions at RHIC were captured and studied by the four experimental detectors around the ring. Out of these, only one continues to operate. The STAR experiment is located at the 6 o'clock position and the PHENIX experiment (retired in 2016) at 8 o'clock. The PHOBOS and BRAHMS experiments, which are already decommissioned in 2005 and 2006 respectively, were located at the 10 o'clock and 2 o'clock positions.

The STAR detector specializes in the tracking and identification of charged hadrons covering a large solid angle at mid-rapidity in a conventionally generated solenoidal magnetic field [57]. The PHENIX experiment was aimed at measuring the direct probes of the collision using a partial coverage detector system in a super-conductively generated axial magnetic field [58]. The PHOBOS detector had the largest pseudo-rapidity coverage and was tailored to measure bulk particle multiplicities [59]. The BRAHMS experiment was designed to study the small-x physics using momentum spectroscopy [60].

The flexibility of colliding species and energies at RHIC makes it ideal to explore the properties of nuclear matter under extreme conditions.

2.2 Solenoid Tracker At RHIC (STAR)

STAR is one of the two large detector systems at RHIC. This massive detector system weighs 1200 tons. STAR was constructed to search for the signatures of QGP and study the properties of QGP formed in high-energy nucleus-nucleus collisions. The main feature of such collisions is that a large number of particles, of the order of 1000 at mid-rapidity, are produced. In addition, high momentum particles are also produced from hard-parton scatterings. STAR is designed to measure hadron production across large solid angle. The detectors sub-systems allow for high precision tracking, momentum analysis, and particle identification at the center of mass rapidity. It is the only experiment at RHIC which can measure the full azimuth and tracks particles from 100 MeV/c to 20 GeV/c [57]. This makes STAR particularly well suited for event-by-event characterizations of heavy-ion collisions and for the detection of hadron jets.

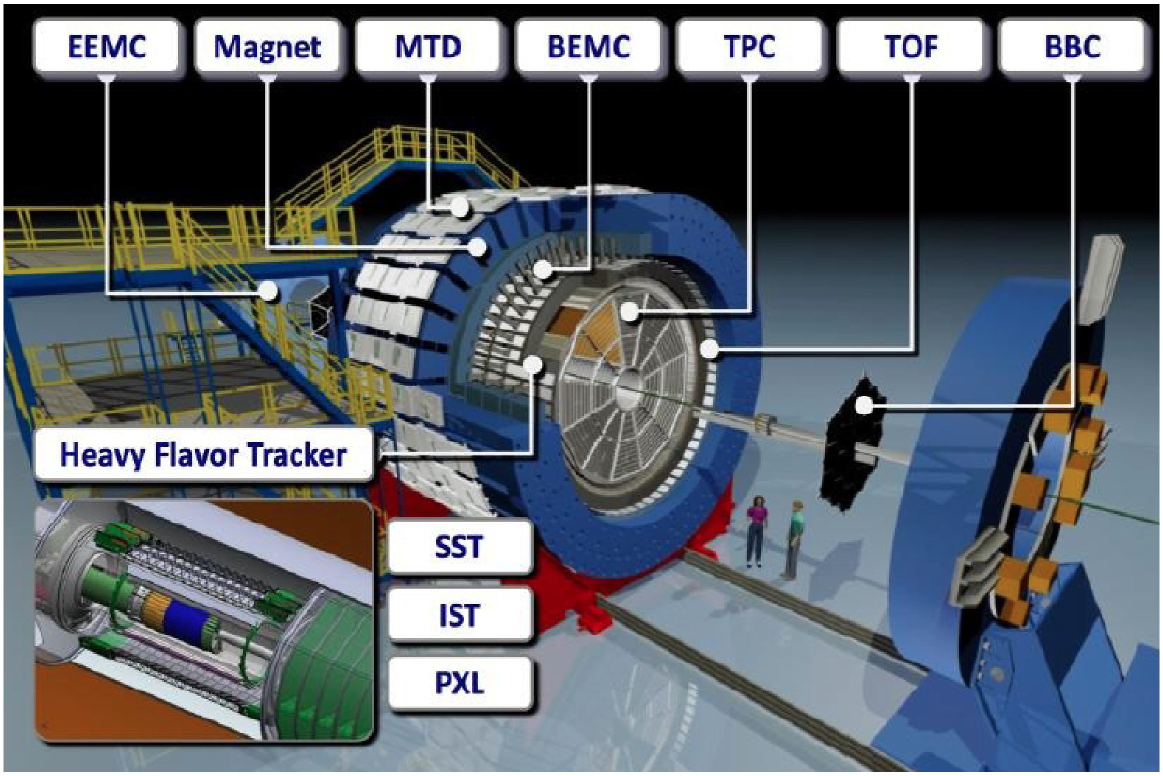

Figure 2.3: (Color online) Three-dimensional view of the STAR detector.

The three-dimensional schematic layout of the STAR detector system, which was configured for operation in the year 2014, is shown in Figure 2.3. At the heart of STAR is the Time Projection Chamber (TPC). It is a cylindrical detector which enables particle tracking and identification via track ionization energy loss [61]. The beam crossing point is at the center of TPC and the direction of the beam is the Z-direction [62]. Between TPC and the beam pipe, we have the Heavy Flavor Tracker (HFT), which is a silicon-based tracking detector [63]. It helps in precise vertex measurements. Surrounding the TPC is the Time-of-Flight (TOF) detector [64]. It extends particle identification capabilities at STAR to above 1 GeV/c. Beyond TOF is the STAR calorimeter system, consisting of the Barrel ElectroMagnetic Calorimeter (BEMC) and the Barrel Shower Maximum Detector (BSMD) [65]. The End-cap ElectroMagnetic Calorimeter (EEMC) on one side of STAR [66], with the BEMC and BSMD allow for the measurement of transverse momentum of photons, electrons and electro-magnetically decaying hadrons. The BEMC is surrounded by the STAR magnet coils and Iron York [67]. This room temperature solenoidal magnet provides a uniform magnetic field of 0.5 T along the beam line. The outermost cylindrical layer is the Muon Telescope Detector (MTD), which provides for an excellent muon trigger and identification capabilities at mid-rapidity [68].

Apart from these, STAR houses several other sub-detectors for beam monitoring and triggering. The Beam Beam Counters (BBC) are located 3.5 m away from the center of STAR on either side and monitor event rates in $p + p$ collisions [69] [70]. A pair of Zero Degree Calorimeter (ZDC) detectors, located along the beam pipe on both sides, monitor small-angle scattering of neutral particles such as spectator neutrons [69]. The Vertex Position Detectors (VPD) are located at Z = ± 5.6 m on either side. These provide the start time of the collisions, which is essential for time-of-flight measurements [64].

The various detector sub-systems are discussed in detail in the following subsections.

2.2.1 Heavy Flavor Tracker

Heavy Flavor Tracker (HFT) is a group of inner tracking detectors which are designed to facilitate the reconstruction of displaced decay vertices of heavy flavor hadrons with a pointing resolution of 50 μm [63]. It covers a pseudorapidity range of ± 1 and 2π in azimuth. This helps extend STAR's capabilities by providing direct topological identification of hadrons containing charm and bottom quarks. HFT consists of three sub-detectors, a silicon pixel detector (PIXEL), the Intermediate Silicon Tracker (IST) and the Silicon Strip Detector (SSD). The schematic of the configuration is shown in Figure 2.4.

The SSD lies at a radius of 22 cm with a length of 106 cm. It comprises of double-sided silicon strip wafers with a pitch of 95 μm. Inside the SSD, lies IST at a radius of 14 cm. It is a single-sided double metal silicon pad that is designed to match the high resolution of the PIXEL detector with the coarser resolution of the SSD. With a 600 μm $\times$ 6 mm pitch, the IST has a length of 50 cm. Two layers of low mass PIXEL detectors are built at a radius of 2.8 cm and 8 cm, with a length of 20 cm and 20.7 μm pitch. Each ladder contains a row of 10 monolithic Complementary Metal Oxide Semiconductor (CMOS) detector chips and

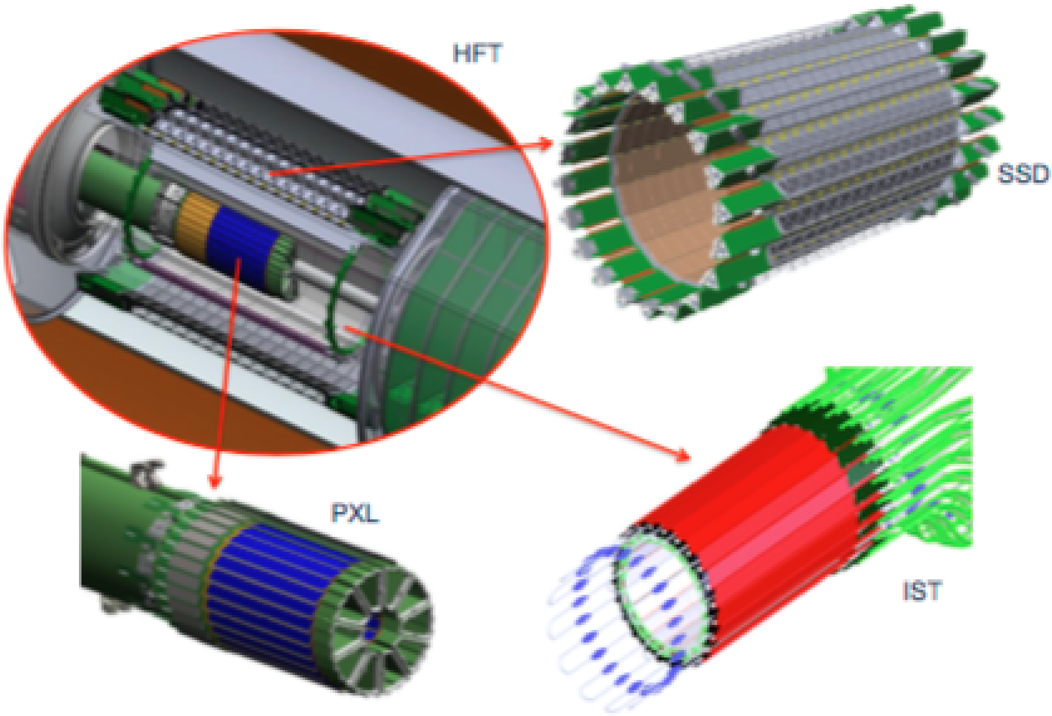

Figure 2.4: (Color online) A schematic drawing of the Heavy Flavor Tracker.

has an active area of 19.2 cm × 1.92 cm [71]. A summary of technical details of the three sub-detectors is given in Table 2.2.

2.2.2 Time Projection Chamber

The Time Projection Chamber (TPC) is the primary tracking device used to identify charged particles through ionization energy loss as they traverse through the gas volume [61] [72]. The schematic diagram of TPC is shown in Figure 2.5 [61]. The TPC covers an acceptance of ±1.8 units of pseudorapidity and 2π in the azimuthal angle. It is 4.2 m long, along the beamline, and 4 m in diameter. The Outer Field Cage (OFC) and the Inner Field Cage (IFC) has a radius of 200 cm and 50 cm respectively. The region enclosed by the OFC, IFC and the end caps on both sides is filled with P-10 gas, which is a mixture of 90% argon and 10% methane. The TPC is divided into two drift volumes, each of 210 cm, by a central membrane, which serves as the cathode. The central membrane has a 28 kV negative potential applied

Table 2.2: Technical details of HFT

Sub-detector	r (cm)	Resolution R/ϕ – Z (μm)	X/X_0 (%)
PIXEL	2.8	12 – 12	0.4/layer
	8	12 – 12	0.4/layer
IST	14	170 – 1800	< 1.5
SSD	22	20 – 740	1

to it. The end caps, at ground potential, serve as anode and host readout systems. The field cages are segmented into a total of 182 conducting rings, biased by 2 MΩ resistors between the rings. The field cage, central membrane and the end caps together provide a uniform electric field of 133 V/m pointing towards the center ($Z = 0$) of the TPC from both the ends ($Z = \pm 210$ cm). Under the influence of this electric field, the electrons from the ionization of P10 gas by charged tracks drift towards the ends of the TPC with a velocity of 5.45 cm/μs, translating to a maximum of about 40 μs of total drifting time.

The readout of the TPC endcap planes is based on Multi-Wire Proportional Chambers (MWPC) [61]. The MWPC chambers are composed of three layers of wire planes and a pad plane each. For each end cap, 12 readout modules, also called sectors, are arranged radially, with a gap of 3 mm between them. Each sector is further divided into inner and outer subsector. The inner subsector consists of smaller pads, distributed in 13 pad rows, in order to optimize the position and two-track resolution in a region with high particle density. The outer subsectors are packed into 32 rows per sector to maximize the measurement of energy loss in a region with relatively lower particle density. One full sector of anode is shown in Figure 2.6 [61]. A track in TPC can, therefore, be sampled by a maximum of 45 pad rows. The central membrane cathode consists of 70 μm thick carbon-loaded Kapton film, which has 36 aluminium stripes attached to each side. These are used as targets for the TPC laser calibration system.

The main function of the TPC subsytem in STAR is track reconstruction and particle

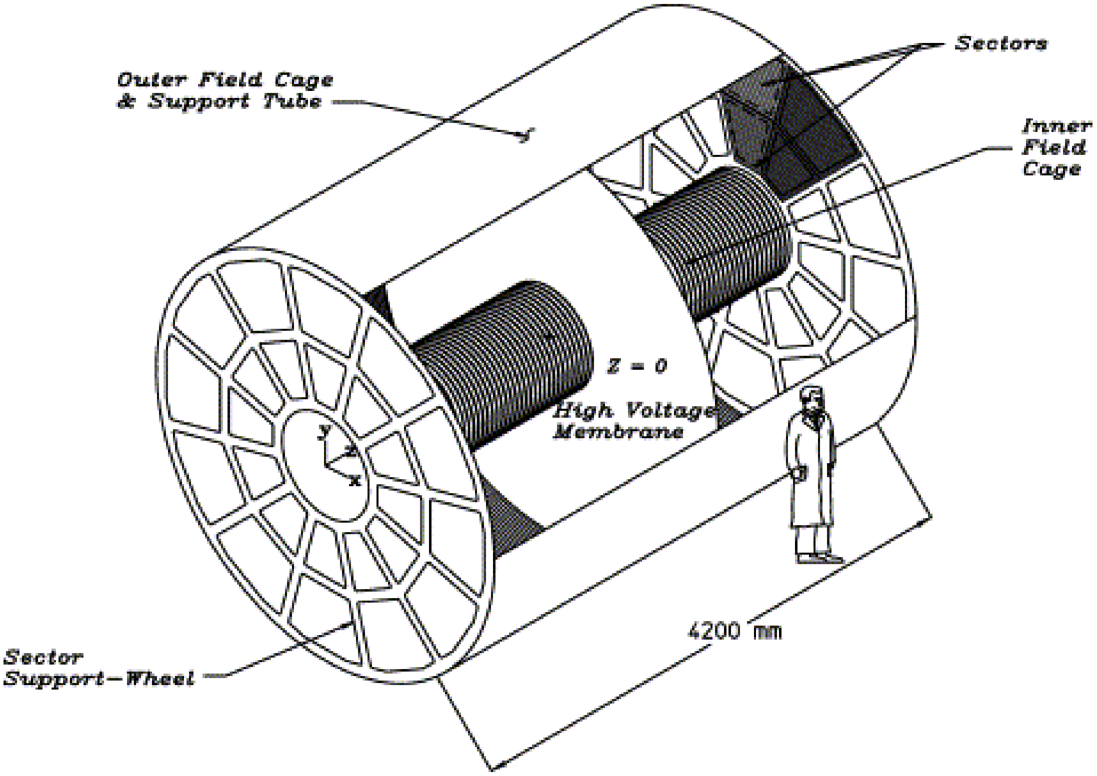

Figure 2.5: A schematic drawing of the Time Projection Chamber.

identification. Charged particles traversing the TPC follow a curved path due to the presence of magnetic field. Along its track, it ionizes the P10 gas leaving behind clusters of electrons. Assuming Gaussian response function for the pads, the $X - Y$ position of the cluster is determined by measuring the signal in adjacent pads and fitting to find the most likely position. The drift time of the electron cluster from the point of origin to the end caps is used to determine the Z position. The Time Projection Chamber Tracker algorithm is then used to reconstruct the track using a helical trajectory fit. The Z position of the collision vertex is determined by extrapolating the reconstructed trajectories to the origin. A track is called a primary track if its distance of closest approach (DCA) from the reconstructed vertex is within 3 cm, otherwise it is called a global track. The reconstruction efficiency for primary tracks depends on the track quality cuts, particle type and track multiplicity. The transverse momentum, p_T, is determined using the following equation:

$$p_T = 0.3\, B\, r\, q \tag{2.1}$$

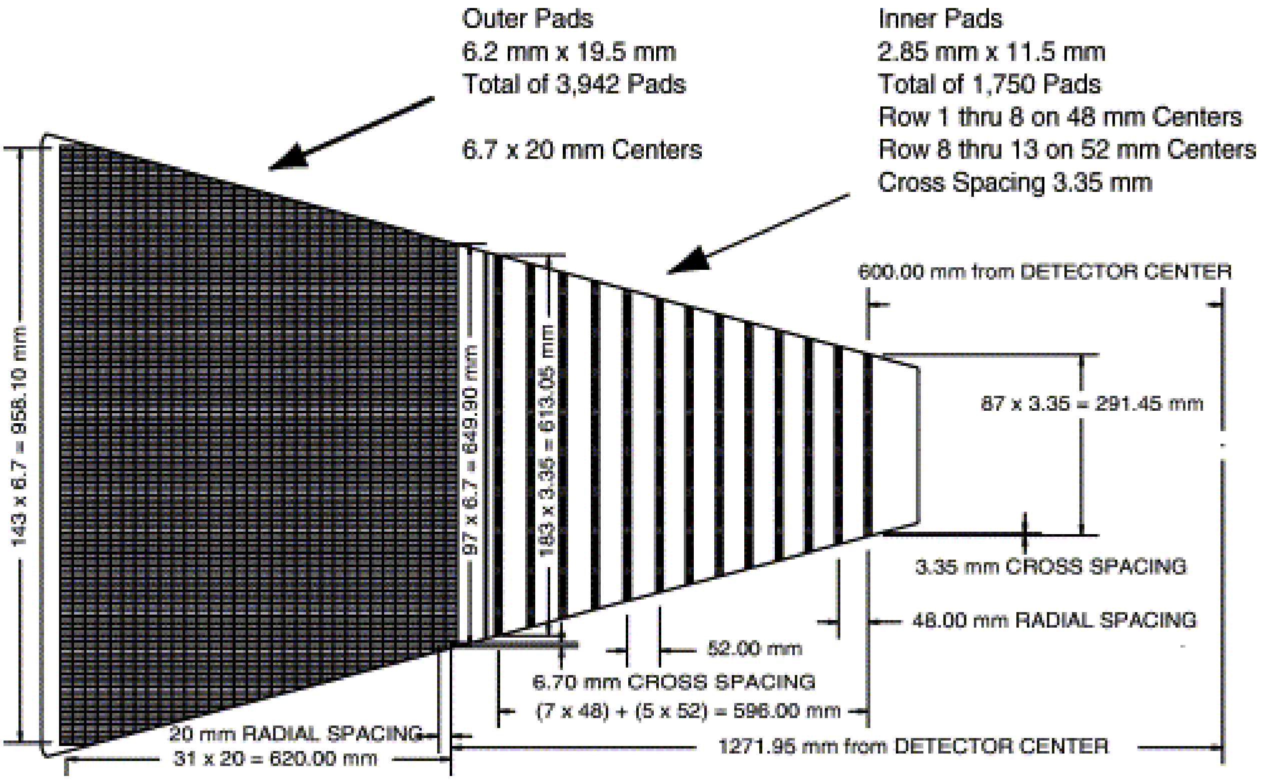

Figure 2.6: A schematic drawing of a sector of the TPC anode plane indicating the inner and outer subsectors and their respective padrows.

where B is the magnetic field strength, r is the radius of curvature of the reconstructed track helix, and Q is the charge of the particle. The components of the three-momentum of the primary track can then be calculated using the angle made by the track with respect to the Z-axis of the TPC.

The ionization energy loss (dE/dx) of the charged particles due to interaction with the medium inside TPC is used for particle identification. The value of dE/dx for the track is extracted from the energy loss measured from the maximum of 45 pad rows. As the length over which the particle energy loss is measured is short and the fluctuations are large, instead of average dE/dx, the most probable energy loss is measured by calculating the truncated mean of 70% of the of the clusters. Figure 2.7 shows a typical plot of measured dE/dx as a function of track momentum. The solid lines are the prediction from the Bischel function for different particle species [73]. The typical resolution of dE/dx in Au+Au collisions is $\sim$ 8%, which makes separation of pions (π) and kaons (K) upto a momentum of 0.6 GeV/c

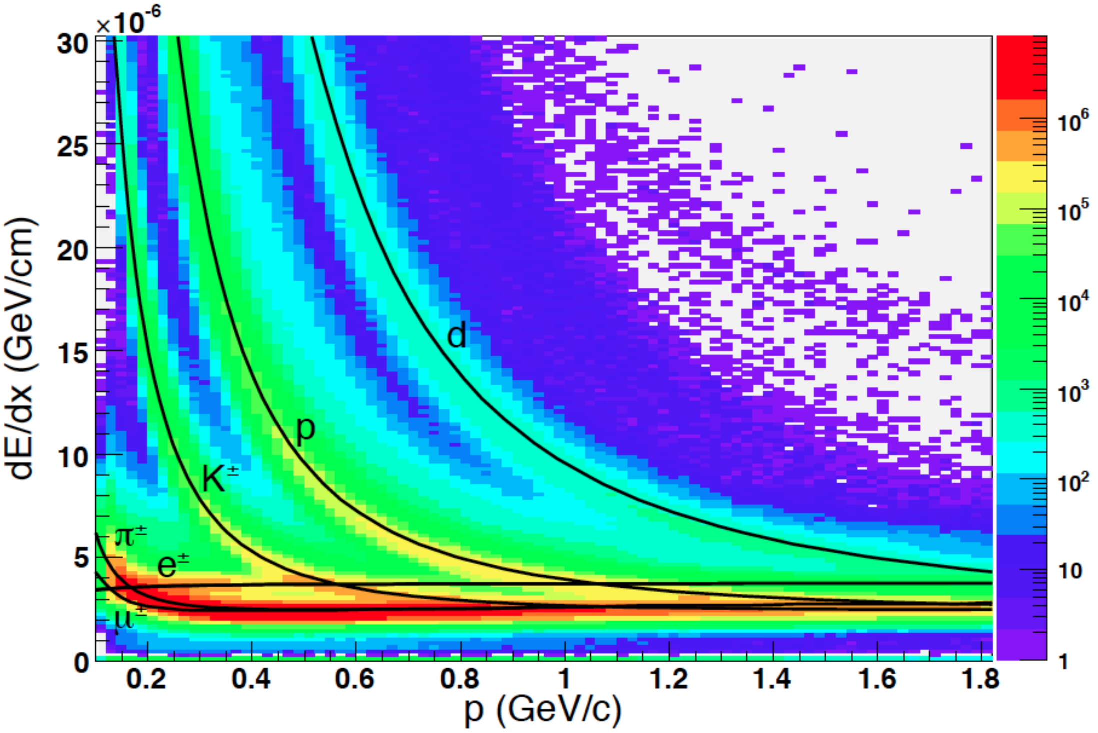

Figure 2.7: (Color online) The energy loss distribution for charged particles from TPC as a function of momentum.

and K and protons (p) upto 1.1 GeV/c.

2.2.3 Time of Flight detector

The Time of Flight (TOF) detector extends particle identification capabilities at STAR to higher momentum [64] [74] [75]. TOF is segmented into 120 trays and surrounds the TPC cylindrically. Each tray is 2.4 m long, 21.3 cm wide, 8.5 m deep and covers an azimuthal angle of 6 degrees around the TPC. It consists of 32 Multigap Resistive Plate Chamber (MRPC) [76] modules along the Z direction, which are a stack of resistive plates arranged in parallel, creating a series of gas gaps. The dimensions of a module are 94 mm × 212 mm × 12 mm with an active area of 61 mm × 200 mm. A cross-section view of the MRPC module is shown in Figure 2.8(a). A strong electric field is generated in each subgaps by the external electrodes. These are made of graphite tapes and applied to the outer surfaces of

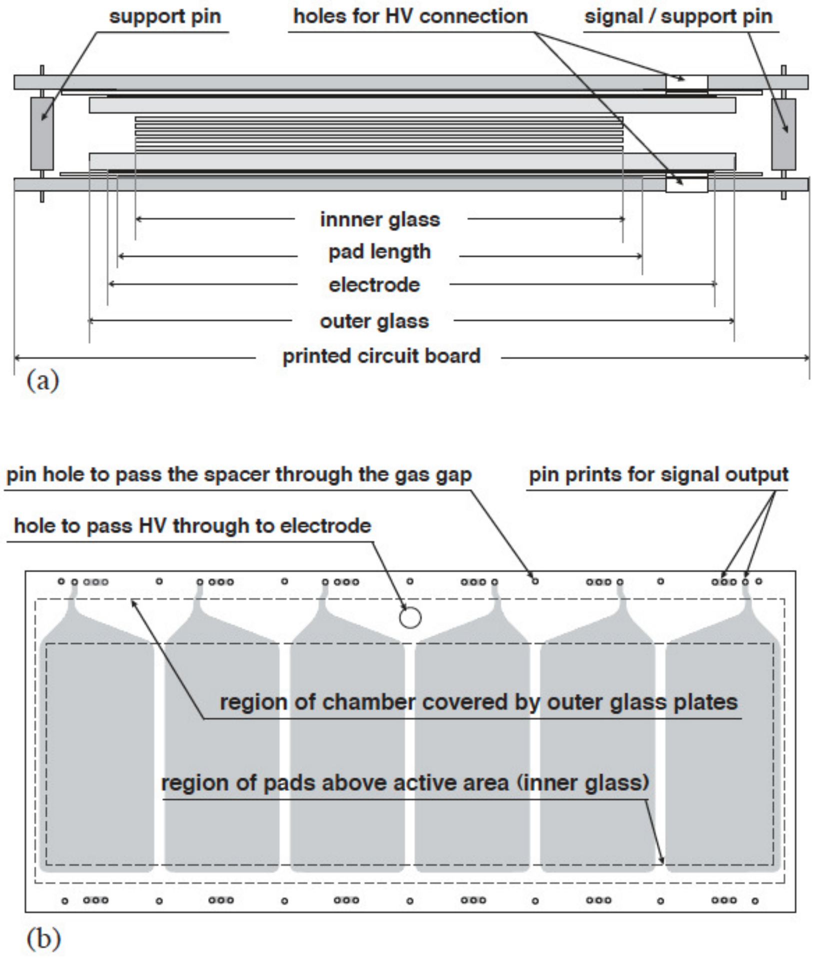

Figure 2.8: (a) A schematic drawing of a cross-section of the MRPC module for TOF. (b) Top view of the printed circuit board with the readout pads array.

the two outer plates. The outer and inner glass plates are kept parallel using a 220 μm nylon fishing line. The plates, being resistive, are transparent to the signal induced by avalanches generated by the traversing charged particles. The signal read out with a 1 × 6 array of copper pickup pad is the sum of the signals from all the gas gaps. Figure 2.8(b) shows the readout pad array [75].

The TOF trays, in conjunction with the Vertex Position Detectors (VPD), form the TOF detector subsystem [64]. The VPD provides the common start time of the event, while the TOF trays provide the stop time for each track. The difference between the two times gives the time of flight (τ) of the associated track. The time resolution for TOF is 80 to 100 ps.

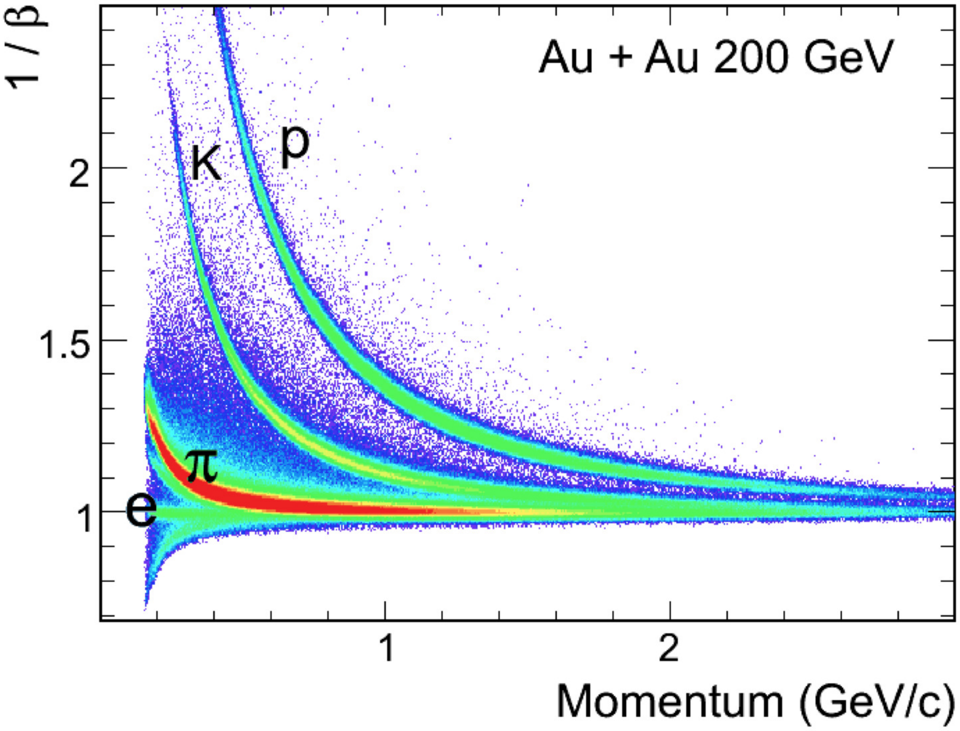

Figure 2.9: (Color online) $1/\beta$ as a function of track momentum from TOF.

Using τ, the relative velocity of associated track (β) can be estimated using the following equation:

$$\beta = L\,/\,c\,\tau \tag{2.2}$$

where L is the length of the track traversed by the particle and c is the speed of the light. The mass (m) of the particle associated with the corresponding track is then given by the following relation:

$$m = p\,/\,\gamma\,\beta\,c \tag{2.3}$$

where $\gamma = 1/\sqrt{1-\beta^2}$. The track momentum, p is measured by the TPC. Figure 2.9 shows $1/\beta$ as a function of momentum for different tracks. Using TOF, π/K and K/p can be distinguished upto 1.6 and 3.0 GeV/c respectively.

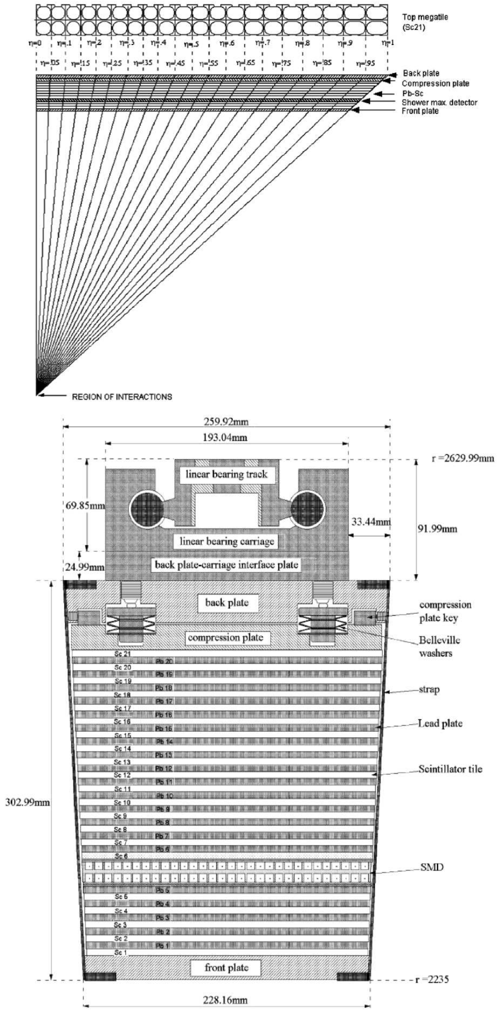

Figure 2.10: A schematic drawing of the side (end) view of a BEMC module in the upper (lower) plot.

2.2.4 Electromagnetic calorimeters

The Barrel ElectroMagnetic Calorimeter (BEMC), with the Endcap ElectroMagnetic Calorimeter (EEMC) and the Barrel Shower Maximum Detector (BSMD) constitute the electromagnetic calorimeter subsystem in the STAR detector system. The BEMC [65] is cylindrical in shape with an inner radius of 223.5 cm and an outer radius of 263 cm. It consists of 120 modules, two halves each of 60 modules. One module covers a pseudorapidity range of 1 unit and and azimuthal angle of 6 degrees. Figure 2.10 shows a BEMC module, which is a stack of 21 layers of plastic scintillators with 20 layers of lead sandwiched between them [65]. At mid-rapidity, it forms a total depth of approximately 20 radiation lengths. Each module is further segmented into 40 towers. One photomultiplier tube is used to read out the sum of light output from 21 layers of plastic scintillators for each tower.

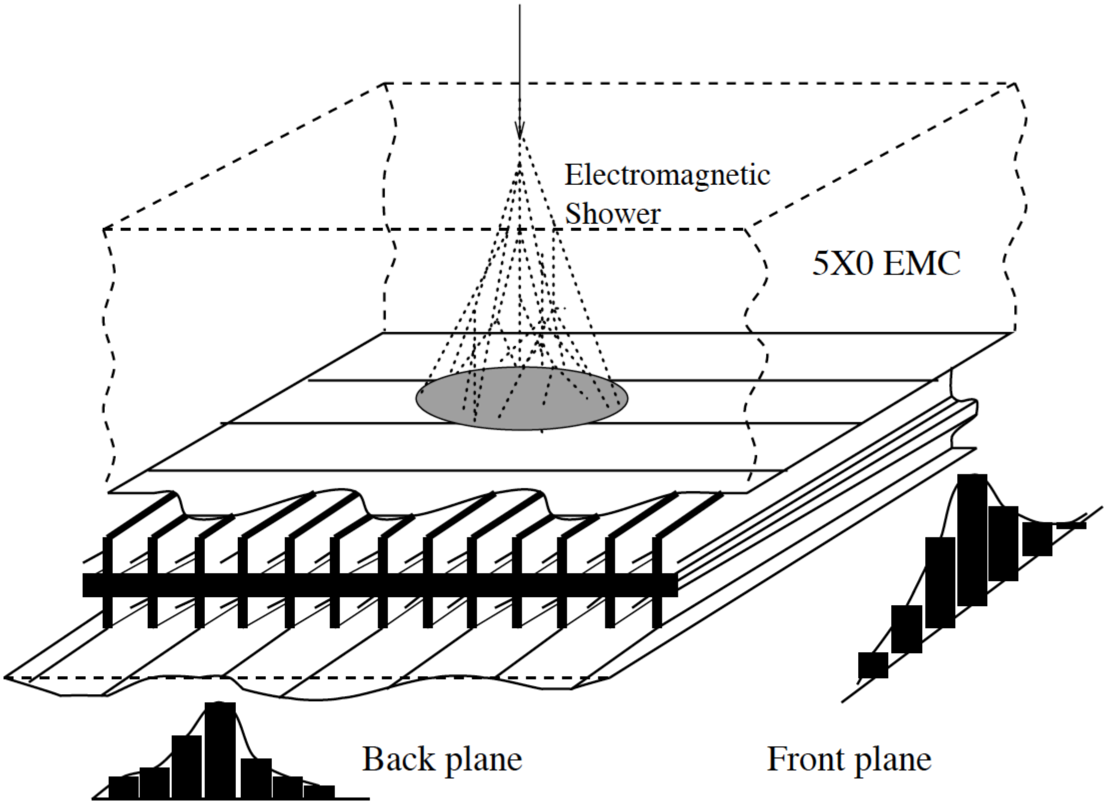

Figure 2.11: A schematic drawing of the BSMD at STAR.

The BSMD [65] is located between the fifth layer of lead and sixth layer of scintillator inside the BEMC. Each module of BSMD, shown in Figure 2.11, is a wire proportional counter sandwiched between two layers of strip readout. There are 150 strips on each of the two planes of the BSMD module. The front plane maps out the shower profile along η with a very fine resolution, while the ones on the back provide fine granularity in the ϕ direction.

The EEMC [66] is a lead-scintillator sampling calorimeter, with 60 azimuthal and 12 radial segments. It allows for measurements in the forward direction, $1 < \eta < 2$, with the full azimuth. The schematic diagram of a part of EEMC is shown in Figure 2.12. A scintillator strip SMD with high position resolution is located after the fifth radiator plate.

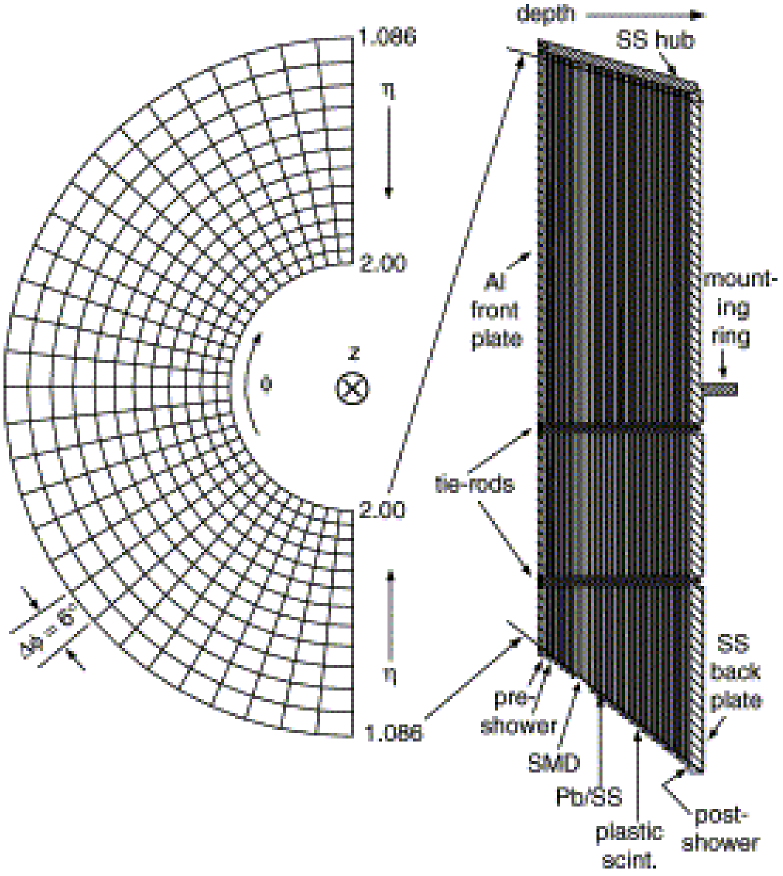

Figure 2.12: A schematic drawing of the EEMC at STAR.

Light from the towers and SMD is carried on optical fibers outside the STAR magnet, to photomultiplier tubes mounted on the rear of the poletip. The EEMC is supported from a strong stainless steel backplate, which attaches to the poletip, and a terraced, conical stainless steel hub at the inner radius, to which the radiator sheets are attached.

2.2.5 Muon Telescope Detector

The Muon Telescope Detector (MTD) [68], the outermost detector subsystem at STAR, is located behind the iron return bars of the STAR magnet. It covers 45% of the full azimuth at midrapidity $-0.5 < \eta < 0.5$. The MTD is based on the Multi-gap Resistive Plate Chambers (MRPC) technology [76], which is similar to that of TOF, but much larger in size and have long double-ended read-out strips. MTD consists of a total of 118 modules with 1416 readout strips and 2832 readout channels. The length of each strip is 87 cm. The spatial resolution

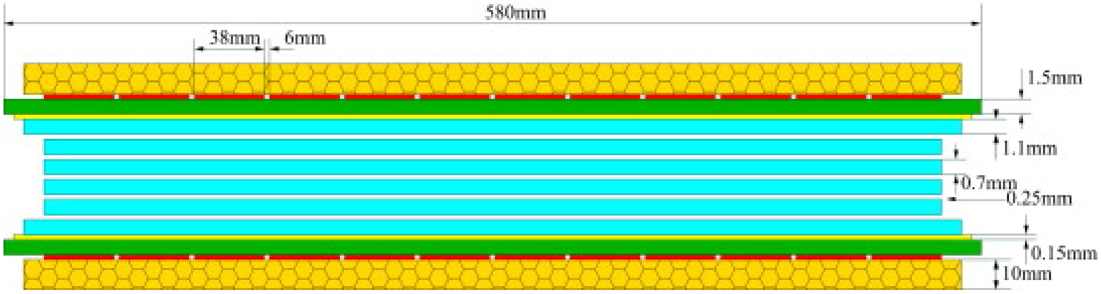

Figure 2.13: A schematic drawing of the side view of a MRPC module for MTD.

is about 1 cm and the intrinsic timing resolution is less than 100 ps. Figure 2.13 shows a the end view of a long MRPC module. The gas mixture used is a mixture of 95% Freon R-134a and 5% isobutane. The MTD allows the measurement of the Υ and J/ψ mesons, over a broad transverse momentum range through di-muon decays.

2.2.6 Trigger detectors

The Zero Degree Calorimeters (ZDC), the Beam Beam counters (BBC), the Vertex Position Detectors (VPD) and the ElectroMagnetic Calorimeters (EMC) are the main trigger detectors at STAR. As the various detector subsystems have different readout speeds, these fast detectors forms Level-0 trigger that initiates the data acquisition (DAQ) sequence.

Located at the distance of ± 18.25 m from the center of TPC along the beam axis, the two ZDC detectors [69] are hadronic calorimeters designed to measure the energy deposited by the spectator neutrons in a small angle near zero degrees ($\theta < 2$ mrad). A coincidence between the two ZDC, with summed signal greater than 40% of a single neutron signal, is required for minimum bias trigger.

The BBC [69] [70] is located on each side of the TPC, covering full azimuthal angle, and $2.1 < |\eta| < 5.0$. This hexagonal scintillator array structure is mounted around the beam pipe at a distance of 3.7 m from the center of TPC along the beam direction. A coincidence between the two counters is required for the minimum bias trigger. This coincidence is also used to reject beam gas events. The timing difference between the BBC is used to obtain information about the position of the collision vertex. In addition, the small tiles of BBC can also be used to reconstruct the first order event plane for flow measurements.

The VPD [64] [74] consists of 19 lead converters plus plastic scintillators with photomultiplier tube readout. These are located at 5.7 m on either side of the interaction point and cover the pseudorapidity range of $4.24 < |\eta| < 5.1$. Like BBC, a coincidence in the east and west VPD is used for the selection of minimum bias events. It also provides information about the Z-component of the collision vertex, with a better timing resolution than BBC.

The EMC is used to trigger events with rare probes with high electromagnetic energy deposition in the EMC tower or patch, arising from high energy photons and neutral pions, or electrons from J/ψ decays.

The results presented in this thesis are based on the data collected for Au+Au collisions by the STAR detector in the years 2010, 2011 and 2014. The information from TPC and TOF is used for particle identification and trigger from VPD is used to select minimum bias events.

CHAPTER 3

Study of local parton density fluctuations through baryon clustering

3.1 Introduction

Local density fluctuations have been a defining feature among the first-order phase transitions observed around us, for example the condensation of water vapor, transformation from paramagnetic to ferromagnetic material, etc. In the QCD phase diagram, model calculations predict the transition from the Quark-Gluon Plasma phase to the Hadron Gas phase to be a first-order phase transition for large baryon chemical potential that ends in a second-order critical point [24]. Hence, probing for signatures of local parton density fluctuations would provide an insight into the proposed critical phenomenon in QCD.

Fragmentation and recombination have been successful models in explaining particle productions in heavy-ion collisions [77] [78] [79]. In the fragmentation picture, perturbative QCD is used to describe the formation of hadrons from a single parton that fragments into a shower of particles. The produced hadrons will only have a fraction of momentum of the fragmenting parton. Alternatively, in the recombination framework, or the coalescence mechanism of particle production, a hadron is formed when the constituent partons in the Quark-Gluon Plasma come sufficiently close both in space and in momentum space. In this case, the momentum of the hadron is the sum of its constituents. The Number of Constituent Quark (NCQ) [27] scaling observed from the elliptic flow measurements in heavy-ion collisions hint at coalescence being a dominant mode of particle production at low momentum. Within the coalescence picture, the baryon formation probability can be influenced by these local parton density fluctuations, thereby leading to clusters and voids in the phase-space distribution of hadrons.

In order to probe the local parton density fluctuations in heavy-ion collisions, we propose to study the distribution of the ratio of the multiplicity of particles produced in an azimuthal region to the total number of particles produced in the event. We expect the shape of this self-normalized distribution to be sensitive to clustering in the local phase space.

In this chapter, the qualitative sensitivity of the proposed observable is studied using a simple Monte-Carlo model. The measurements of the cumulants of the distribution of the aforementioned ratio for protons using the data from Au+Au collisions from the STAR Beam Energy Scan program is presented. The observations are compared with various baselines, like mixed event, and Poisson distribution of produced particles, to demonstrate the sensitivity of our approach to possible clustering and parton density fluctuations in heavy-ion collisions.

3.2 The observable

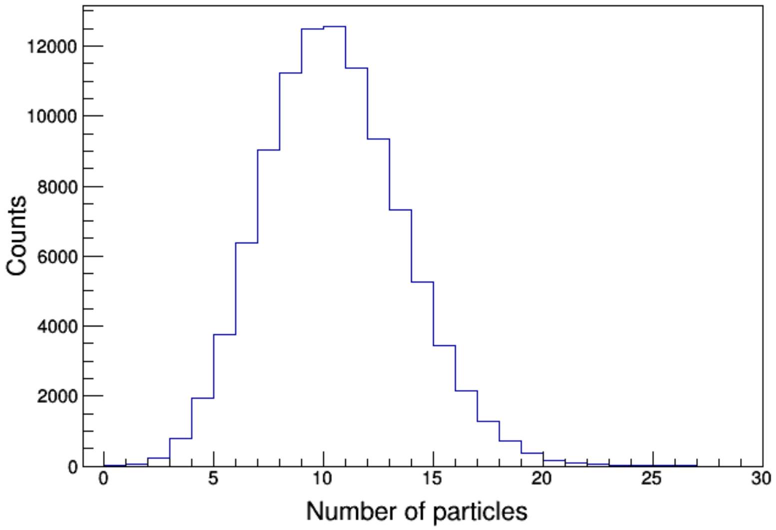

Figure 3.1: Event-by-event distribution of the simulated particles assuming Poisson distribution with mean 10.

In order to probe baryon density fluctuations in relativistic heavy ion collisions, the azimuthal plane is divided into different angular regions and the distribution of the ratio of protons in a region to the total number of protons in the event is studied. The parameter of interest is the ratio R, is given by

$$R = \frac{N_i}{N_1 + N_2 + \cdots + N_m} \tag{3.1}$$

where N_i is the number of protons in the angular region i and m is the total number of divisions of the azimuthal plane. The shape of this self-normalized distribution is expected to carry possible clustering information. Hence, the cumulants of the event-by-event distribution of R is defined as our observable.

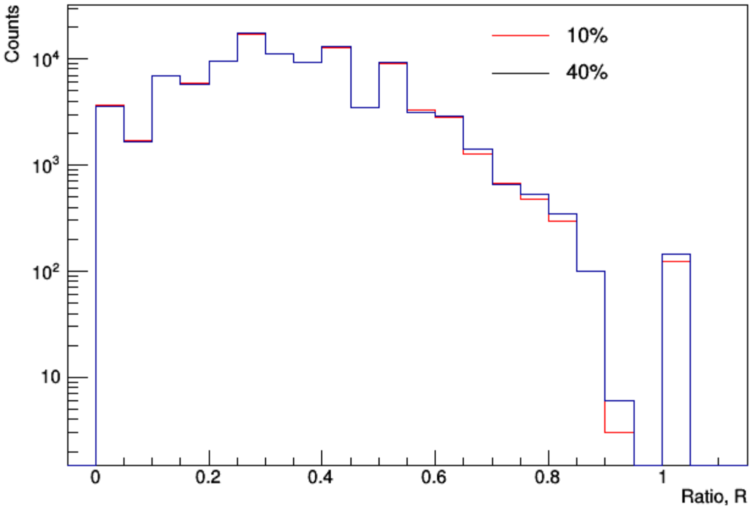

Figure 3.2: Event-by-event distribution of the ratio R for different probability of clustering in the event. The simulated particle distribution is Poisson distribution with mean 10 and the number of azimuthal divisions is 3. Around 10% of the total particles cluster an event. If an event does not cluster, all particles are distributed randomly.

Through a Monte-Carlo model, the variation of the cumulants of the distribution of R with the elements of the model, enumerated below, is studied.

1. The probability of clustering in an event
2. The percentage of protons that will cluster, given there is clustering in an event

3. The total number of angular divisions of the azimuthal plane

For these studies, 100,000 events are simulated, assuming a Poisson distribution, with mean 10, as event-by-event distribution of the particle of interest. Clustering is implemented by assigning a certain percentage of total particles to a randomly selected azimuthal division; all other particles are distributed randomly across the azimuth. If an event does not cluster, all particles are distributed randomly. Figure 3.1 shows the event-by-event distribution of the particles.

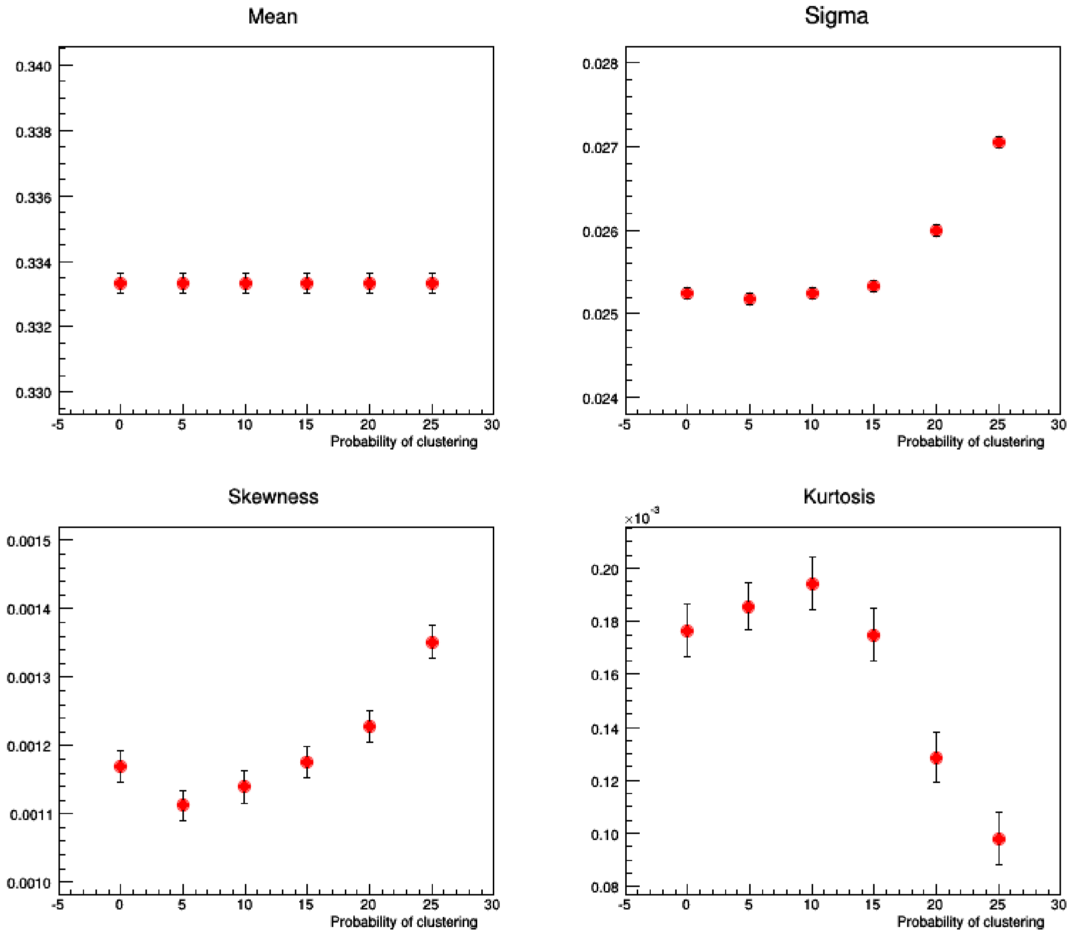

Figure 3.3: Variation of cumulants with probability of clustering. The simulated particle distribution is Poisson distribution with mean 10 and the number of azimuthal divisions is 3. Around 10% of the total particles cluster an event. If an event does not cluster, all particles are distributed randomly.

Effect of probability of clustering

The probability of clustering gives whether or not clustering will occur in an event. In order to study the effect on the observable, the number of azimuthal divisions is fixed to be 3 and the percentage of particles that cluster in an event to 10%. Figure 3.2 shows the distribution of the parameter of interest, R, for different probabilities of clustering, ranging from 0% to 40%. Figure 3.3 shows the variation of the cumulants of the distribution of the self-normalized ratio, R, with the probability of clustering.

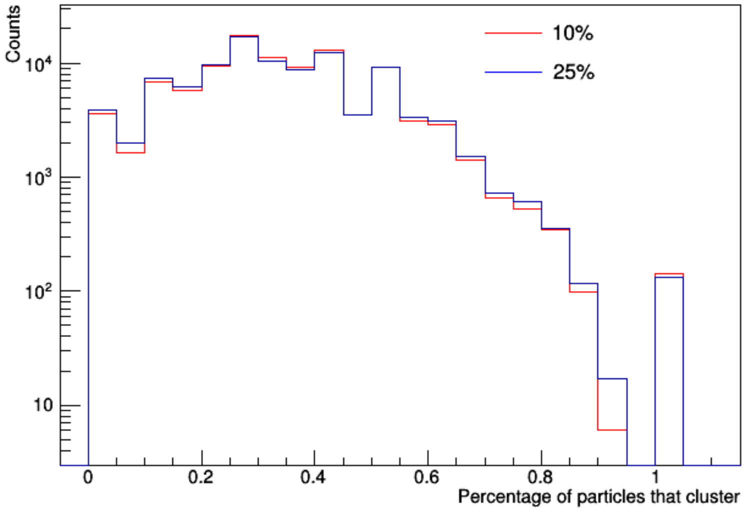

Figure 3.4: Event-by-event distribution of the ratio R for different probability of clustering in the event, that is whether or not particles in the event cluster. The simulated particle distribution is Poisson distribution with mean 10 and the number of azimuthal divisions is 3. Around 10% of the total particles cluster an event. If an event does not cluster, all particles are distributed randomly.

The percentage of particles that cluster

In order to simulate the percentage of particles that cluster, a randomly selected azimuthal bin is assigned to the determined fraction of particles. The remaining particles are distributed randomly across the azimuth. The sensitivity of the observable on the percentage of particles that cluster in an event is studied with the number of azimuthal divisions being 3 and the probability of clustering in an event being 40%. Figure 3.4 shows the distribution of the parameter of interest, R, for different percentages of particles clustering, ranging from 0% to 25%. Figure 3.5 shows the variation of the cumulants of the distribution of the self-normalized ratio, R, with the percentage of particles clustering.

The total number of angular divisions of the azimuthal plane

The total number of divisions across the azimuth will provide insights into angular correlation lengths. With the probability of clustering in an event being 40% and percentage of particles clustering being 10%, the distribution and variation of the cumulants of the ratio, R, for different number of azimuthal divisions is shown in Figure 3.6 and Figure 3.7 respectively.

3.3 Data Analysis

Beam Energy Scan data taken by the STAR Experiment in the year 2010 and 2011 for Au+Au collisions at $\sqrt{s_{NN}}$ = 7.7, 11.5, 19.6, 27, 39, and 62.4 GeV are analyzed.

3.3.1 Data sets

Minimum bias events, which are given by coincidence between the Vertex Position Detector and the Zero Degree Calorimeter, are used. Table 3.1 summarizes the energy, triggers and the total number of events that are used for analysis.

3.3.2 Event selection and centrality determination

A run at STAR refers to a group of around 2 million events. StRefmultCorr class within the STAR framework is a repository for the bad runs and centrality definitions for the different collision species and energies. Bad runs are eliminated using the StRefmultCorr class. In addition, runs with mean Z-vertex, mean reference multiplicity, mean transverse momentum, mean distance of closest approach, mean pseudorapidity, mean azimuthal angle beyond 3

Table 3.1: Triggers with corresponding number of minimum bias events

Energy	Year	Trigger number	Number of events
7.7	2010	290004	1.2 M
11.5	2011	310004, 310014	4.6 M
19.6	2011	340001, 340011, 340021	13.1 M
27	2011	360001	16.7 M
39	2010	280001	16.7 M
62.4	2010	270001, 270011, 270021	10.1 M

sigma of the average of all the runs for a particular collision energy are also removed. List of all the bad runs are given in Appendix 1.

Event selection cuts are applied on the primary vertex. It is required that the Z-vertex position reconstructed based on tracks from Time Projection Chamber (TPC) is within 50 cm of the STAR detector for Au+Au collisions at $\sqrt{s_{NN}}$ = 7.7 GeV and 30 cm for the others. Also, the radial distance of the primary vertex, which is $\sqrt{V_x^2 + V_y^2}$, is within 2 cm of the beam axis. The absolute difference between the vertices reconstructed from the Vertex Position Detector and the TPC should lie within 3 cm for collision energies above 27 GeV.

Charged primary tracks are used to determine the centrality of the collision. Atleast 10 hits in the TPC is required. The distance of closest approach from the primary vertex should be less than 3 cm. In order to avoid auto-correlations, tracks are selected for the pseudorapidity range of $0.5 < |\eta| < 1.0$ from the center of TPC. The multiplicity distribution thus obtained is compared with Glauber Monte-Carlo simulations to get the centrality of the event. These selection criteria correspond to RefMult2 centrality definition within the StRefmultCorr class. More discussions on the process of obtaining the centrality definition is given in Chapter 4.

3.3.3 Particle identification

The information from both TPC and Time of Flight (TOF) detectors are used to identify the protons. A minimum of 15 hits are required in the TPC for reconstruction of the track. Also, the ratio of the number of hits in TPC to the maximum number of hits possible should be greater than 0.52 and less than 1.05. Alteast 10 hits in the TPC is required for the measurement of energy loss of the particle. The distance of closest approach from the primary vertex is required to be less than 1 cm. The charge of the track is required to be ±1. The phase space of measurement is defined to be within the pseudorapidity of 0.5 from the center of TPC. Energy loss information from TPC is used for identification of protons within 0.4 and 0.8 GeV/c. The absolute value of $n\sigma_{proton}$, which compares the energy loss measured for the track to Bethe-Block calculations, is required to be less than 2. The mass-squared information from TOF in conjunction with energy loss in TPC is used for transverse momentum between 0.8 and 2.0 GeV/c and is chosen to lie between $0.8 < m^2 < 1.0$. Figure 3.8 and Figure 3.9 shows the particle identification capabilities at the STAR experiment.

3.4 Results and discussions

With the protons identified, their angular distribution is studied for Au+Au collisions at energies from the STAR Beam Energy Scan program. Figure 3.10 shows the event-by-event distribution of protons for 0-5% central Au+Au collisions for the different collision energies.

Figure 3.11 shows the event-by-event distribution of the ratio of protons in one azimuthal region to the total number of protons in the event for 0-5% central Au+Au collisions for the different collision energies, assuming 6 divisions across the azimuth. The results from the experiment is compared with model expectations assuming the proton distribution to be Poisson or Binomial, with the mean as in data, being distributed uniformly in the azimuthal direction. Figure 3.12 shows the first four cumulants of the above distribution. The first-cumulant, or mean, is 1/6 by construction. We find that as we go higher in the order of the cumulant, the difference between the model expectations and the experimental observations increase, implying higher-order cumulants to be increasingly sensitive.

In order to reliably account for detector efficiency, mixed event technique is employed. Within the framework of mixed events, several events with similar characteristics like centrality, event plane orientation and the position of collision vertex are superimposed. From this, the number of protons in the true event are sampled randomly. By using the mixed event technique, the effects of local parton density fluctuations are washed out, while preserving detection and reconstruction effects. For the purpose of further discussions, 100 events are superimposed to create the mixed event sample.

Figure 5.8 shows the variation of cumulants of the event-by-event distribution of the ratio of protons in one azimuthal region to the total number of protons in the event as a function of beam energy in Au+Au collisions for different centralities. The number of azimuthal divisions range from 3 to 6. We find that the cumulants are monotonic with beam energy. The differences in trends arising due to number of azimuthal divisions are prominent for higher-order cumulants. We find that the concavity of the curves for kurtosis change when we go from central to peripheral collisions for finer azimuthal divisions.

Figure 3.14 shows the variation of cumulants from the mixed event sample for the distribution of the ratio of protons in one azimuthal region to the total number of protons in the event as a function of beam energy in Au+Au collisions for different centralities. The number of azimuthal divisions range from 3 to 6. We find that the cumulants are again monotonic with beam energy. We find that the concavity of the curves for kurtosis remain the same when we go from central to peripheral collisions for finer azimuthal divisions. In addition, the values of cumulants remain similar for different centralities.

Figure 3.15 and Figure 3.16 shows the variation of the ratio of the cumulants as measured from data to those from mixed event samples with beam energy for different centralities. Figure 3.15 shows the comparison for azimuthal divisions ranging from 4 to 6. We find the trends and magnitudes of the ratio of the cumulants from data to mixed events to be similar for lower-order cumulants. The difference is considerable for kurtosis measurements. The trends remain monotonic. The deviation from 1 hints at local partonic density fluctuation. The comparison between data and mixed event samples for three azimuthal divisions is shown in Figure 3.16. It is found that the ratio of the first-, second- and third-order cumulants remain monotonic, while that of the fourth-order cumulant follows a non-monotonic trend.

3.5 Conclusion

In order to explore and understand critical phenomenon associated with the QCD phase diagram, in this chapter, an observable that may be sensitive to local parton density fluctuations is introduced. The sensitivity of the observable to density fluctuations is established using a toy Monte-Carlo model.

Within the framework of coalescence mechanism of particle production, the baryon formation probabilities are expected to be affected by local parton density fluctuations. This, in turn, would affect the azimuthal distribution of baryons. Hence, the introduced observable is studied in detail in the context of protons. The cumulants of the event-by-event distribution of the ratio of the number of protons in one azimuthal division to the total number of protons produced in an event is studied for Au+Au collisions for beam energies ranging from 7.7 GeV to 62.4 GeV for different collision centralities.

In the absence of a dynamical model including phase transition, not much can be extracted in regards to the magnitudes and trends observed. However, comparisons with mixed events measurements may be considered as a realistic baseline. The differences between the magnitudes and trends of the cumulants as obtained from data and mixed event sample hint at observation of local parton density fluctuations in relativistic heavy-ion collisions.

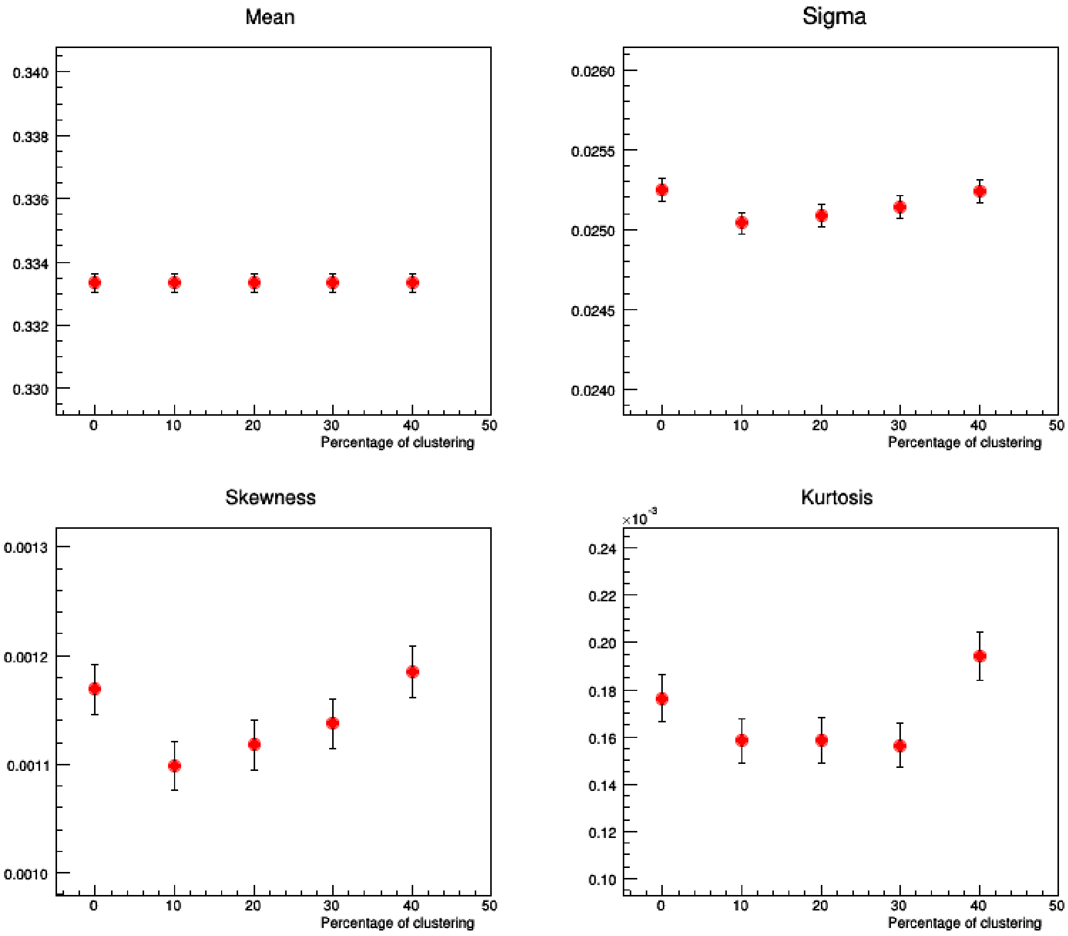

Figure 3.5: Variation of cumulants with probability of clustering. The simulated particle distribution is Poisson distribution with mean 10 and the number of azimuthal divisions is 3. Around 10% of the total particles cluster an event. If an event does not cluster, all particles are distributed randomly.

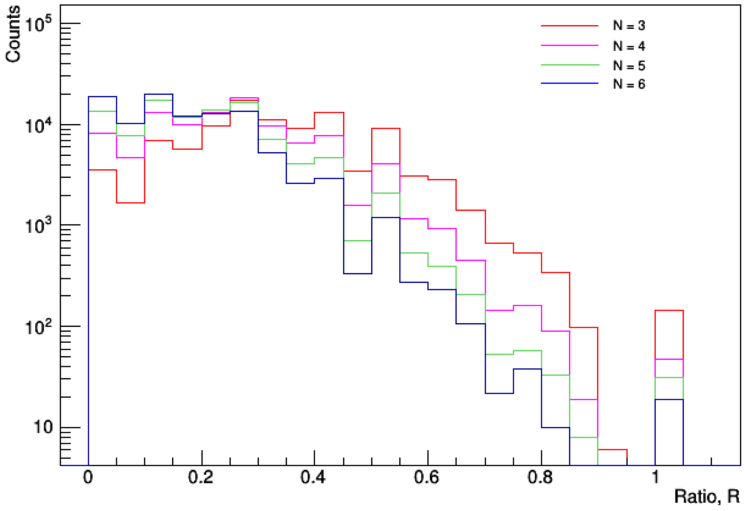

Figure 3.6: Event-by-event distribution of the ratio R for different number of azimuthal divisions. The simulated particle distribution is Poisson distribution with mean 10 and the probability of clustering in the event is 40%. Around 10% particles cluster an event.

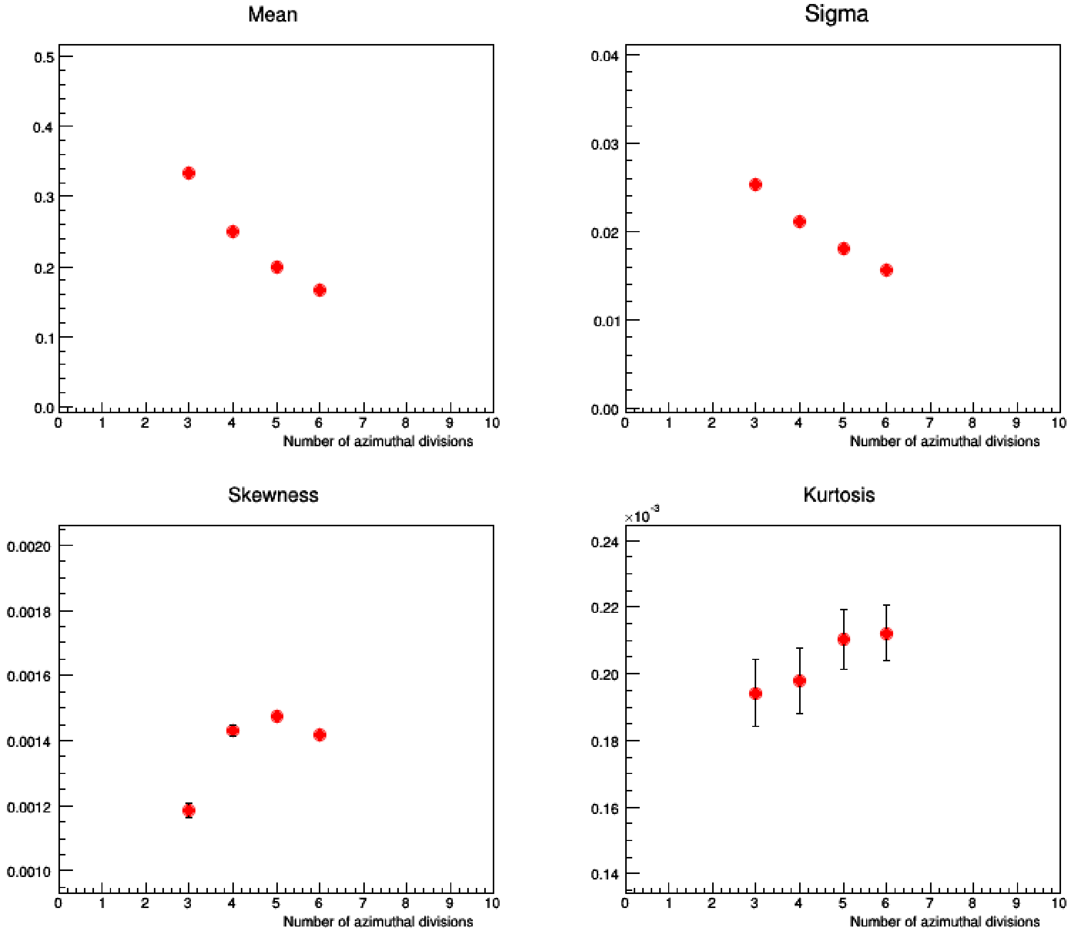

Figure 3.7: Variation of cumulants with number of azimuthal divisions. The simulated particle distribution is Poisson distribution with mean 10 and the probability of clustering in the event is 40%. Around 10% particles cluster an event.

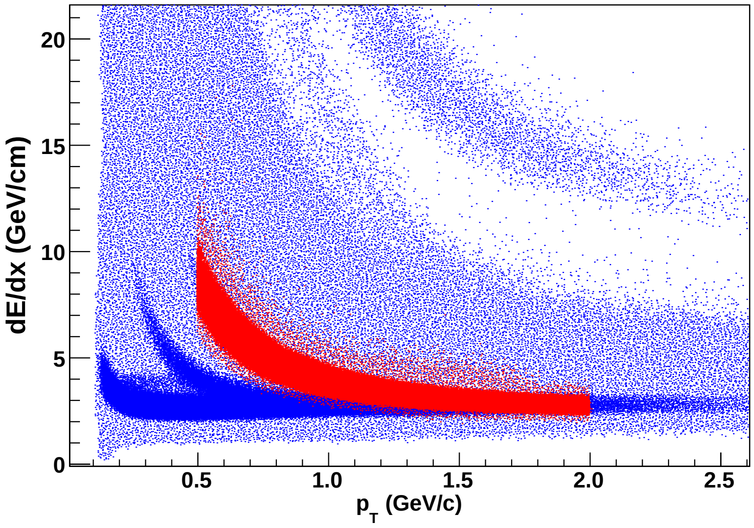

Figure 3.8: (Color online) Energy loss, dE/dx, as measured by TPC as a function transverse momentum. The yellow bands correspond to the selected proton tracks.

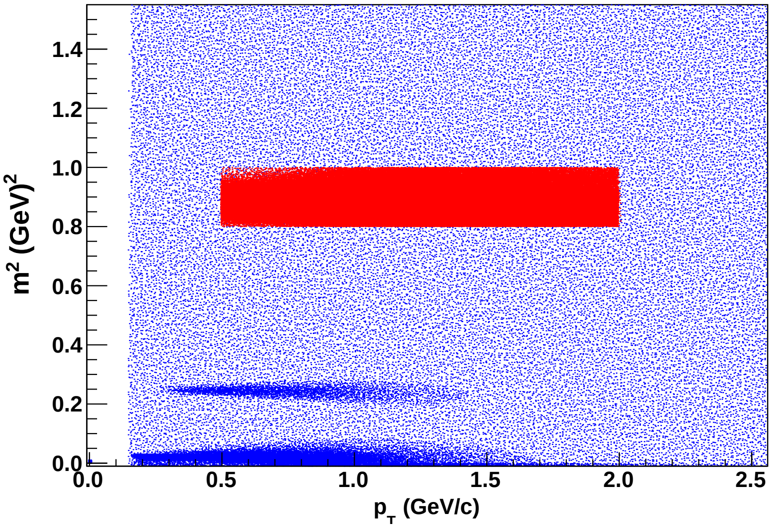

Figure 3.9: (Color online) Mass-squared, m^2, as measured by TPC as a function transverse momentum. The yellow bands correspond to the selected proton tracks.

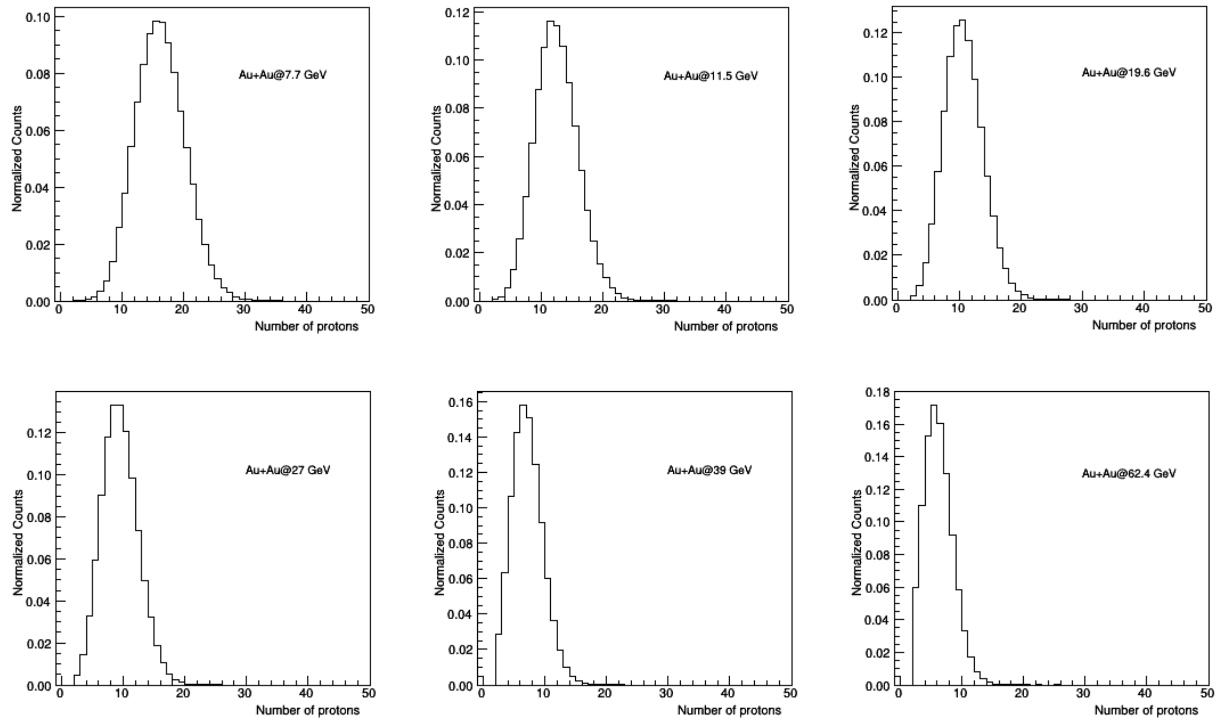

Figure 3.10: Event-by-event distribution of protons for 0-5% central Au+Au collisions for the different collision energies.

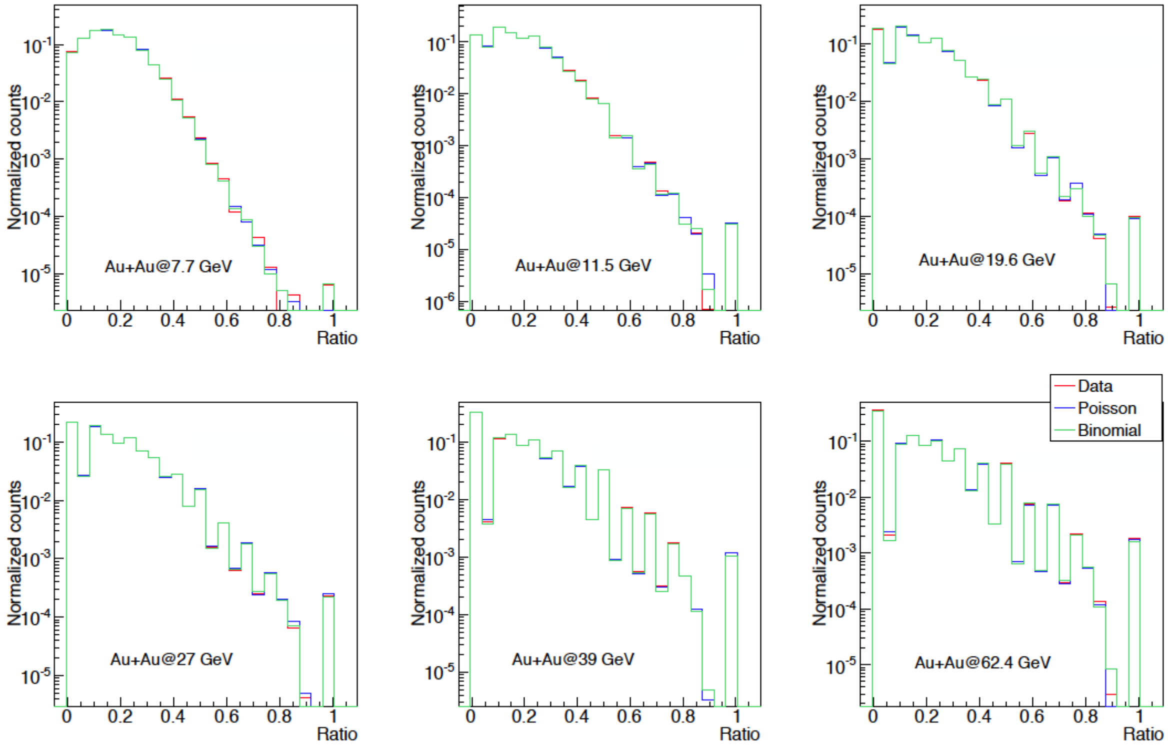

Figure 3.11: (Color online) Event-by-event distribution of the ratio of protons in one azimuthal region to the total number of protons in the event for 0-5% central Au+Au collisions for the different collision energies. The measurements are compared with baselines from Poisson and Binomial expectations.

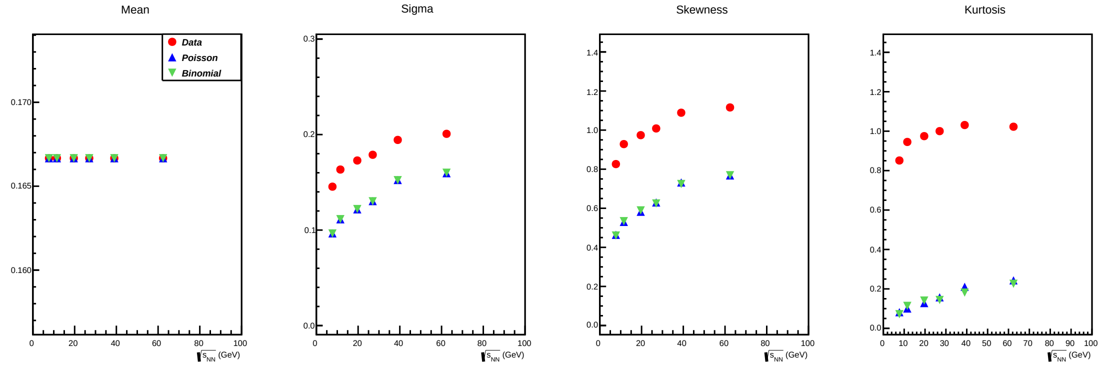

Figure 3.12: (Color online) Cumulants of the event-by-event distribution of the ratio of protons in one azimuthal region to the total number of protons in the event for 0-5% central Au+Au collisions for the different collision energies. The measurements are compared with baselines from Poisson and Binomial expectations, assuming uniform distribution across the azimuth.

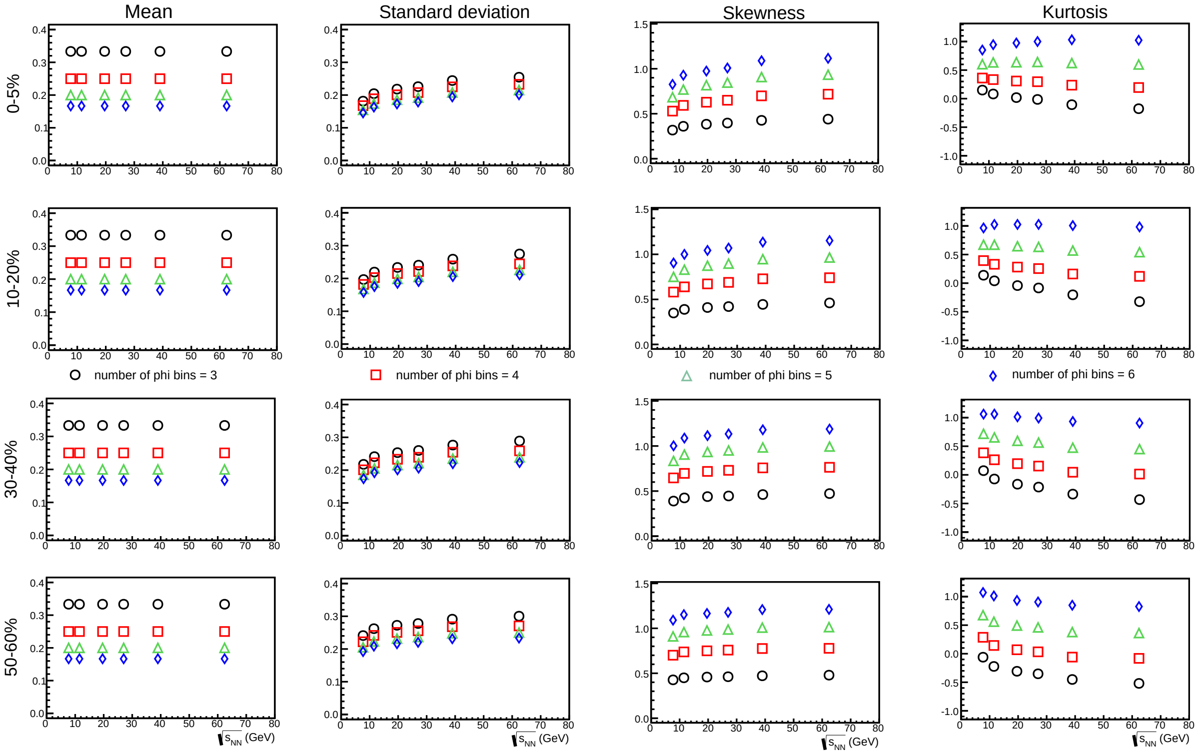

Figure 3.13: (Color online) Event-by-event distribution of the ratio of protons in one azimuthal region to the total number of protons in the event for Au+Au collisions as a function of collision energies for different centralities. The number of azimuthal divisions are given by black circles for 3, red squares for 4, green triangles for 5 and blue diamonds for 6.

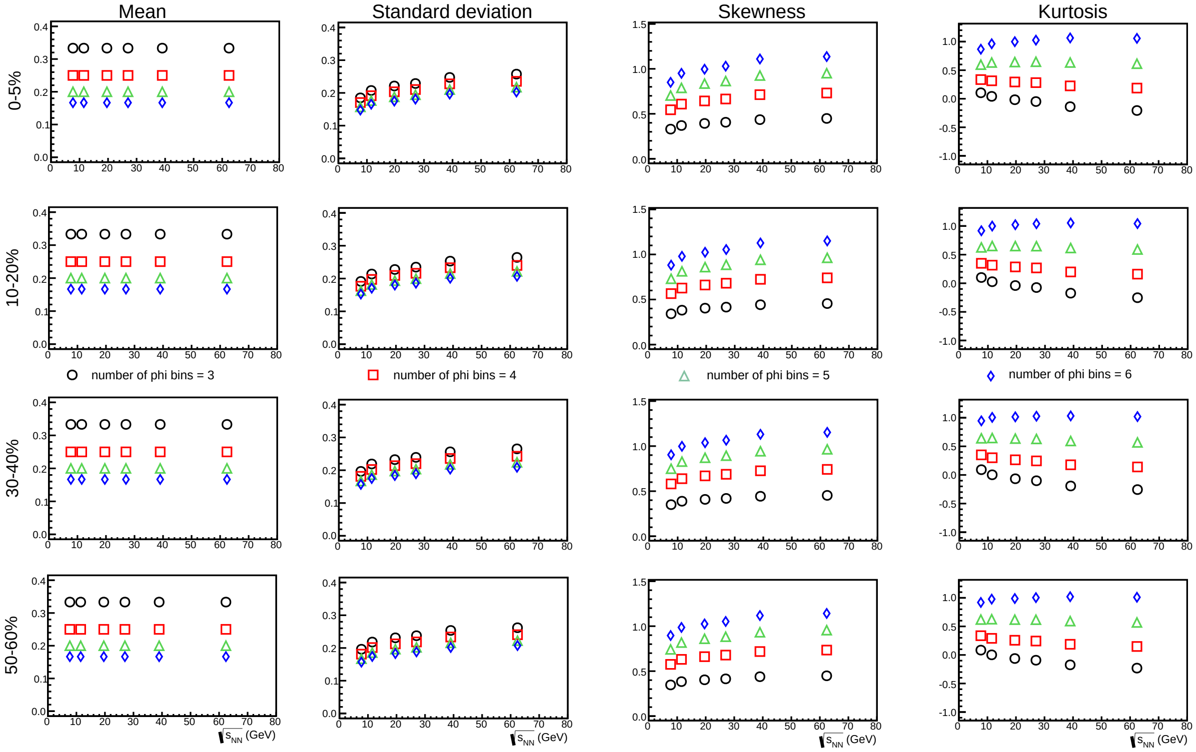

Figure 3.14: (Color online) Event-by-event distribution of the ratio of protons in one azimuthal region to the total number of protons in the event for mixed events sample Au+Au collisions as a function of collision energies for different centralities. The number of azimuthal divisions are varied from 3 to 6.

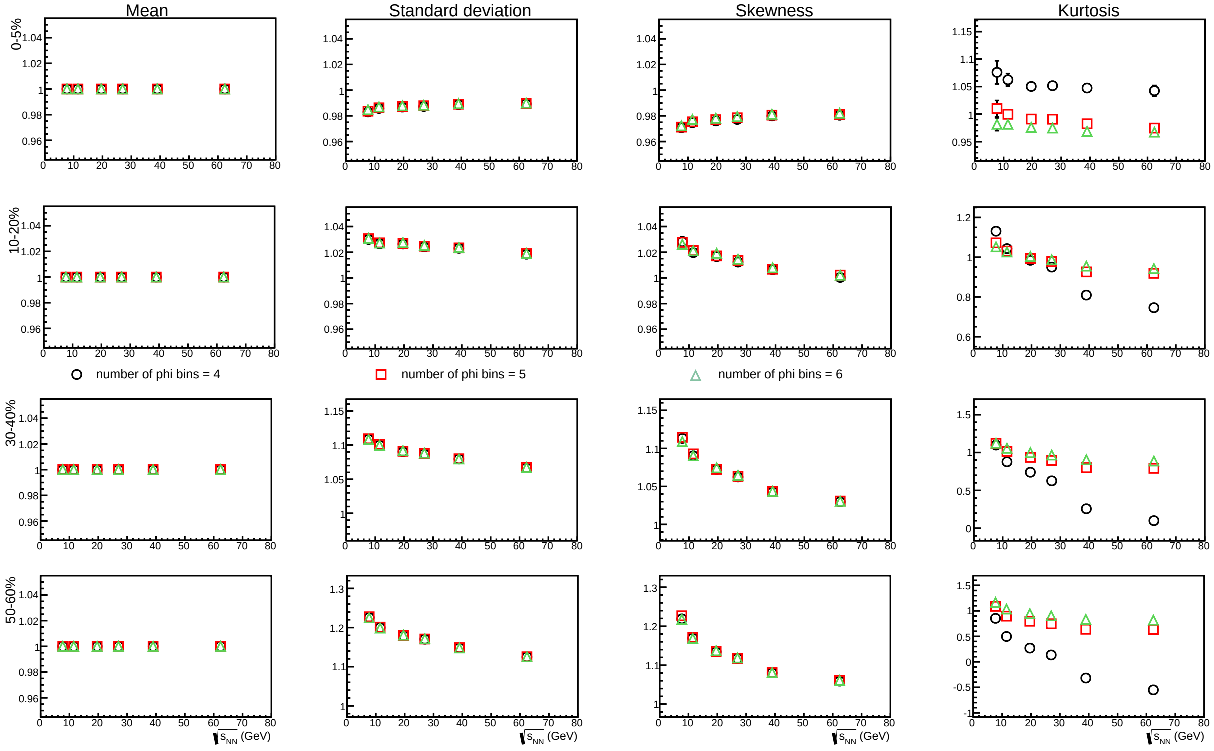

Figure 3.15: (Color online) The ratio of cumulants from data to those from mixed events for the event-by-event distribution of the ratio of protons in one azimuthal region to the total number of protons in the event for Au+Au collisions as a function of collision energies for different centralities. The number of azimuthal divisions are varied from 4 to 6.

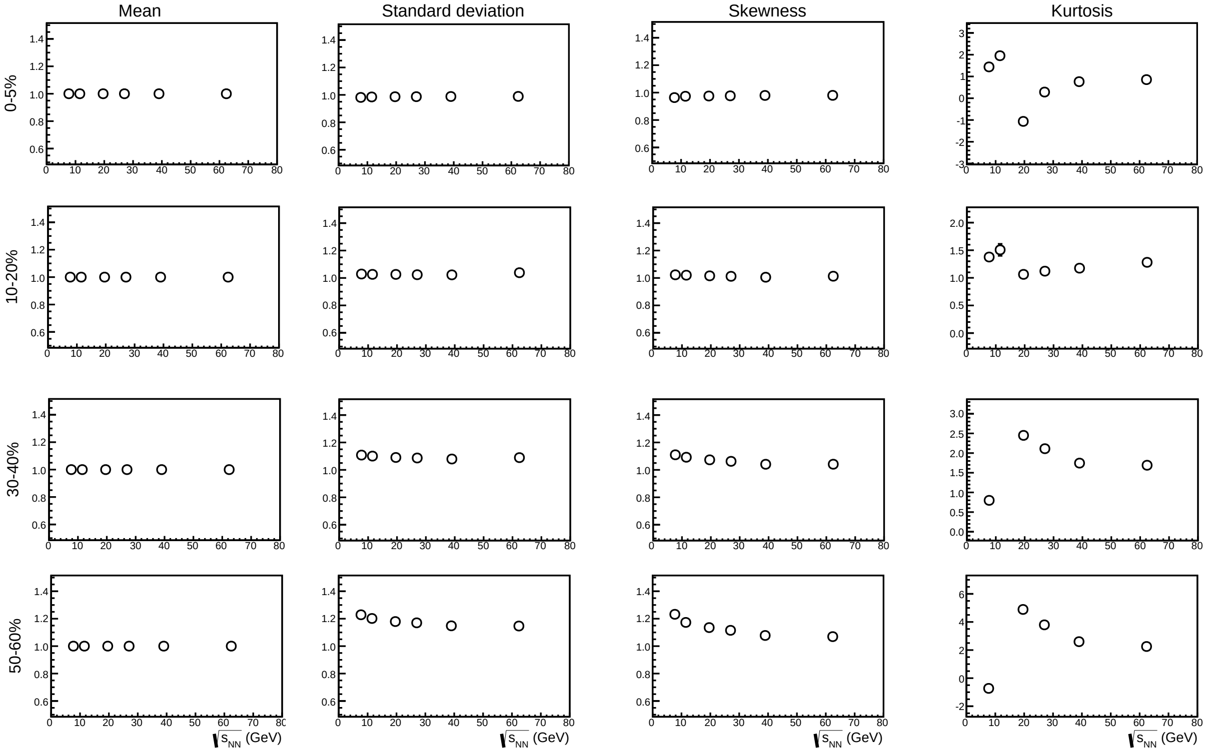

Figure 3.16: (Color online) The ratio of cumulants from data to those from mixed events for the event-by-event distribution of the ratio of protons in one azimuthal region to the total number of protons in the event for Au+Au collisions as a function of collision energies for different centralities. The number of azimuthal divisions is 3.

CHAPTER 4

The sixth-cumulant of net-proton multiplicity distribution

4.1 Introduction

Fluctuations and correlations have been considered as sensitive observables to explore the bulk properties of QCD such as phase transition, QCD critical point and thermalization of the matter created in high-energy heavy-ion collisions as they have a well-defined physical interpretation for a system in thermal equilibrium and can provide essential information about the effective degrees of freedom. The magnitude of fluctuations in conserved quantities (baryon number, strangeness, and charge of the system) in a grand canonical ensemble at finite temperature are distinctly different in the hadronic and the QGP phases. Event-by-event fluctuation and correlation of the conserved quantities is one of the observables to study the properties of the QCD medium created in relativistic heavy-ion collisions [42] [43] [44].

The equation of state in QCD is given by

$$\frac{P}{T^4} = \sum_{i,j,k=0}^{\infty} \frac{1}{i!j!k!} \chi_{i,j,k}^{BQS}(T) \left(\frac{\mu_B}{T}\right)^i \left(\frac{\mu_Q}{T}\right)^j \left(\frac{\mu_S}{T}\right)^k \tag{4.1}$$

where T is the temperature and P is the pressure. BQS stands for the conserved charges, which are baryon number, charge and strangeness, associated with their corresponding chemical potential (μ). The susceptibility (χ), which is defined as the derivative of free energy density or pressure of a thermodynamic system at a given temperature with respect to the chemical potential, can be related to the cumulants of the event-by-event distribution of the associated conserved quantity in the following way

$$\chi_q^{(n)} = \frac{\partial^n (P/T^4)}{\partial(\mu_q/T)^n} = \frac{1}{VT^3} \times C_{n,q}, \tag{4.2}$$

where V is the volume and q denotes the conserved quantity, that is, charge, baryon number or strangeness. The ratios of such cumulants as experimental observables cancel the volume and temperature dependence and can be directly compared to the ratios of susceptibilities from theoretical calculations.

Lattice QCD is a well-established non-perturbative approach to solve the theory of quarks and gluons exactly from first principles, without any assumptions. It can be used to study the thermodynamic properties of a strongly interacting system in thermal equilibrium. Most importantly, Lattice QCD provides a framework for investigation of non-perturbative phenomena which are difficult to deal by means of analytic field theories. However, these calculations can be performed exactly at zero chemical potentials only [22] [23]. To explore phenomenon at finite baryon chemical potentials, next to leading order calculations are performed using the current best approach, which is Taylor expansion about $\mu_B = 0$ [80].

$$\frac{p(T,\mu_B) - p(T,0)}{T^4} = \frac{1}{2}\chi_2(T)\left(\frac{\mu_B}{T}\right)^2 \times \left[1 + \frac{1}{4}\frac{\chi_4(T)}{\chi_2(T)}\left(\frac{\mu_B}{T}\right)^2 + \frac{1}{360}\frac{\chi_6(T)}{\chi_2(T)}\left(\frac{\mu_B}{T}\right)^4\right] + O(\mu_B^8) \tag{4.3}$$

The correction to current measurements is estimated to be $\sim \frac{1}{720}\frac{\chi_6(T)}{\chi_2(T)}\left(\frac{\mu_B}{T}\right)^6$.

Constrained by statistics, up to fourth-order cumulants has been experimentally determined at the STAR experiment [46]. These results differ from Lattice calculations and Hadron Resonance Gas results considerably for higher collision energy or smaller baryon chemical potential [80]. It is expected from Lattice calculations that the sixth order cumulant of baryon number remain negative at the chiral transition temperature which is strikingly different from Hadron Resonance Gas model, which predicts it to be positive [81]. In addition, the determination of the ratio of the sixth-order cumulant to the second-order cumulant will provide a characteristic signature for the location of the freeze-out temperature relative to the QCD phase transition temperature.

4.2 Analysis technique

We apply the following techniques to allow for precise event-by-event fluctuation measurements and background suppression:

1. **Centrality determination**: The definition of collision centrality is not unique. It is usually determined by comparing experimentally measured particle multiplicity with Monte-Carlo Glauber simulations. In order to suppress auto-correlations, which is a background effect and can reduce the magnitude of the signal in fluctuation analyses, we exclude the corresponding protons and anti-protons from the centrality definition [82].

2. **Centrality Bin Width Correction**: The centrality bin width effect is caused by variation of volume within a wide centrality range. This results in an artificial centrality dependence for the fluctuation observable. In order to suppress volume fluctuations over wide centrality bins, the cumulants are weighted and then averaged to get the value for the given centrality [83].

3. **Statistical error estimation**: Statistical errors on the cumulant of order r (C_r) depend on the number of events (N) and the width of the distribution (σ) as :

   $$Error\ (C_r) \propto \frac{\sigma^r}{\sqrt{N}}. \tag{4.4}$$

   These are estimated either by the Bootstrap technique [84], which is based on the method of resampling, or using the Delta Theorem [85], which is an analytical technique. We find that these methods give similar results.

4. **Detection efficiency correction**: The observed event-by-event particle multiplicity distribution is a convolution of the original distribution and the efficiency response function. Efficiency correction includes the net effect of tracking efficiency, detector acceptance, decays and interaction losses. In order to correct the cumulants for efficiency, the principal idea is to express them in terms of the factorial moments [85] [86]

or factorial cumulants [87], which can be efficiency corrected assuming a Binomial response function.

The cumulants of net-proton multiplicity distribution, which is the event-by-event difference of the number of protons and anti-protons, are measured in this report. The efficiency-corrected cumulants will be obtained using bivariate factorial moments assuming Binomial efficiency for protons and anti-protons and the statistical errors will be estimated using Delta theorem.

The factorial moments (f_{ij}) are defined as

$$f_{ij}(n_p, n_{\bar{p}}) = \left\langle \frac{n_p!}{(n_p - i)!} \frac{n_{\bar{p}}!}{(n_{\bar{p}} - j)!} \right\rangle, \tag{4.5}$$

where n_p and $n_{\bar{p}}$ are the measured number of protons and anti-protons in every event respectively. The efficiency-corrected factorial moments (F_{ij}) are given by

$$F_{ij}(N_p, N_{\bar{p}}) = \frac{f_{ij}(n_p, n_{\bar{p}})}{\varepsilon_p^i \varepsilon_{\bar{p}}^j}, \tag{4.6}$$

where N_p and $N_{\bar{p}}$ are the true number of protons and anti-protons in every event and ε_p and $\varepsilon_{\bar{p}}$ are the efficiencies of protons and anti-protons respectively. The n-th order moments (μ_n) can then be expressed as

$$\mu_n(N_p - N_{\bar{p}}) = \sum_{i=0}^{n} \sum_{r_1=0}^{n-i} \sum_{r_2=0}^{i} (-1)^i \binom{n}{i} s_2(n-i, r_1) s_2(i, r_2) F_{r_1, r_2}(N_p, N_{\bar{p}}), \tag{4.7}$$

where $s_2(n, i)$ is the Sterling number of second kind[1]. Finally, the efficiency-corrected cumulants (C_n) of are obtained from the efficiency-corrected moments (μ_n) using the following recursion relation:

$$C_n(N_p - N_{\bar{p}}) = \mu_n(N_p - N_{\bar{p}}) - \sum_{s=1}^{n-1} \binom{n-1}{s-1} C_s(N_p - N_{\bar{p}}) \mu_{n-s}(N_p - N_{\bar{p}}) \tag{4.8}$$

The ratio of the sixth-order to the second order cumulant is defined as

---

[1] $s_2(n, i) = s_2(n-1, i-1) + i \times s_2(n-1, i)$ with $s_2(n, i)|_{n<i} = 0$, $s_2(n, i)|_{n=i} = 1$, $s_2(n, 0)|_{n>0} = 0$

$$\begin{aligned}\frac{C_6}{C_2} = \frac{1}{\mu_2 - \mu_1^2}\Bigg(&\mu_6 - 6\mu_5\mu_1 - 15\mu_4\mu 2 + 30\mu_4\mu_1^2 - \\ &10\mu_3^2 + 120\mu_3\mu_2\mu_1 - 120\mu_3\mu_1^3 + \\ &30\mu_2^3 - 270\mu_2^2\mu_1^2 + 360\mu_2\mu_1^4 - 120\mu_1^6\Bigg)\end{aligned} \tag{4.9}$$

in terms of other cumulants. The statistical error, based on Delta theorem, can be estimated as

$$\begin{aligned}\delta\left(\frac{C_6}{C_2}\right)^2 = \frac{\sigma^8}{N}\Bigg(&m_{12} + 10575 - 30m_{10} + 18300m_3^2 + 2600m_3^4 - \\ &225(-3+m_4)^2 - 7440m_3m_5 - 520m_3^3m_5 - \\ &2160m_6 - 200m_5^2m_6 + 52m_3m_5m_6 + 33m_6^2 + \\ &(-3+m_4)\left[10\left(405 - 390m_3^2 + 10m_3^4 + 24m_3m_5\right) - 20m_6\left(6 + m_3^2\right) + m_6^2\right] + \\ &840m_3m_7 - 12m_5m_7 + 345m_8 + 20m_3^2m_8 - 40m_3m_9\Bigg)\end{aligned} \tag{4.10}$$

where $m_r = \mu_r/\sigma^r$. μ is the mean of the N entries and σ is its standard deviation.

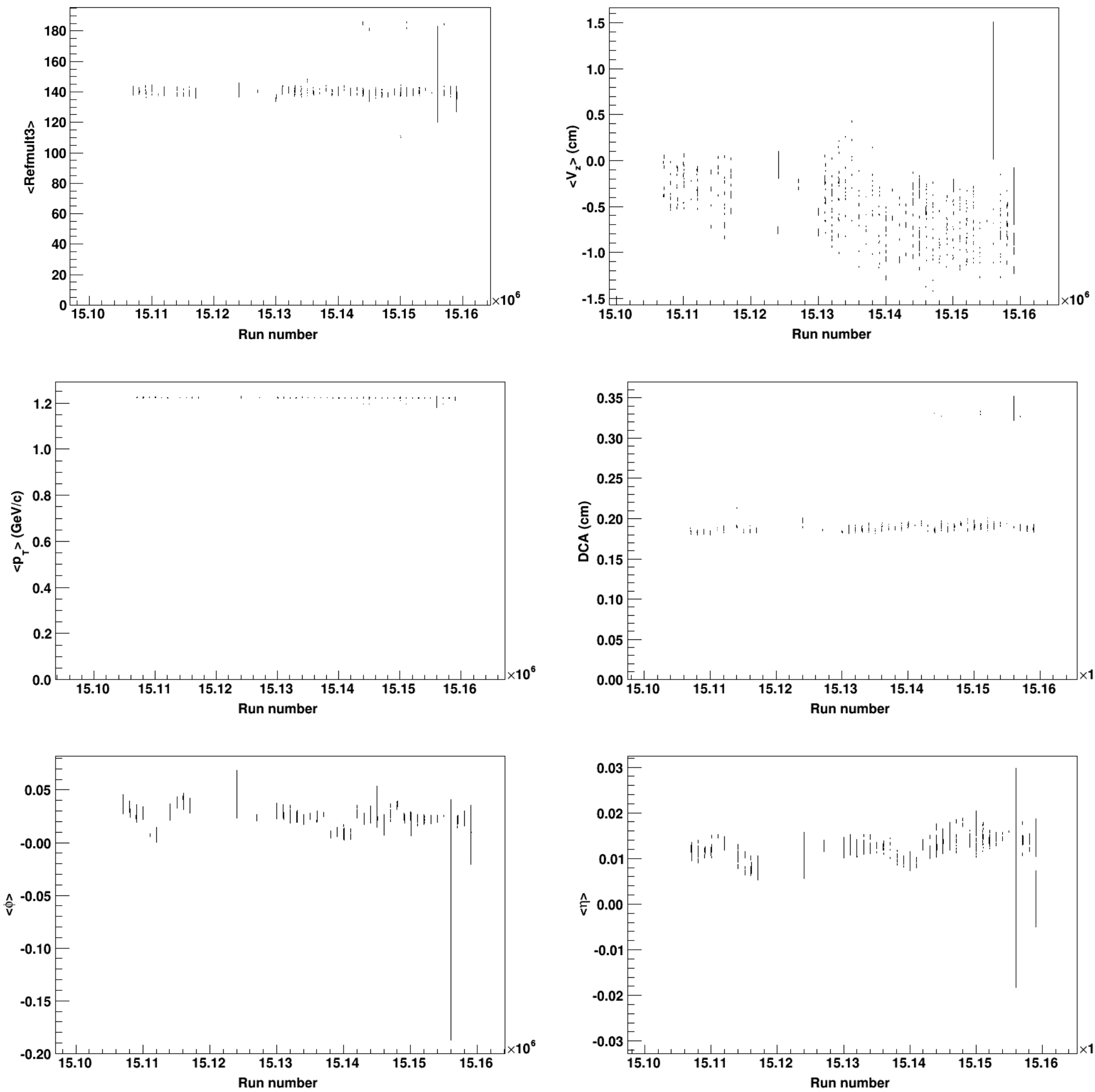

Figure 4.1: Distribution of mean reference multiplicity (refmult3), mean Z-vertex position (V_z), mean transverse momentum (p_T), mean distance of closest approach (DCA), mean azimuthal angle (ϕ) and mean pseudorapidity (η) with run number

4.3 Data Analysis

The large statistics data taken by the STAR experiment in the year 2014 for Au+Au collisions at $\sqrt{s_{NN}} = 200$ GeV by the STAR experiment are analyzed.

4.3.1 Data sets

A series of selection procedures are implemented to ensure high quality data is used for analysis.

4.3.1.1 Triggers

In the year 2014, around 1.4 billion events are collected at STAR for Au+Au collisions at $\sqrt{s_{NN}} = 200$ GeV over a period of 4 months. Of these, around 900 million were minimum bias events, which are given by coincidence between the Vertex Position Detector and the Zero Degree Calorimeter. For this dataset, minimum bias events are identified from the st-physics and st-physics-adc streams by the triggers 450050 and 450060.

4.3.1.2 Run selection

At STAR, data is collected for periods of half an hour at a stretch, called a run, and constitute an average of 2 million events. For the year 2014, around 13, 600 runs were recorded for Au+Au collisions at $\sqrt{s_{NN}} = 200$ GeV. Apart from the runs marked bad by the crew, the ones with either of mean reference multiplicity, mean Z-vertex position, mean transverse momentum, mean distance of closest approach, mean azimuthal angle, or mean pseudorapidity more than 3 standard deviation away from the average over the entire period are also removed from analysis. The quality assurance plots are given in Figure 4.1. List of bad runs is given in Appendix A.

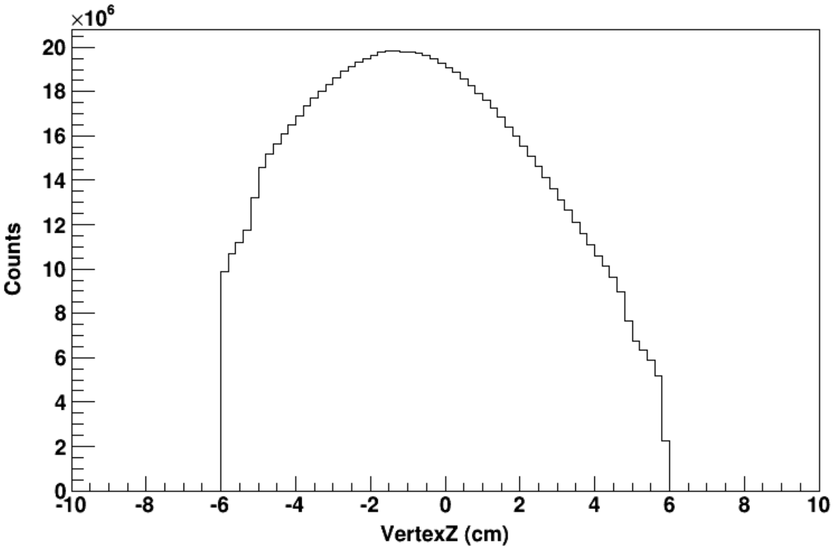

Figure 4.2: Event-by-event distribution of the Z-vertex position of the reconstructed tracks.

4.3.1.3 Event selection

Event selection cuts are applied on the primary vertex position. It is required that the Z-vertex position reconstructed based on tracks from Time Projection Chamber is within 5 cm of the center of the STAR detector. The event-by-event distribution of the Z-vertex position of the selected tracks is shown in Figure 4.2. Also, the radial distance of the primary vertex is within 2 cm of the beam axis. The absolute difference between the vertices reconstructed from the Vertex Position Detector and the Time Projection Chamber should lie within 3 cm. In order to reduce contributions from pile-up, every event is required to have at least two tracks within pseudorapidity of ±0.5 with Time of Flight information and at least one track within pseudorapidity of ±1.0 has $\beta > 0.1$.

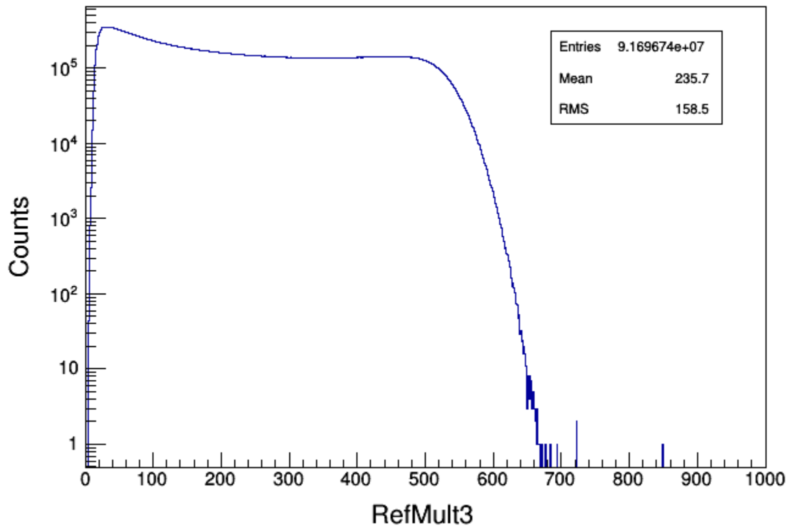

Figure 4.3: (Color online) Event-by-event distribution of the raw charged particle multiplicity.

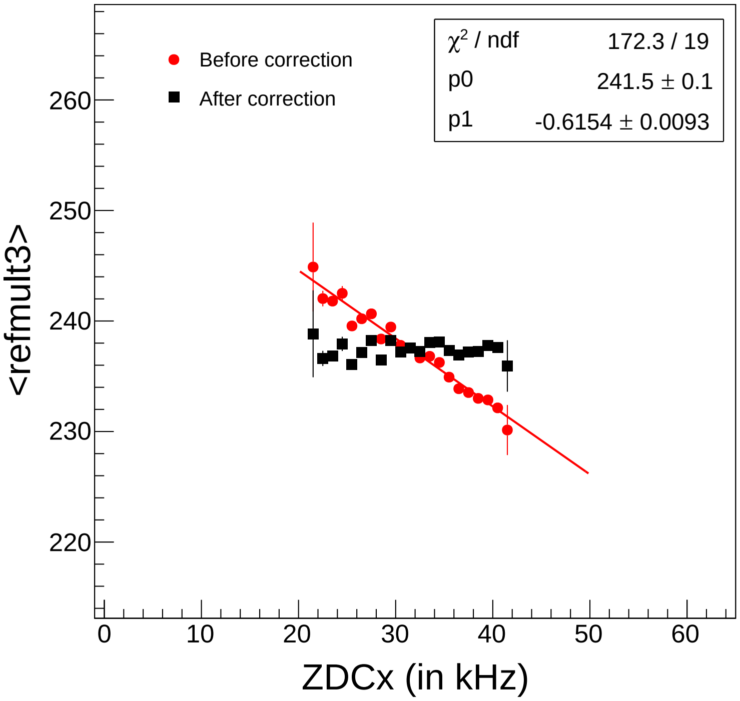

Figure 4.4: (Color online) The RefMult3 distribution as a function of ZDC coincidence rate before and after luminosity correction.

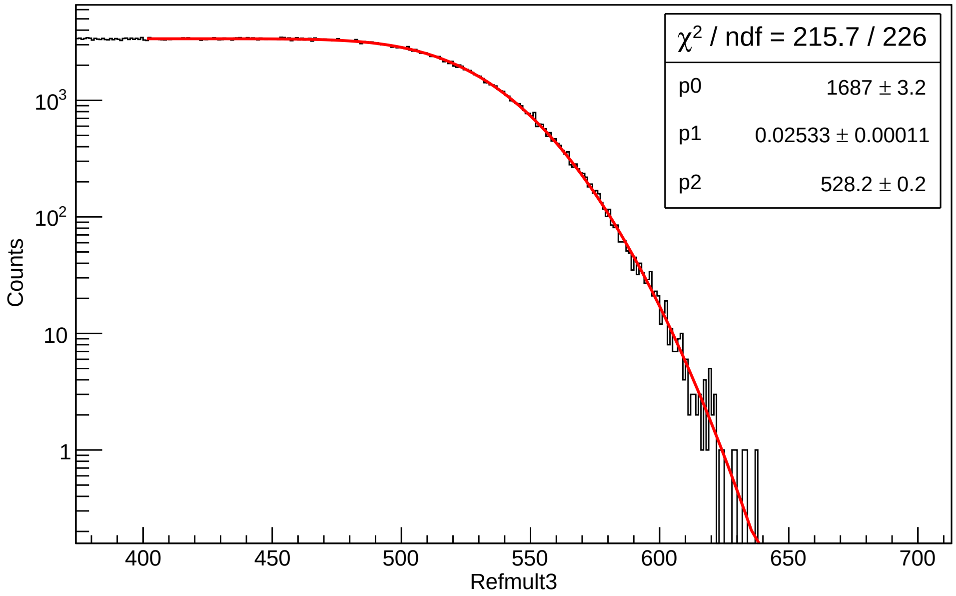

Figure 4.5: (Color online) A sample fit of the tail of the RefMult3 distribution with Gaussian Error fit function to obtain parameter H (same as $p2$ in the plot) for $-1 < V_z < 1$ cm..

4.3.2 Centrality determination

Primary tracks are used for determination of event centrality. Track selection criteria ensure properly reconstructed tracks are used for centrality determination. The distance of closest approach from the primary vertex is required to be less than 3 cm. There should be a minimum of 10 hits in the Time Projection Chamber. The minimum transverse momentum for track reconstruction is 0.15 GeV/c. In order to reduce the effect of auto-correlation, protons and anti-protons are removed. The reconstructed mass from the Time of Flight, if available, is less that 0.4 GeV/c^2 and $n\sigma_{proton} < -3.0$. The total number of tracks satisfying the above criteria in an event is called RefMult3. Raw RefMult3 distribution is shown in Figure 4.3. The RefMult3 distribution, thus obtained, is corrected for luminosity and Z-vertex dependence. For luminosity correction, the fit function used is $p0+p1(x-25)$, where $p0$ and $p1$ are the fit parameters. The correction factor, hence obtained, is $1/[1+(p1/p0)(x-25)]$. The RefMult3 distribution as a function of ZDC coincidence rate before and after correction is shown in Figure 4.4. For the Z-vertex correction, the parameter H (which is the same as parameter $p2$ in the Figure 4.5) is obtained by fitting the tail of the RefMult3 distribution with the Gaussian Error fit function

$$y = p0 + p1 * Erf(-\sigma(x - H)) \tag{4.11}$$

as shown in Figure 4.5 for $-1 < V_z < 1$ cm. Similar fits were performed for different intervals of Z-vertex. The values of the parameter H, before and after correction is shown in Figure 4.6. Sixth-order polynomial is used to get the correction factor.

The corrected RefMult3 distribution thus obtained is compared with Glauber Monte-Carlo calculations, as shown in Figure 4.7 to obtain the centrality definition. Re-weighting is required for peripheral collisions.

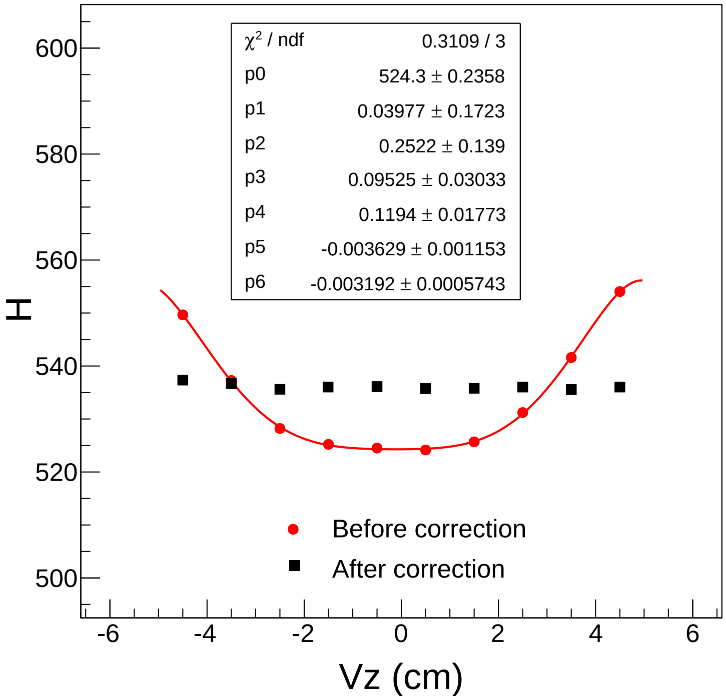

Figure 4.6: (Color online) The value of the parameter H before and after V_z correction for different Z-vertex intervals.

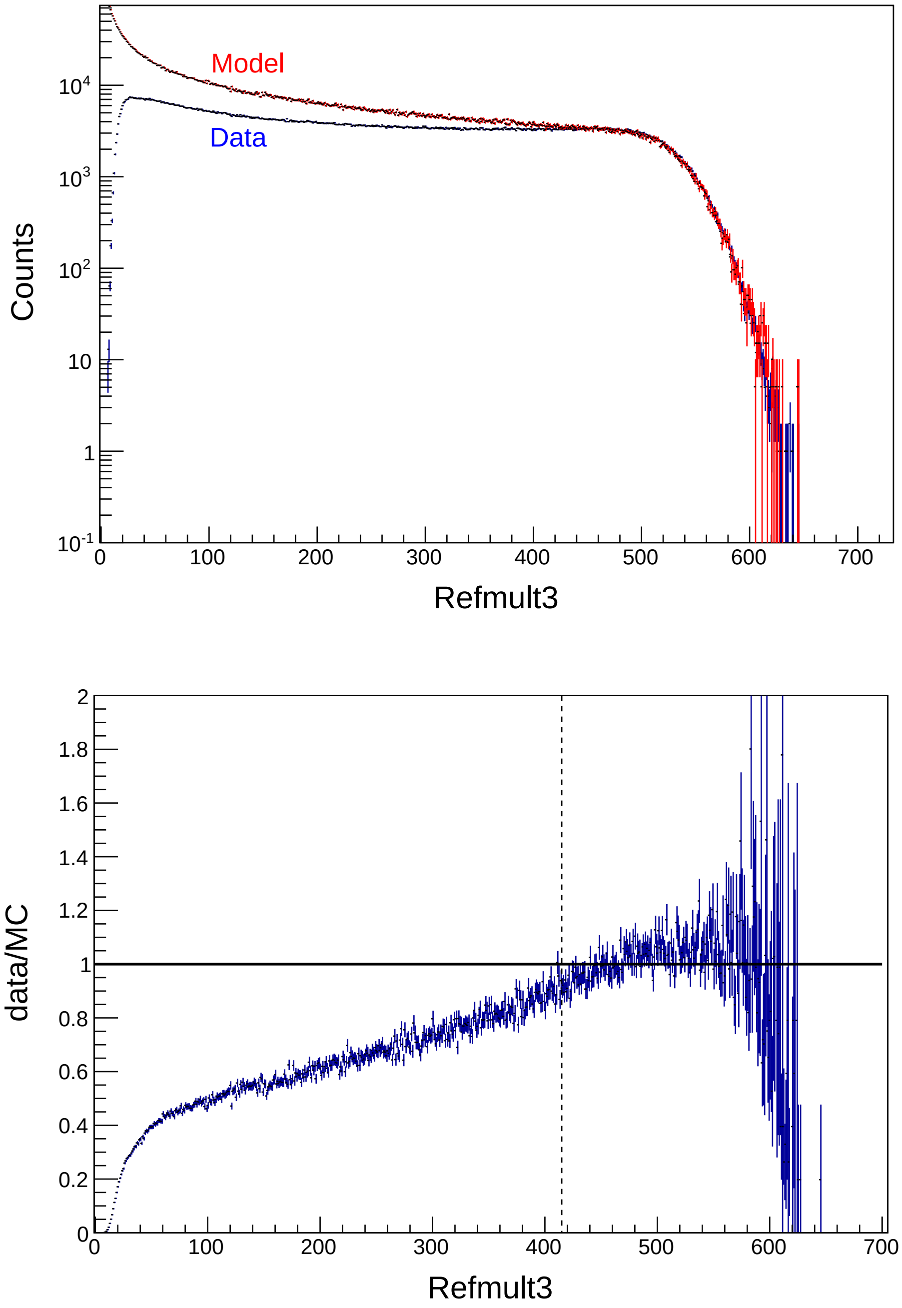

Figure 4.7: Comparison of corrected RefMult3 distribution with Glauber Monte Carlo calculations to get the centrality definition.

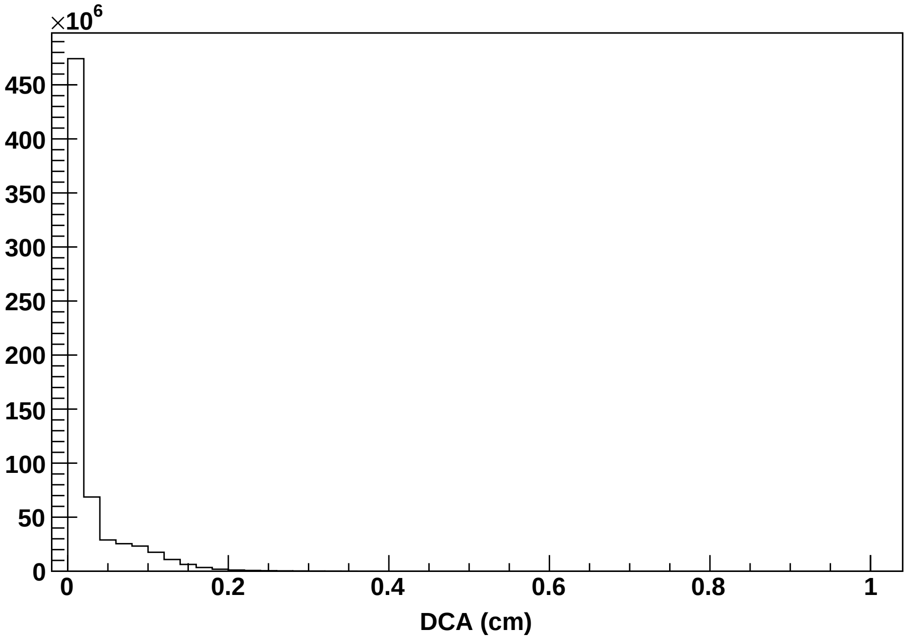

Figure 4.8: Distribution of the distance-of-closest approach (DCA) of the selected tracks.

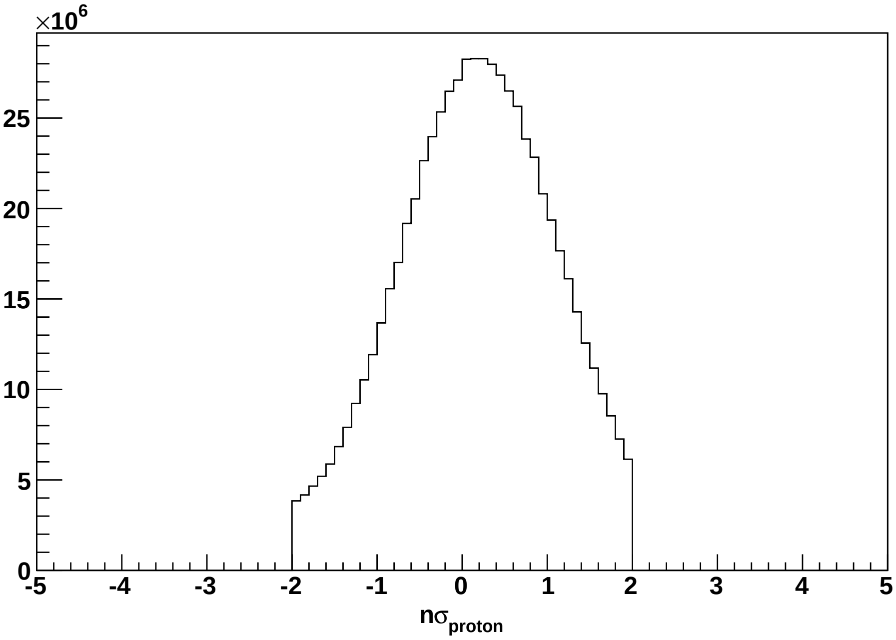

Figure 4.9: $n\sigma_{proton}$ distribution of the selected tracks.

4.3.2.1 (Anti-)Proton identification

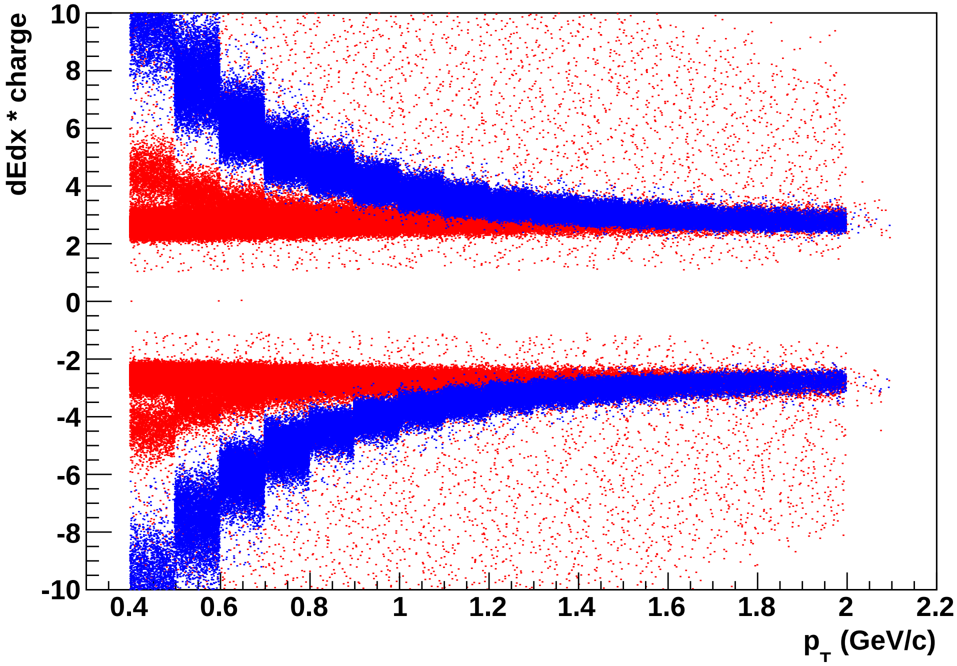

Figure 4.10: (Color online) Energy loss of reconstructed tracks as measured in the Time Projection Chamber. Blue tracks are the selected (anti-)proton tracks.

Primary tracks are used for the identification of proton and anti-protons. The ratio of number of hits used for track reconstruction to the maximum number of hits possibles should lie between 0.52 and 1.02. Atleast 20 hits are used for track reconstruction. It is ensured that a minimum of 5 hits are used in track energy loss calculation. The distance-of-closest approach from the primary vertex is less than 1 cm as shown in Figure 4.8. The rapidity of the track is within ±0.5. The $n\sigma_{proton}$ is required to be less than 2.0. The $n\sigma_{proton}$ distribution of the selected tracks is shown in Figure 4.9. For the low transverse momentum regime, that is, transverse momentum between 0.4 to 0.8 GeV/c, track energy loss as measured in the Time Projection Chamber is used to identify (anti-)protons. The selected tracks are shown in Figure 4.10. The reconstructed mass from the Time of Flight, for transverse momentum between 0.8 to 2.0 GeV/c, should lie between 0.8 and 1.0 GeV/c^2. The selected tracks are shown in Figure 4.11.

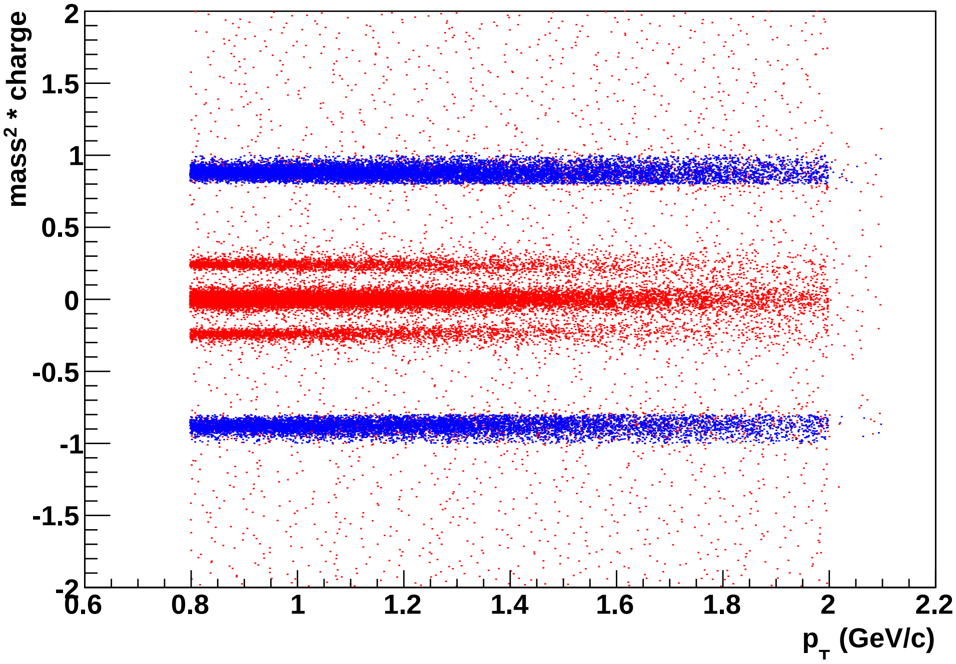

Figure 4.11: (Color online) Mass of reconstructed tracks as measured in the Time of Flight detector. Blue tracks are the selected (anti-)proton tracks.

4.4 Results and discussions

Figure 4.12 shows the measured net-proton multiplicity distribution for the Au+Au collision data at $\sqrt{s_{NN}} = 200$ GeV taken in the year 2014.

In order to account for detector inefficiencies, information from embedding is used to obtain the efficiency of protons and anti-protons. In embedding, Monte-Carlo tracks are embedded in real event and passed through the entire reconstruction framework. Comparing the input Monte-Carlo tracks to those reconstructed, imposing the same selection criteria as that in real data, would give us an estimate of the particle detection efficiencies. The embedding framework at STAR includes correction for the track reconstruction in the Time Projection Chamber. In the year 2014, the Heavy Flavor Tracker detector subsystem was introduced inside the Time Projection Chamber. In order to account for the losses in the Heavy Flavor Tracker, the technique of DCA-smearing is used. The distance-of-closest approach is then evaluated for the reconstructed track using the StDcaGeometry class. Figure 4.13

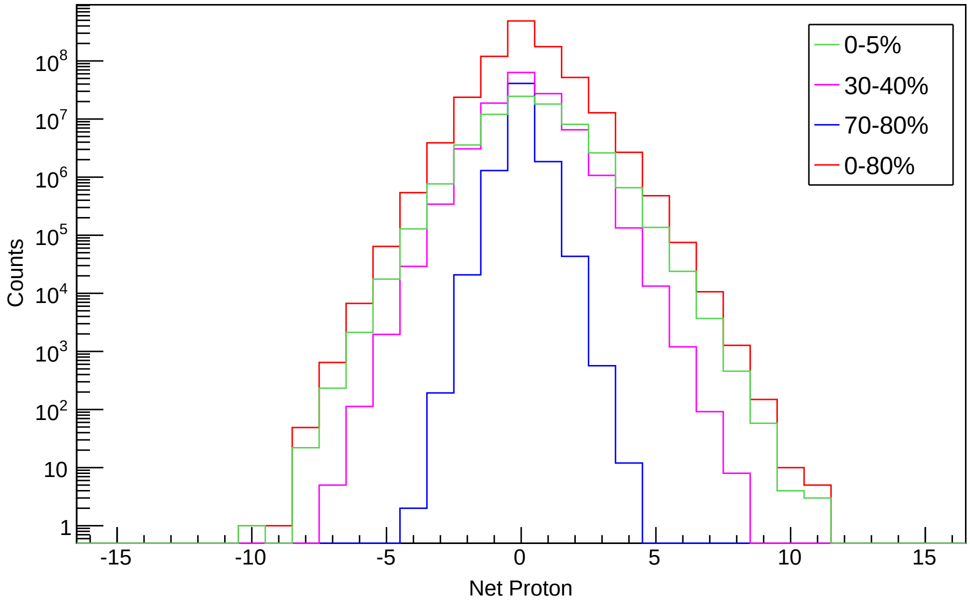

Figure 4.12: (Color online) Measured net-proton multiplicity distribution for the Au+Au collision at $\sqrt{s_{NN}} = 200$ GeV.

and Figure 4.14 shows the detection efficiency of protons and anti-protons respectively for different collision centralities. The p_T-integrated efficiency as a function of RefMult3 is given in Figure 4.15.

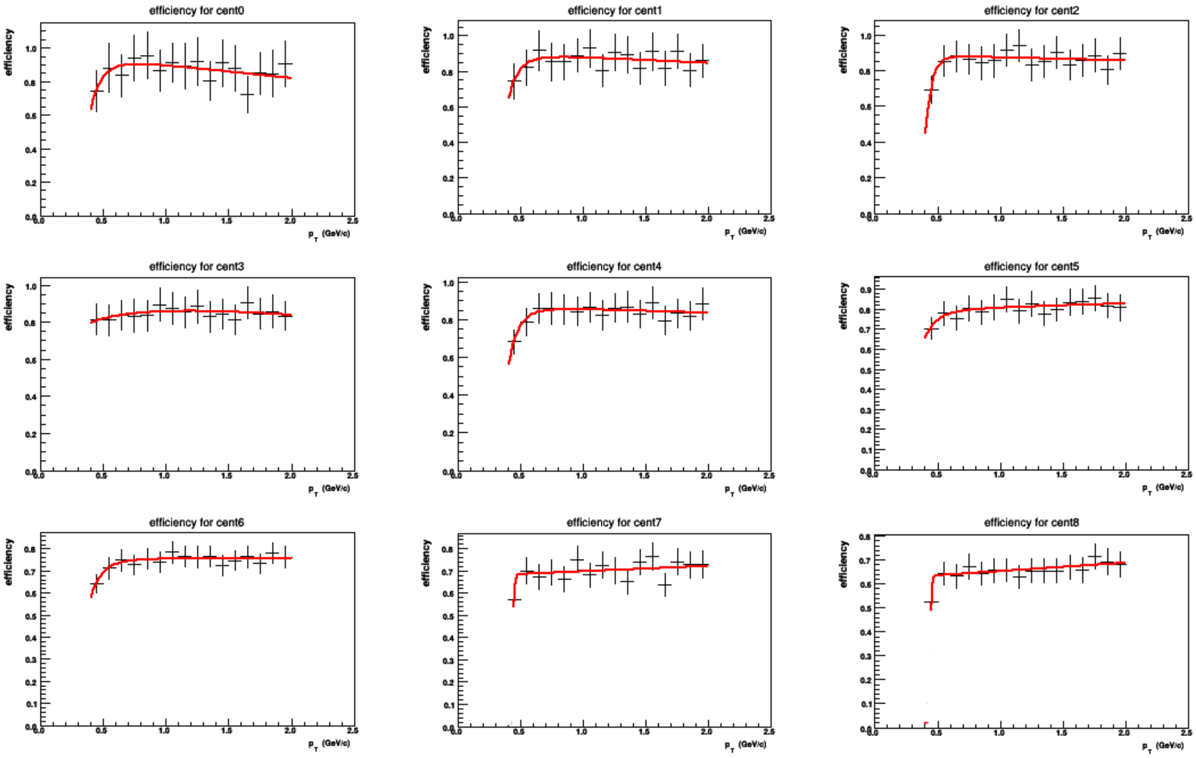

Figure 4.13: (Color online) Reconstruction efficiency of protons for different centralities as a function of transverse momentum.

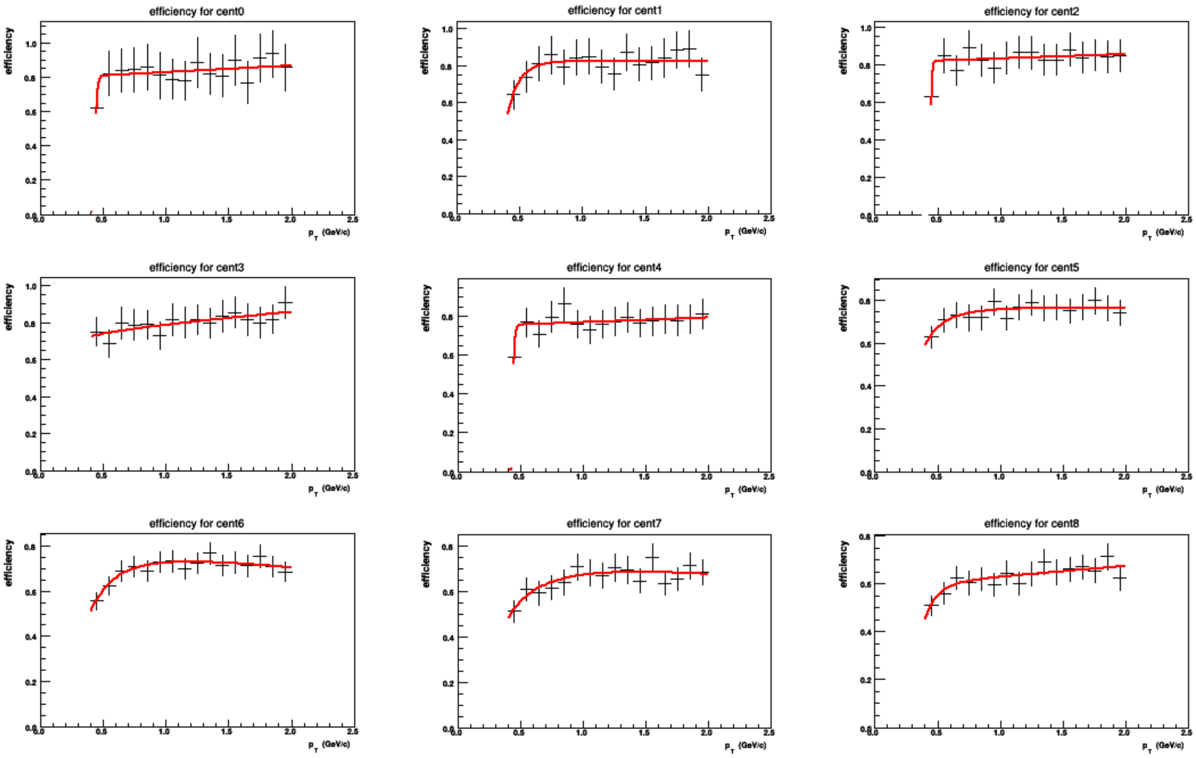

Figure 4.14: (Color online) Reconstruction efficiency of anti-protons for different centralities as a function of transverse momentum.

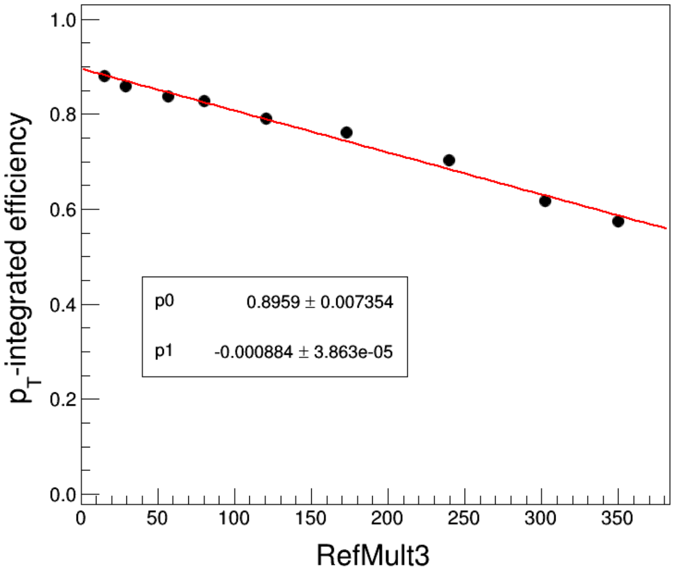

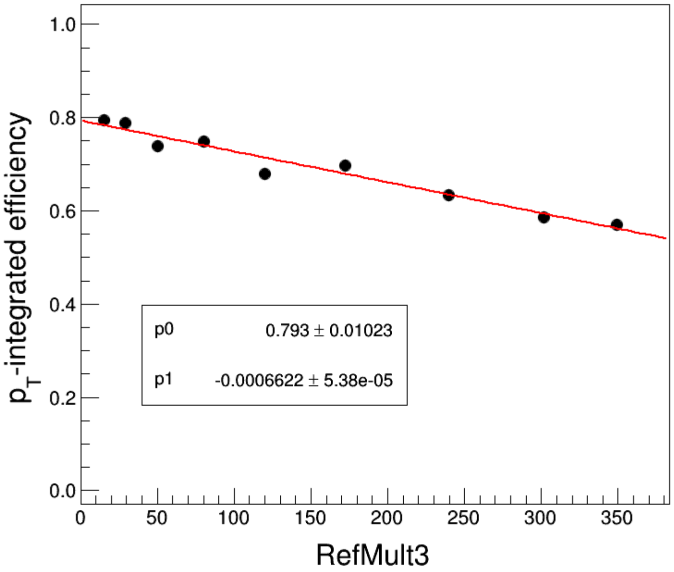

Figure 4.15: (Color online) p_T-integrated reconstruction efficiency of protons (top) and anti-protons (bottom) as a function of charged particle multiplicity. The linear fit function is used to correct the cumulants for each reference multiplicity.

With the ingredients in place, the efficiency-corrected sixth-order cumulant and the ratio of sixth-order to the second-order cumulant of the net-proton multiplicity distribution for Au+Au collisions at $\sqrt{s_{NN}}$ = 200 GeV is measured using the data from the year 2014 and shown in Figure 4.16. The measurements are done for (anti-)protons within $|y| < 0.5$ and $0.4 < p_T < 0.8$ GeV/c. We find that the sixth-order cumulant is systematically negative for central collisions. In all, around 750 million good events were analyzed for 0-80% central collisions.

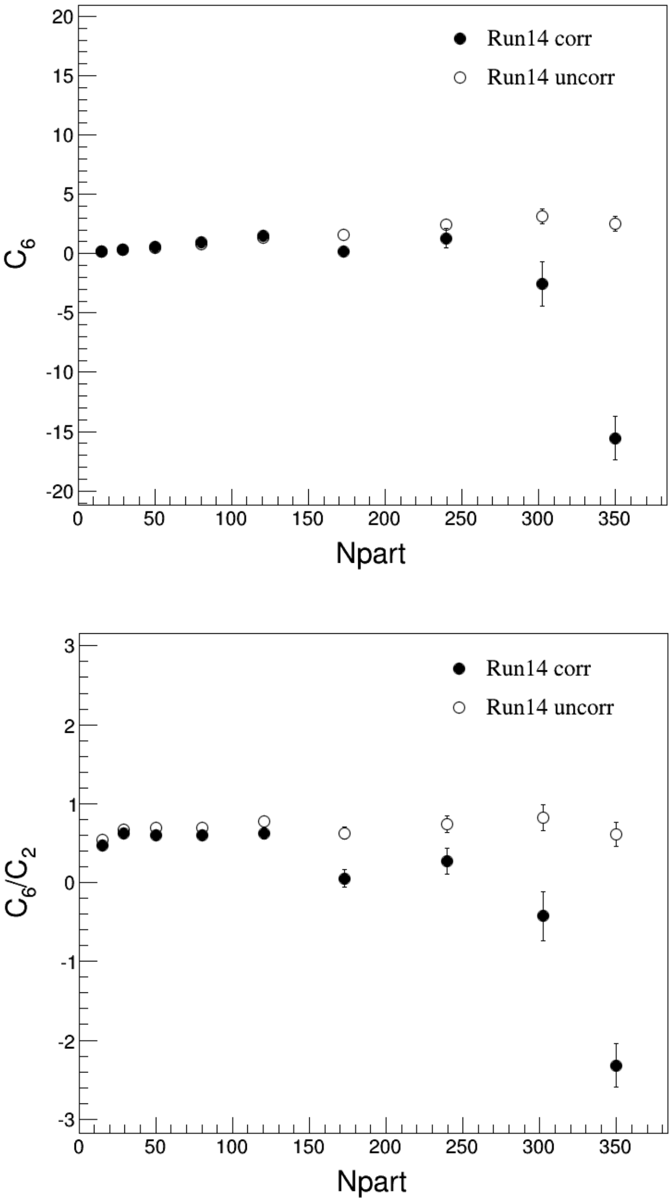

Figure 4.16: Sixth-order cumulant and the ratio of sixth-order to the second-order cumulant of the net-proton multiplicity distribution for Au+Au collisions at $\sqrt{s_{NN}} = 200$ GeV within $|y| < 0.5$ and $0.4 < p_T < 0.8$ GeV/c.

4.4.1 Comparison to Lattice QCD

The ratio of the sixth-order cumulant to the second-order cumulant for net-proton multiplicity distribution for Au+Au collision at $\sqrt{s_{NN}} = 200$ GeV is compared with calculations of the ratio of sixth-order to the second-order baryon susceptibility from Lattice QCD in Figure 4.17. The left panel is the measurement from data, while the right panel is the calculations from Lattice QCD [41].

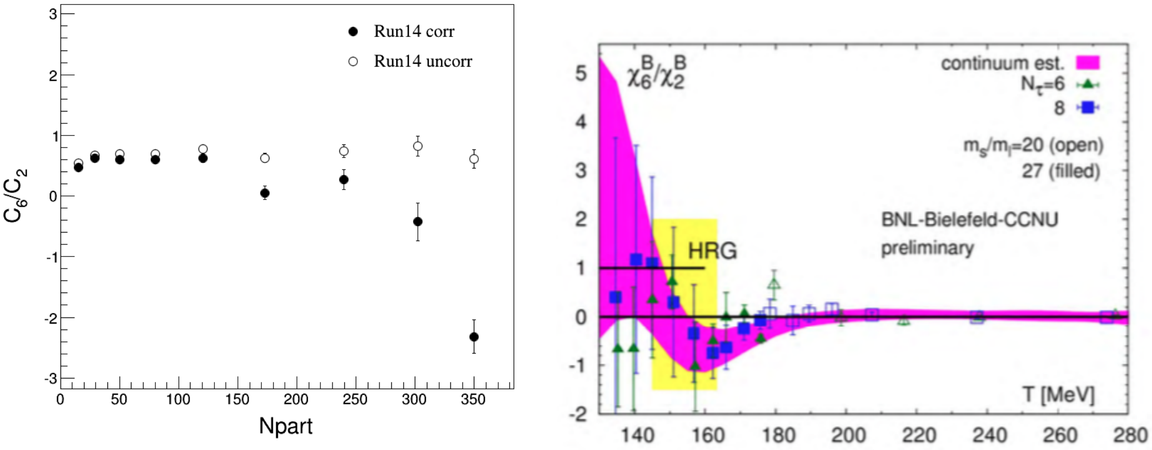

Figure 4.17: (Color online) Comparison between calculations from Lattice QCD and experimental data.

However, there are a few caveats that needs to be noted when comparing Lattice QCD calculations with experimental measurements. Lattice QCD calculations are performed for net-baryons over the entire phase space. In experimental measurements, net-protons are used as a proxy for net-baryons. In addition, the analysis is performed over the phase space restricted by detector characteristics in transverse momentum and rapidity. Lattice QCD calculations are exact for $\mu_B = 0$ and Taylor expansion is used for larger baryon chemical potentials. In Au+Au collisions at $\sqrt{s_{NN}} = 200$ GeV, $\mu_B \sim 20$ MeV.

Considering these, cautious comparisons can be made between 0-5% central Au+Au collisions at $\sqrt{s_{NN}} = 200$ GeV with Lattice QCD calculations around $T \sim 160$ MeV. We find the cumulant (susceptibility) ratio to be negative, within large statistical uncertainties.

4.5 Conclusion

Using a Binomial approximation to efficiency estimation, the results for the sixth-order cumulant and the ratio of sixth-order to the second-order cumulants for net-proton multiplicity distribution for Au+Au collisions at $\sqrt{s_{NN}} = 200$ GeV is discussed. We find the results to be negative for central collisions within large statistical uncertainties. We have also compared our results with estimates from Lattice QCD calculations.

However, recent studies have shown that even a slight deviation (at the level of 10^{-3}) of efficiency from Binomial approximation may lead to large deviations in the magnitudes of the cumulants. In the light of this, we proposed an unfolding approach to efficiency correction, which is discussed in detail in the next chapter.

CHAPTER 5

The unfolding approach to measurement of cumulants

5.1 Introduction

The measurement of higher-order cumulants is sensitive to experimental artifacts. Efficiency correction is one of the most important ingredients in order to reliably calculate the higher-order cumulants. The observed event-by-event particle multiplicity distribution is a convolution of the original distribution and the efficiency response function. Efficiency correction includes the net effect of tracking efficiency, detector acceptance, decays and interaction losses.

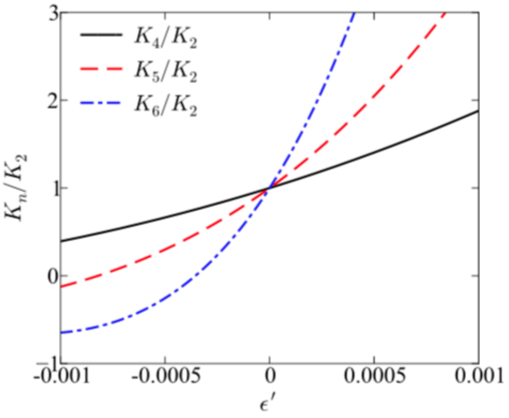

Figure 5.1: The ratio of n-th order cumulant to the second order cumulant (K_n/K_2) as a function of the slope of multiplicity-dependence of the efficiency.

Previous measurements of the cumulants of multiplicity distributions are based on the assumption that the efficiency response function follows a Binomial distribution [46] [47] [48]. However, recent studies show that there could be noticeable consequences of the multiplicity-dependent behavior of the detection efficiency on the measured higher-order cumulants [49]. Figure 5.1 shows the variation of the ratio of n-th order cumulant to the second order cumulant (K_n/K_2), n = 4, 5, 6 as a function of ε' when corrected using average, multiplicity independent, efficiency, ε_0, where in reality efficiency depends on the number of produced protons, $\varepsilon(N) = \varepsilon_0 + \varepsilon'(N - \langle N \rangle)$. In this calculation, $\varepsilon_0 = 0.65$ and $\langle N \rangle = 40$ [49]. The effect on higher-order cumulants is large.

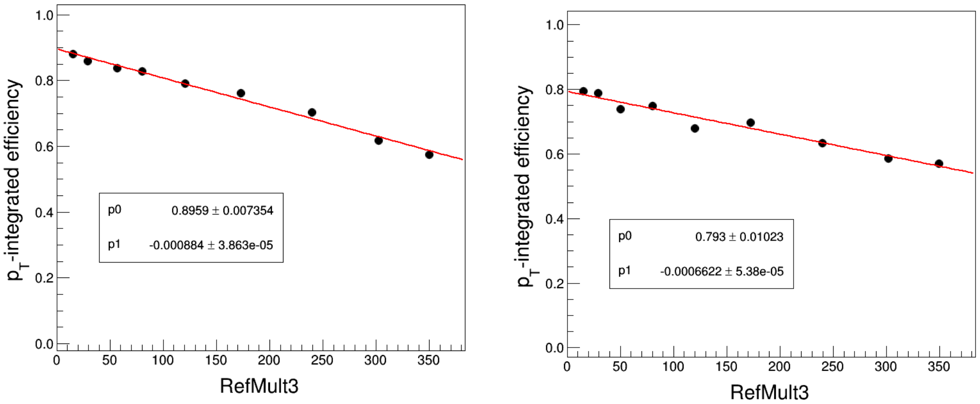

Figure 5.2: (Color online) p_T-integrated reconstruction efficiency of protons (left) and anti-protons (right) as a function of charged particle multiplicity. The linear fit function is used to correct the cumulants for each reference multiplicity.

Figure 5.2 shows the efficiency of protons (left) and anti-protons (right) integrated over transverse momentum as a function of charged particle multiplicity (excluding protons and anti-protons) in Au+Au collisions at $\sqrt{s_{NN}} = 200$ GeV. The measurements are for transverse momentum between 0.4 to 0.8 GeV/c and 1 unit in rapidity at mid-rapidity. We find that the detection efficiency decreases with particle multiplicity with the slope of the order of 10^{-3}.

In order to deal with such multiplicity-dependent efficiency, we have explored a data-driven approach to measure the cumulants of the distributions of physical variables. Comparing different methods would enable us to better understand the cumulants of these multiplicity distributions.

5.2 Methodology

The measured distribution is a convolution of the original produced particle distribution and the detector response function. The detector response function is used to extract the original produced particle distribution. The detector response function is obtained with embedding, where a few Monte Carlo tracks are embedded within a real experimental event and passed through the entire reconstruction chain. By studying the response of the reconstruction framework on these embedded Monte Carlo tracks, we can obtain the estimate of the detector response function.

The ingredients for the implementation of the data-driven technique are the correlation histogram and the response matrix. The correlation histogram contains the number correlation between the measured protons and anti-protons event-by-event. We can obtain the response matrix using the information from the embedded Monte Carlo tracks, which gives the distribution of the number of produced particles, for every given number of measured particles.

In order to obtain the cumulants of the multiplicity distributions, the event is sampled from the correlation histogram, that is, the number of measured protons and anti-protons in event is obtained. The number of protons and anti-protons is then corrected using the respective response matrices to get the produced number of protons and anti-protons in the event. This sampling is done for the total number of events in the true distribution. The above step is repeated M number of times. The cumulants are then evaluated for each of these M copies. The mean will be the value of the cumulant, while the width will be the corresponding uncertainty. Centrality bin width correction is not used in this approach.

5.3 Simulation results

For the simulations, 10 million events are used and 1000 copies are created to evaluate the cumulants and their respective errors. Three scenarios are analyzed using this data-driven method and the factorial moment method to understand the implications of various correction approaches towards a reliable measurement of the cumulants.

1. **Poisson distribution for protons and anti-protons with Binomial efficiency**

   We assumed that the event-by-event distribution of protons is given by a Poisson distribution with mean 10 and anti-protons with mean 9. The efficiency for protons and anti-protons is assumed to follow Binomial distribution with detection probability being 0.8 and 0.7 respectively. We compare the results in Table 5.1. We find that the results from both the data-driven method and the factorial moment method agree with the analytic values.

Table 5.1: Comparison of cumulants of net-proton multiplicity distribution, assuming a Poisson distribution for protons and anti-protons with Binomial efficiency

Cumulants for net-proton distribution	Skellam (analytically)	Efficiency corrected (data-driven method)	Efficiency corrected (Factorial moment method)
C_1	1	0.9996 ± 0.0005	1.001 ± 0.0006
C_2	19	18.990 ± 0.003	18.990 ± 0.004
C_3	1	1.03 ± 0.02	1.04 ± 0.03
C_4	19	19.3 ± 0.4	18.7 ± 0.3

2. **Poisson distribution for protons and anti-protons with multiplicity-dependent efficiency**

   We assumed that the event-by-event distribution of protons is given by a Poisson distribution with mean 10 and anti-protons with mean 9. The efficiency for protons is assumed to be $0.8 - 0.0003\ N_{proton}$, while for anti-protons, it is $0.7 - 0.0003\ N_{anti-proton}$ respectively. We compare the results in Table 5.2. We find that the results from the data-driven method agree well with the analytic values, while the corrected cumulants obtained from the factorial moment method starts to deviate from the analytic values for higher-order cumulants. Thus, we confirmed that seemingly small non-Binomial effects could have noticeable consequences on higher-order cumulants as pointed out by.

Table 5.2: Comparison of cumulants of net-proton multiplicity distribution, assuming a Poisson distribution for protons and anti-protons with multiplicity-dependent efficiency

Cumulants for net-proton distribution	Skellam (analytically)	Efficiency corrected (data-driven method)	Efficiency corrected (Factorial moment method)
C_1	1	1.000 ± 0.0004	0.998 ± 0.0006
C_2	19	19.000 ± 0.004	18.780 ± 0.004
C_3	1	1.02 ± 0.02	1.07 ± 0.03
C_4	19	19.1 ± 0.3	17.0 ± 0.3

3. **The AMPT model with multiplicity-dependent efficiency for $0-5\%$ central Au+Au collisions at $\sqrt{s_{NN}}$ = 200 GeV**

   We assumed that the event-by-event distribution of protons and anti-protons are given by the AMPT model [88]. The efficiency for protons is assumed to be 0.8 – 0.0003 $N_{charge} - N_{proton} - N_{anti-proton}$, while for anti-protons, it is 0.7 – 0.0003 $N_{charge} - N_{proton} - N_{anti-proton}$ respectively. The coefficient 0.0003 is the expected order of magnitude of the multiplicity dependence of efficiency in real data. We compare the results in Table 5.3. We find that the results from the data-driven method agree well with the cumulants of the true distribution. In the 2-D response matrix situation, both protons and anti-protons are corrected simultaneously, that is, the response matrix is a two-dimensional histogram containing the information for produced number of both protons and anti-protons for every measured number of protons and anti-protons. In the 1-D response matrix approach, protons and anti-protons are corrected separately, that is, the response matrix is two one-dimensional matrices; one for protons and the other for anti-protons. The corrected cumulants obtained from the factorial moment method, however, deviate from the true values considerably. This is because the factorial moment method assumes binomial efficiency correction. Centrality bin width correction is applied to the factorial moment method.

Table 5.3: Comparison of cumulants of net-proton multiplicity distribution using AMPT model with multiplicity-dependent efficiency for 0 – 5% central Au+Au collisions at $\sqrt{s_{NN}}$ = 200 GeV

Cumulants for net-proton distribution	True distribution	Efficiency corrected (2-D response matrix)	Efficiency corrected (1-D response matrix)	Efficiency corrected (Factorial moment method)
C_1	2.799 ± 0.002	2.799 ± 0.002	2.800 ± 0.002	2.550 ± 0.001
C_2	31.44 ± 0.01	31.43 ± 0.01	49.78 ± 0.02	12.63 ± 0.01
C_3	8.4 ± 0.2	8.4 ± 0.1	9.3 ± 0.2	2.58 ± 0.04
C_4	91 ± 1	91 ± 2	89 ± 3	12.5 ± 0.3

5.4 STAR Embedding Framework

STAR embedding involves introduction of Monte-Carlo tracks into the real data. These Monte-Carlo tracks with the real data are passed through the entire reconstruction framework. The relations between the input Monte-Carlo tracks and the reconstructed tracks provides an insight into the efficiency of particle identification. Till date, only the Time Projection Chamber (TPC) has been entirely implemented within this framework.

5.4.1 Inputs for the embedding procedure

Within the current set-up at STAR, a maximum of 5% of the total particles in the event can be embedded reliably. In order to account for this, protons and anti-protons are embedded separately. Around 500, 000 events are processed with the details given in Table 5.4. The phase space for embedding is kept larger than that for data analysis to avoid edge effects. The (anti-)proton distribution is assumed to be a uniform distribution between 1 and 30.

Table 5.4: Details of embedding request for Au+Au collision at $\sqrt{s_{NN}} = 200$ GeV data taken in year 2014.

Variable	Range
Centrality	0 – 20%
Triggers	450050, 450060
Production chain	P16id + NoPxlIT, NoIstIT, NoSstIT
Library	SL16d
Z- vertex distribution, V_z	(-6, 6) cm
Radial vertex distribution, V_r	(0, 2) cm
Azimuthal angle, ϕ	(0, 6.29) radians, flat
Rapidity, y	(-0.6, 0.6), flat
Transverse momentum, p_T	(0.3, 2.2) GeV/c, exponential with slope 350 MeV

5.4.2 Efficiency from embedding

Certain checks are performed in order to establish whether the efficiency of (anti-)proton identification using TPC follows the Binomial distribution. For this, protons and anti-protons from the embedding data for 0-5% central collisions within $0.4 < p_T < 2.0$ GeV/c and $|y| < 0.5$ is used. Protons and anti-protons are sampled according to Poisson distribution. The distribution of rapidity, transverse momentum and multiplicity of input Monte-Carlo and reconstructed protons and anti-protons is shown in Figure 5.3. The left column corresponds to protons and the right column is for anti-protons.

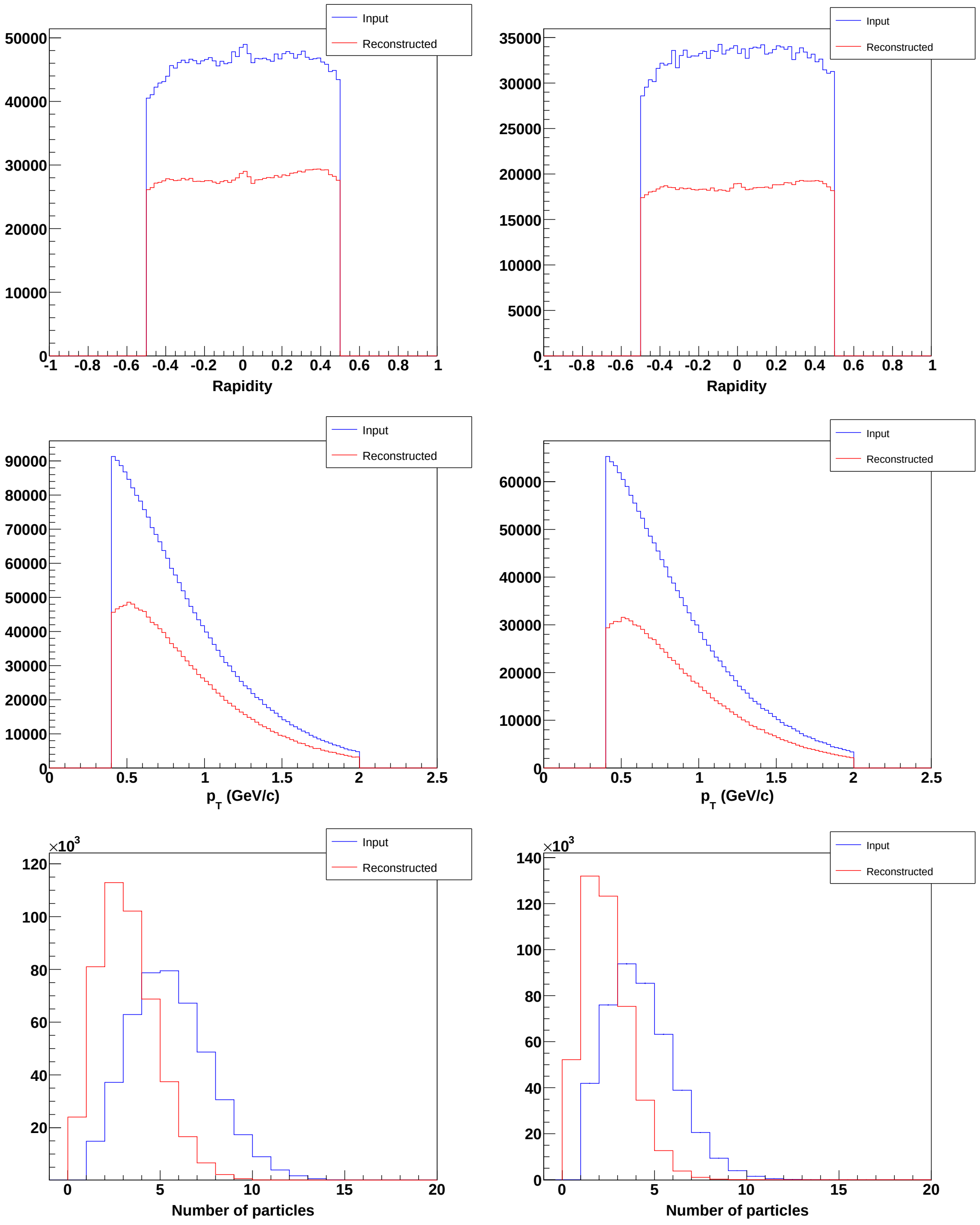

Figure 5.3: (Color online) Distribution of rapidity (top), transverse momentum (middle) and multiplicity (bottom) of input Monte-Carlo and reconstructed protons (left column) and anti-protons (right column) as obtained from the embedding data.

Efficiency is defined as the ratio of reconstructed particles to the input particles. The average efficiency for protons and anti-protons as a function of input number of particles is shown in Figure 5.4. The red square corresponds to the overall average efficiency.

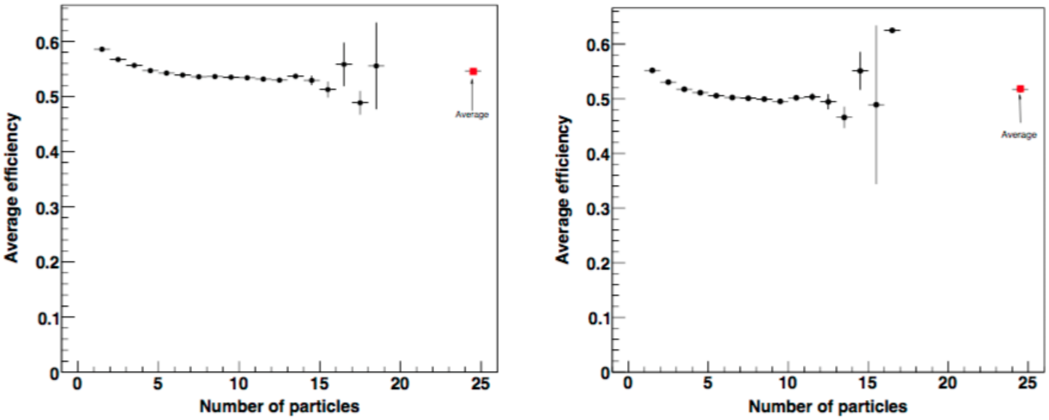

Figure 5.4: (Color online) Average efficiency of protons (left) and anti-protons (right) as obtained from the embedding data.

It is known that a linear combination of Binomial distributions with different means does not yield a Binomial distribution. A comparison with the Binomial function for efficiency with mean as the average for the particular number of input particles, as shown in Figure 5.5, establishes that the efficiency of (anti-)proton identification from the TPC deviates from Binomial.

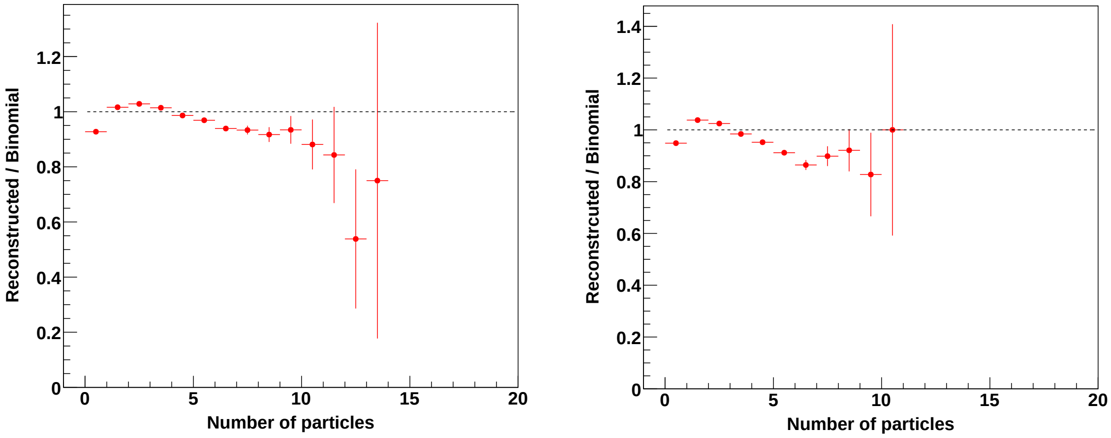

Figure 5.5: (Color online) The ratio of reconstruction efficiency to Binomial efficiency for protons (left) and anti-protons (right) as obtained from the embedding data.

The deviation from Binomial assumption is found up to a level of 10%, which may lead to significant impact on the values of the efficiency-corrected cumulants of multiplicity distributions.

5.5 Results and discussions

The data from Au+Au collisions at $\sqrt{s_{NN}} = 200$ GeV taken in the year 2014 is used to compare cumulants of net-proton-multiplicity distribution from the factorial moment method (that assumes Binomial efficiency) and the unfolding approach. The event and track selection criteria and the centrality determination algorithm have been discussed in great details in Chapter 4.

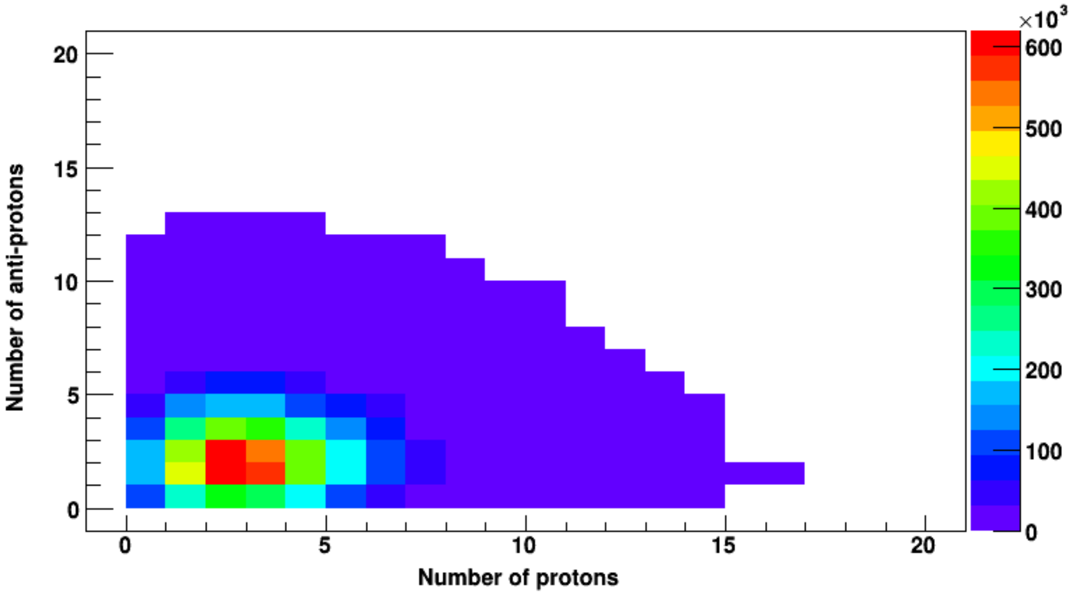

Figure 5.6: (Color online) Event-by-event correlation between the measured number of protons and anti-protons for 0-5% central collisions.

Figure 5.6 shows the correlation between event-by-event distribution of the measured protons and anti-protons. The phase space of the measurement is given by $0.4 < p_T < 0.8$ GeV/c and $|y| < 0.5$ for 0-5% central collisions. The response histograms are obtained by sampling a Poisson distribution for the protons and anti-protons using the embedding data, with mean as obtained from the factorial moment method for the given collision centrality.

A typical response histogram under the same phase space as data is given in Figure 5.7. The figure shows the distribution of input Monte-Carlo tracks in the embedding framework for a fixed number of reconstructed tracks. The solid lines correspond to protons, while the dashed lines are for anti-protons.

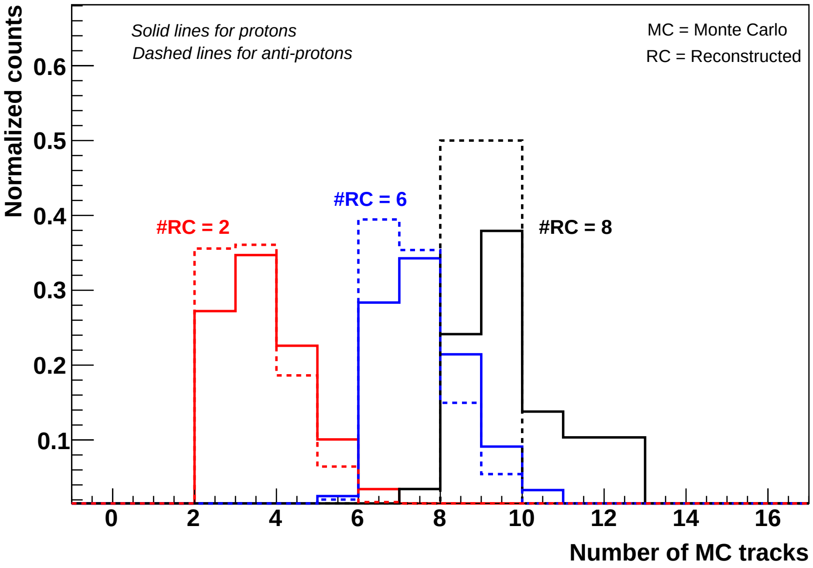

Figure 5.7: (Color online) Distribution of Monte-Carlo tracks for a fixed number of reconstructed tracks as obtained from embedding.

In order to estimate the cumulants and their respective errors, 100 copies are used. Figure 5.8 shows the first- to fourth-order efficiency-corrected cumulants of proton, anti-proton and net-proton multiplicity distributions for three centralities for Au+Au collisions at $\sqrt{s_{NN}} = 200$ GeV data taken in the year 2014. A comparison between the cumulants obtained from unfolding and the factorial moment method is also shown. We observe that the first-order cumulant is the same for both the methods. The difference between the higher-order cumulants increases with the order of the cumulant.

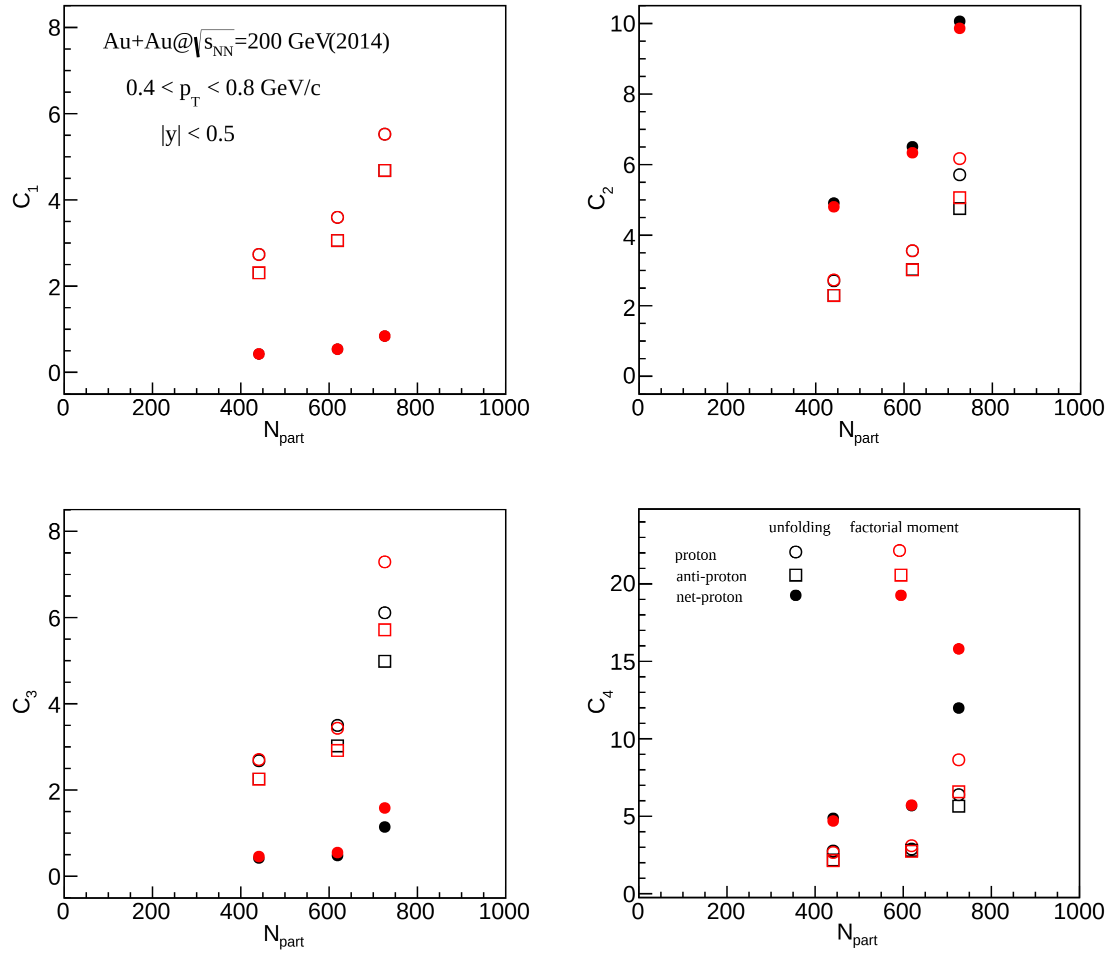

Figure 5.8: (Color online) Comparison between efficiency-corrected cumulants as obtained from unfolding and factorial moment methods.

5.6 Conclusion

Through Monte-Carlo simulations using the AMPT model, we demonstrated a data-driven efficiency correction method for the cumulants of multiplicity distributions to account for the possible experimental artifacts, like multiplicity-dependent efficiency.

The embedding framework at STAR is used in order to correct the particle multiplicity distributions as the observed multiplicity distribution is believed to be a convolution of produced multiplicity distribution and efficiency function.

The comparison of the measurements of the first four cumulants of proton, anti-proton and net-proton multiplicity distributions using the unfolding and the factorial moment methods indicated a noticeable difference in the final higher-order cumulant values. Non-binomial effects in the efficiency calculation should be taken into account in the correction for cumulant measurements.

CHAPTER 6

Summary and Outlook

The objective of this dissertation is to develop analysis methods to explore the phase diagram of strong interactions. From the theoretical perspective, the phase transition from the Quark-Gluon Plasma phase to the Hadron Gas phase is a first order phase transition for large baryon chemical potential that ends in a second order critical point. For small baryon chemical potential, the transition is predicted to be a cross-over.

Phase transitions are characterized by local density fluctuations. In the first part of the dissertation, we defined an observable, which is expected to be sensitive to local parton density fluctuations, based on the azimuthal distribution of produced particles. We established the sensitivity of the observable using a toy Monte-Carlo model. Within the coalescence mechanism of particle production, we expect the baryon distribution to be more sensitive to local parton density fluctuations. We studied the energy and centrality dependence of the cumulants of the event-by-event distribution of the aforementioned observable for protons with the STAR Beam Energy Scan data taken for Au+Au collisions for $\sqrt{s_{NN}} = 7.7 - 62.4$ GeV for different number of azimuthal divisions. We find certain non-monotonic trends in the higher-order cumulants with variation of collision energy for most central collisions. In the absence of a dynamical model that include phase transition, it is too early to associate these signatures to critical phenomenon or phase transitions. However, with more data coming in Beam Energy Scan II in 2019–2020, a detailed study of this new observable, would complement other studies of critical phenomenon in the QCD phase diagram.

The main focus of the second part of the dissertation shifts to the study of the cross-over transition for small baryon chemical potential. Lattice QCD calculations, which solves the QCD equation of state from first principles, is exact only for zero baryon chemical potential. In order to extend the calculations to finite baryon chemical potentials, the current best approach is Taylor expansion about zero baryon chemical potential. Constrained by statistics, up to fourth-order cumulants of net-proton (which is a proxy for net-baryon) multiplicity distribution have been well studied at STAR for Au+Au collision at $\sqrt{s_{NN}} = 200$ GeV. In order to further constrain the QCD equation of state, we measured the sixth-order cumulant of net-proton multiplicity distribution for the large statistics run taken in the year 2014. It is also predicted that the the sixth-order cumulant of net-baryon distribution remains negative beyond chiral transition temperature. We found that the sixth-order cumulant of net-proton multiplicity distribution remains negative for central collisions.

Appropriate corrections for detection efficiency is of utmost importance when performing any measurement. The previous measurements used efficiency correction for the cumulants of multiplicity distributions which are based on an analytical formula derived assuming a Binomial distribution for detector efficiency. Recent studies have shown that even a slight deviation from the Binomial assumption could have noticeable consequences on the measurement of the higher-order cumulants of multiplicity distributions. From detailed experimental analysis, we found that the detector efficiency depends on the collision centrality. Also, we know that a linear combination of two (or more) Binomial distributions is not a Binomial distributions. Unfortunately, the analytical formula cannot account for such slight efficiency variations. In order to account for these multiplicity-dependent variations, we developed an unfolding algorithm for precise measurements of the higher-order cumulants of multiplicity distributions. The algorithm is based on the inputs from the embedding framework at STAR. We used transport model calculations to establish the applicability of the proposed unfolding approach. We also measured the first few cumulants of net-proton multiplicity distribution for Au+Au collisions at $\sqrt{s_{NN}} = 200$ GeV for the data taken in the year 2014 and compared the results from tradition (Binomial) efficiency correction methods and the unfolding approach. With more precise measurements of the higher-order cumulants of multiplicity distributions of produced particles expected from Beam Energy Scan II in order to study phase transitions in the QCD phase diagram, such comparisons will be extremely insightful.

The methods developed as a part of this thesis will be useful tools for the understanding of experimental observations pertaining to the QCD phase diagram from the precision measurements expected to come out of Beam Energy Scan II at STAR, with larger statistics and advanced detector sub-systems.

APPENDIX A

List of bad runs

List of bad runs

Au+Au at $\sqrt{s_{NN}} = 7.7GeV$

11114085, 11114089, 11114095, 11115005, 11115042, 11115064, 11115080, 11116027, 11116028, 11116060, 11116068, 11116070, 11117044, 11117075, 11117088, 11117090, 11117098, 11118007, 11118008, 11118015, 11119024, 11119062, 11120040, 11120042, 11121044, 11121054, 11122037, 11122049, 11122050, 11122073, 11123028, 11123051, 11123053, 11123054, 11123055, 11123056, 11123057, 11123058, 11123059, 11123060, 11123076, 11123095, 11123102, 11124041, 11124046, 11124047, 11124048, 11124050, 11124062, 11128056, 11129028, 11133006, 11136005, 11136012, 11136013, 11142117, 11147006

Au+Au at $\sqrt{s_{NN}} = 11.5GeV$

11148001, 11148045, 11149015, 11149017, 11149018, 11149047, 11150025, 11150029, 11151050, 11151057, 11152016, 11152036, 11152078, 11153032, 11154026, 11156009, 11156036, 11156043, 11156044, 11156045, 11157050, 11158011, 11158012, 11158015, 11158016, 11158017, 11158019, 11158020, 11158021, 11158022, 11158024

Au+Au at $\sqrt{s_{NN}} = 14.5 GeV$

15046096, 15046106, 15046107, 15046108, 15046110, 15046111, 15047004, 15047015, 15047019, 15047021, 15047023, 15047027, 15047028, 15047029, 15047030, 15047039, 15047041, 15047044, 15047050, 15047056, 15047057, 15047061, 15047062, 15047064, 15047068, 15047069, 15047071, 15047074, 15047075, 15047082, 15047093, 15051131, 15051132, 15053052, 15053053, 15053054, 15053055

Au+Au at $\sqrt{s_{NN}} = 19.6 GeV$

12113091, 12114007, 12115014, 12115015, 12115016, 12115018, 12115019, 12115020, 12115022, 12115023, 12115026, 12115073, 12116012, 12116015, 12116016, 12120026, 12121017, 12121022, 12121034, 12122019

Au+Au at $\sqrt{s_{NN}} = 27 GeV$

12172050, 12172051, 12172055, 12173009, 12173030, 12173031, 12173032, 12173033, 12173034, 12174077, 12174085, 12174096, 12175062, 12175087, 12175113, 12175114, 12175115, 12176054, 12176067, 12176069, 12177092, 12177099, 12177101, 12177106, 12177107, 12177108, 12178003, 12178004, 12178005, 12178006, 12178051, 12178099, 12178123, 12179068

Au+Au at $\sqrt{s_{NN}} = 39 GeV$

11099124, 11100034, 11100045, 11101046, 11101104, 11102012, 11102098, 11103008, 11103009, 11103046, 11103058, 11103062, 11103065, 11105011, 11105018, 11105029, 11106026, 11106027, 11106028, 11106029, 11106030, 11106040, 11106041, 11107061

Au+Au at $\sqrt{s_{NN}} = 62.4 GeV$

11108101, 11109013, 11109088, 11109090, 11109092, 11109097, 11109098, 11109100, 11109101, 11109102, 11109103, 11109104, 11109105, 11110041, 11110073

Au+Au at $\sqrt{s_{NN}} = 200 GeV$

15167014, 15078075, 15078110, 15078111, 15079042, 15079046, 15079047, 15079048, 15079050, 15079052, 15080029, 15080053, 15080054, 15080055, 15080056, 15080059, 15081001, 15081003, 15081015, 15082016, 15082023, 15082030, 15084009, 15084030, 15084053, 15084061, 15086060, 15086076, 15088004, 15088005, 15088006, 15089033, 15097059, 15098042, 15099001, 15102021, 15102024, 15102059, 15103030, 15104016, 15104018, 15108017, 15108018, 15108019, 15108020, 15109039, 15109040, 15118063, 15121062, 15121063, 15121065, 15121066, 15121067, 15121068, 15122045, 15125003, 15125067, 15126021, 15129006, 15131052, 15131053, 15135013, 15141009, 15144004, 15145012, 15145021, 15146017, 15150031, 15151005, 15151041, 15151042, 15152051, 15153022, 15156008, 15157048, 15161010, 15161051, 15163061, 15164034, 15165033, 15166014, 15166015, 15166016, 15166017

REFERENCES

[1] "http://www.bnl.gov/rhic."

[2] G. Baym, "RHIC: From dreams to beams in two decades," *Nucl. Phys.*, vol. A698, 2002.

[3] S. L. Glashow, "Partial Symmetries of Weak Interactions," *Nucl. Phys.*, vol. 22, pp. 579–588, 1961.

[4] S. Weinberg, "A Model of Leptons," *Phys. Rev. Lett.*, vol. 19, pp. 1264–1266, 1967.

[5] A. Salam and J. C. Ward, "Electromagnetic and weak interactions," *Phys. Lett.*, vol. 13, pp. 168–171, 1964.

[6] P. W. Higgs, "Broken Symmetries and the Masses of Gauge Bosons," *Phys. Rev. Lett.*, vol. 13, pp. 508–509, 1964.

[7] P. W. Higgs, "Broken symmetries, massless particles and gauge fields," *Phys. Lett.*, vol. 12, pp. 132–133, 1964.

[8] F. Englert and R. Brout, "Broken Symmetry and the Mass of Gauge Vector Mesons," *Phys. Rev. Lett.*, vol. 13, pp. 321–323, 1964.

[9] G. Aad *et al.*, "Observation of a new particle in the search for the Standard Model Higgs boson with the ATLAS detector at the LHC," *Phys. Lett.*, vol. B716, pp. 1–29, 2012.

[10] S. Chatrchyan *et al.*, "Observation of a new boson at a mass of 125 GeV with the CMS experiment at the LHC," *Phys. Lett.*, vol. B716, pp. 30–61, 2012.

[11] S. Bethke, "Experimental tests of asymptotic freedom," *Prog. Part. Nucl. Phys.*, vol. 58, pp. 351–386, 2007.

[12] K. G. Wilson, "Confinement of Quarks," *Phys. Rev.*, vol. D10, pp. 2445–2459, 1974.

[13] A. Chodos, R. L. Jaffe, K. Johnson, C. B. Thorn, and V. F. Weisskopf, "A New Extended Model of Hadrons," *Phys. Rev.*, vol. D9, pp. 3471–3495, 1974.

[14] C. E. DeTar and J. F. Donoghue, "Bag Models of Hadrons," *Ann. Rev. Nucl. Part. Sci.*, vol. 33, pp. 235–264, 1983.

[15] D. J. Gross and F. Wilczek, "Asymptotically free gauge theories - i," *Phys. Rev.*, vol. D8, pp. 3633–3652, 1973.

[16] D. J. Gross and F. Wilczek, "Asymptotically free gauge theories - 2," *Phys. Rev.*, vol. D9, pp. 980–993, 1974.

[17] H. D. Politzer, "Reliable Perturbative Results for Strong Interactions?," *Phys. Rev. Lett.*, vol. 30, pp. 1346–1349, 1973.

[18] T. D. Lee and G. C. Wick, “Vacuum Stability and Vacuum Excitation in a Spin 0 Field Theory,” *Phys. Rev.*, vol. D9, pp. 2291–2316, 1974.

[19] F. Karsch and K. Redlich, “Has Tc been measured by heavy ion experiments?,” *Phys. Rev.*, vol. D84, p. 051504, 2011.

[20] F. Karsch, “Lattice results on QCD thermodynamics,” *Nucl. Phys.*, vol. A698, pp. 199–208, 2002.

[21] B. Mohanty, “Exploring the QCD landscape with high-energy nuclear collisions,” *New J. Phys.*, vol. 13, p. 065031, 2011.

[22] F. R. Brown, F. P. Butler, H. Chen, N. H. Christ, Z.-h. Dong, W. Schaffer, L. I. Unger, and A. Vaccarino, “On the existence of a phase transition for QCD with three light quarks,” *Phys. Rev. Lett.*, vol. 65, pp. 2491–2494, 1990.

[23] Y. Aoki, G. Endrodi, Z. Fodor, S. D. Katz, and K. K. Szabo, “The Order of the quantum chromodynamics transition predicted by the standard model of particle physics,” *Nature*, vol. 443, pp. 675–678, 2006.

[24] Y. Hatta and T. Ikeda, “Universality, the QCD critical / tricritical point and the quark number susceptibility,” *Phys. Rev.*, vol. D67, p. 014028, 2003.

[25] Z. Fodor, “Lattice QCD results at finite temperature and density,” *Nucl. Phys.*, vol. A715, pp. 319–328, 2003.

[26] A. Andronic, P. Braun-Munzinger, J. Stachel, and H. Stocker, “Production of light nuclei, hypernuclei and their antiparticles in relativistic nuclear collisions,” *Phys. Lett.*, vol. B697, pp. 203–207, 2011.

[27] J. Adams *et al.*, “Experimental and theoretical challenges in the search for the quark gluon plasma: The STAR Collaboration’s critical assessment of the evidence from RHIC collisions,” *Nucl. Phys.*, vol. A757, pp. 102–183, 2005.

[28] A. M. Poskanzer and S. A. Voloshin, “Methods for analyzing anisotropic flow in relativistic nuclear collisions,” *Phys. Rev.*, vol. C58, pp. 1671–1678, 1998.

[29] L. Adamczyk *et al.*, “Beam-Energy Dependence of the Directed Flow of Protons, Antiprotons, and Pions in Au+Au Collisions,” *Phys. Rev. Lett.*, vol. 112, no. 16, p. 162301, 2014.

[30] P. Shanmuganathan, “Beam-Energy and Centrality Dependence of Directed Flow of Identified Particles,” *Nucl. Phys.*, vol. A956, pp. 260–263, 2016.

[31] L. Adamczyk *et al.*, “Centrality dependence of identified particle elliptic flow in relativistic heavy ion collisions at $\sqrt{s_{NN}}$=7.7–62.4 GeV,” *Phys. Rev.*, vol. C93, no. 1, p. 014907, 2016.

[32] P. Huovinen, P. F. Kolb, U. W. Heinz, P. V. Ruuskanen, and S. A. Voloshin, “Radial and elliptic flow at RHIC: Further predictions,” *Phys. Lett.*, vol. B503, pp. 58–64, 2001.

[33] A. Wroblewski, “On the Strange Quark Suppression Factor in high-energy collisions,” *Acta Phys. Polon.*, vol. B16, pp. 379–392, 1985.

[34] T. Alber *et al.*, “Strange particle production in nuclear collisions at 200-GeV per nucleon,” *Z. Phys.*, vol. C64, pp. 195–207, 1994.

[35] P. G. Jones *et al.*, “Hadron yields and hadron spectra from the NA49 experiment,” *Nucl. Phys.*, vol. A610, pp. 188C–199C, 1996.

[36] J. Rafelski and B. Muller, “Strangeness Production in the Quark - Gluon Plasma,” *Phys. Rev. Lett.*, vol. 48, p. 1066, 1982. [Erratum: Phys. Rev. Lett.56,2334(1986)].

[37] B. I. Abelev *et al.*, “Measurements of phi meson production in relativistic heavy-ion collisions at RHIC,” *Phys. Rev.*, vol. C79, p. 064903, 2009.

[38] B. Muller, “Phenomenology of jet quenching in heavy ion collisions,” *Phys. Rev.*, vol. C67, p. 061901, 2003.

[39] A. Majumder and M. Van Leeuwen, “The Theory and Phenomenology of Perturbative QCD Based Jet Quenching,” *Prog. Part. Nucl. Phys.*, vol. 66, pp. 41–92, 2011.

[40] L. P. Csernai, G. Mocanu, and Z. Neda, “Fluctuations in Hadronizing QGP,” *Phys. Rev.*, vol. C85, p. 068201, 2012.

[41] A. Bazavov *et al.*, “The QCD Equation of State to $\mathcal{O}(\mu_B^6)$ from Lattice QCD,” *Phys. Rev.*, vol. D95, no. 5, p. 054504, 2017.

[42] M. A. Stephanov, “On the sign of kurtosis near the QCD critical point,” *Phys. Rev. Lett.*, vol. 107, p. 052301, 2011.

[43] M. A. Stephanov, “Non-Gaussian fluctuations near the QCD critical point,” *Phys. Rev. Lett.*, vol. 102, p. 032301, 2009.

[44] M. Asakawa, S. Ejiri, and M. Kitazawa, “Third moments of conserved charges as probes of QCD phase structure,” *Phys. Rev. Lett.*, vol. 103, p. 262301, 2009.

[45] J. Thäder, “Higher Moments of Net-Particle Multiplicity Distributions,” *Nucl. Phys.*, vol. A956, pp. 320–323, 2016.

[46] M. M. Aggarwal *et al.*, “Higher Moments of Net-proton Multiplicity Distributions at RHIC,” *Phys. Rev. Lett.*, vol. 105, p. 022302, 2010.

[47] L. Adamczyk *et al.*, “Beam energy dependence of moments of the net-charge multiplicity distributions in Au+Au collisions at RHIC,” *Phys. Rev. Lett.*, vol. 113, p. 092301, 2014.

[48] L. Adamczyk *et al.*, “Collision Energy Dependence of Moments of Net-Kaon Multiplicity Distributions at RHIC,” *Phys. Lett.*, vol. B785, pp. 551–560, 2018.

[49] A. Bzdak, R. Holzmann, and V. Koch, “Multiplicity dependent and non-binomial efficiency corrections for particle number cumulantsMultiplicity-dependent and nonbinomial efficiency corrections for particle number cumulants,” *Phys. Rev.*, vol. C94, no. 6, p. 064907, 2016.

[50] M. Harrison, S. G. Peggs, and T. Roser, “The RHIC accelerator,” *Ann. Rev. Nucl. Part. Sci.*, vol. 52, pp. 425–469, 2002.

[51] G. Bunce, N. Saito, J. Soffer, and W. Vogelsang, “Prospects for spin physics at RHIC,” *Ann. Rev. Nucl. Part. Sci.*, vol. 50, pp. 525–575, 2000.

[52] W. Vogelsang, “QCD spin physics: Status, and prospects for RHIC,” *Pramana*, vol. 63, p. 1251, 2004.

[53] L. C. Bland, “Spin physics at RHIC,” *AIP Conf. Proc.*, vol. 675, no. 1, pp. 98–111, 2003.

[54] “http://www.agsrhichome.bnl.gov/RHIC/Runs/index.html.”

[55] M. Harrison, T. Ludlam, and S. Ozaki, “RHIC project overview,” *Nucl. Instrum. Meth.*, vol. A499, pp. 235–244, 2003.

[56] M. Anerella *et al.*, “The RHIC magnet system,” *Nucl. Instrum. Meth.*, vol. A499, pp. 280–315, 2003.

[57] K. H. Ackermann *et al.*, “STAR detector overview,” *Nucl. Instrum. Meth.*, vol. A499, pp. 624–632, 2003.

[58] K. Adcox *et al.*, “PHENIX detector overview,” *Nucl. Instrum. Meth.*, vol. A499, pp. 469–479, 2003.

[59] B. B. Back *et al.*, “The PHOBOS detector at RHIC,” *Nucl. Instrum. Meth.*, vol. A499, pp. 603–623, 2003.

[60] M. Adamczyk *et al.*, “The BRAHMS experiment at RHIC,” *Nucl. Instrum. Meth.*, vol. A499, pp. 437–468, 2003.

[61] M. Anderson *et al.*, “The Star time projection chamber: A Unique tool for studying high multiplicity events at RHIC,” *Nucl. Instrum. Meth.*, vol. A499, pp. 659–678, 2003.

[62] “https://drupal.star.bnl.gov/STAR/starnotes/public/csn0121.”

[63] “https://drupal.star.bnl.gov/star/ starnotes/public/sn0600..”

[64] W. J. Llope *et al.*, “The TOFp / pVPD time-of-flight system for STAR,” *Nucl. Instrum. Meth.*, vol. A522, pp. 252–273, 2004.

[65] M. Beddo *et al.*, “The STAR barrel electromagnetic calorimeter,” *Nucl. Instrum. Meth.*, vol. A499, pp. 725–739, 2003.

[66] C. E. Allgower *et al.*, “The STAR endcap electromagnetic calorimeter,” *Nucl. Instrum. Meth.*, vol. A499, pp. 740–750, 2003.

[67] F. Bergsma *et al.*, “The STAR detector magnet subsystem,” *Nucl. Instrum. Meth.*, vol. A499, pp. 633–639, 2003.

[68] L. Ruan *et al.*, “Perspectives of a Midrapidity Dimuon Program at RHIC: A Novel and Compact Muon Telescope Detector,” *J. Phys.*, vol. G36, p. 095001, 2009.

[69] C. Adler *et al.*, “The STAR level-3 trigger system,” *Nucl. Instrum. Meth.*, vol. A499, pp. 778–791, 2003.

[70] J. Kiryluk, “Local polarimetry for proton beams with the STAR beam beam counters,” in *Spin physics. Polarized electron sources and polarimeters. Proceedings, 16th International Symposium, SPIN 2004, Trieste, Italy, October 10-16, 2004, and Workshop, PESP 2004, Mainz, Germany, October 7-9, 2004*, pp. 718–721, 2005.

[71] G. Contin *et al.*, “The STAR MAPS-based PiXeL detector,” *Nucl. Instrum. Meth.*, vol. A907, pp. 60–80, 2018.

[72] J. H. Thomas, “A TPC for measuring high multiplicity events at RHIC,” *Nucl. Instrum. Meth.*, vol. A478, pp. 166–169, 2002.

[73] H. Bichsel, “A method to improve tracking and particle identification in TPCs and silicon detectors,” *Nucl. Instrum. Meth.*, vol. A562, pp. 154–197, 2006.

[74] M. Shao, L. J. Ruan, H. F. Chen, J. Wu, C. Li, Z. Z. Xu, X. L. Wang, S. L. Huang, Z. M. Wang, and Z. P. Zhang, “Beam test results of two kinds of multi-gap resistive plate chambers,” *Nucl. Instrum. Meth.*, vol. A492, pp. 344–350, 2002.

[75] B. Bonner, H. Chen, G. Eppley, F. Geurts, J. Lamas Valverde, C. Li, W. J. Llope, T. Nussbaum, E. Platner, and J. Roberts, “A single Time-of-Flight tray based on multigap resistive plate chambers for the STAR experiment at RHIC,” *Nucl. Instrum. Meth.*, vol. A508, pp. 181–184, 2003.

[76] E. Cerron Zeballos, I. Crotty, D. Hatzifotiadou, J. Lamas Valverde, S. Neupane, M. C. S. Williams, and A. Zichichi, “A New type of resistive plate chamber: The Multigap RPC,” *Nucl. Instrum. Meth.*, vol. A374, pp. 132–136, 1996.

[77] R. J. Fries, B. Muller, C. Nonaka, and S. A. Bass, “Hadronization in heavy ion collisions: Recombination and fragmentation of partons,” *Phys. Rev. Lett.*, vol. 90, p. 202303, 2003.

[78] R. J. Fries, V. Greco, and P. Sorensen, “Coalescence Models For Hadron Formation From Quark Gluon Plasma,” *Ann. Rev. Nucl. Part. Sci.*, vol. 58, pp. 177–205, 2008.

[79] S. A. Bass, “Review of parton recombination models,” *J. Phys. Conf. Ser.*, vol. 50, pp. 279–288, 2006.

[80] F. Karsch and K. Redlich, “Probing freeze-out conditions in heavy ion collisions with moments of charge fluctuations,” *Phys. Lett.*, vol. B695, pp. 136–142, 2011.

[81] B. Friman, F. Karsch, K. Redlich, and V. Skokov, “Fluctuations as probe of the QCD phase transition and freeze-out in heavy ion collisions at LHC and RHIC,” *Eur. Phys. J.*, vol. C71, p. 1694, 2011.

[82] X. Luo and N. Xu, “Search for the QCD Critical Point with Fluctuations of Conserved Quantities in Relativistic Heavy-Ion Collisions at RHIC : An Overview,” *Nucl. Sci. Tech.*, vol. 28, no. 8, p. 112, 2017.

[83] X. Luo, J. Xu, B. Mohanty, and N. Xu, “Volume fluctuation and auto-correlation effects in the moment analysis of net-proton multiplicity distributions in heavy-ion collisions,” *J. Phys.*, vol. G40, p. 105104, 2013.

[84] B. Efron and R. J. Tibshirani, *An Introduction to the Bootstrap.* No. 57 in Monographs on Statistics and Applied Probability, Boca Raton, Florida, USA: Chapman & Hall/CRC, 1993.

[85] X. Luo, “Unified description of efficiency correction and error estimation for moments of conserved quantities in heavy-ion collisions,” *Phys. Rev.*, vol. C91, no. 3, p. 034907, 2015. [Erratum: Phys. Rev.C94,no.5,059901(2016)].

[86] A. Bzdak and V. Koch, “Local Efficiency Corrections to Higher Order Cumulants,” *Phys. Rev.*, vol. C91, no. 2, p. 027901, 2015.

[87] T. Nonaka, M. Kitazawa, and S. Esumi, “More efficient formulas for efficiency correction of cumulants and effect of using averaged efficiency,” *Phys. Rev.*, vol. C95, no. 6, p. 064912, 2017.

[88] Z.-W. Lin, C. M. Ko, B.-A. Li, B. Zhang, and S. Pal, “A Multi-phase transport model for relativistic heavy ion collisions,” *Phys. Rev.*, vol. C72, p. 064901, 2005.